The Dissertation Committee for Wen Liao Certifies that this is the approved version of the following dissertation:

Controlling Nucleation and Growth of Ultra-Thin Ruthenium Films in Chemical Vapor Deposition

Committee:

John G. Ekerdt, Supervisor

Brian A. Korgel

Gyeong S. Hwang

Lea Hildebrandt Ruiz

Paulo Ferreira

Controlling Nucleation and Growth of Ultra-Thin Ruthenium Films in Chemical Vapor Deposition

by

Wen Liao, B. S. Chem. E.

Dissertation

Presented to the Faculty of the Graduate School of

The University of Texas at Austin

in Partial Fulfillment

of the Requirements

for the Degree of

Doctor of Philosophy

The University of Texas at Austin

May 2016

Dedication

To my lovely family

Acknowledgements

Firstly, I would like to express my sincere gratitude to my advisor Prof. Ekerdt for the continuous support of my Ph.D study and related research, for his patience, motivation, and immense knowledge. His guidance helped me in all the time of research and writing of this thesis. I could not have imagined having a better advisor and mentor for my Ph.D study.

Besides my advisor, I would like to thank the rest of my thesis committee: Prof. Korgel, Prof. Hwang, Prof. Hildebrandt Ruiz, and Prof. Ferreira for their insightful comments and encouragement.

A special thanks goes to my labmates, Dr. Joe M. McCrate, Dr. Tyler Elko-Hansen, Dr. Martin "DJ" McDaniel, Dr. Thong Ngo, Dan Bost, Brad Leonhardt, Sonali Chopra, Zizhuo Zhang, Edward Lin, Shen Hu, Himmi Nallan and Bryce Edmondson for sharing their truthful and illuminating views on a number of issues related to the research. In particular, I am grateful to Dan Bost for his expertise on all equipment.

I would also like to acknowledge with much appreciation the staff, Jim Smitherman, Shallaco McDonald, Butch Cunningham, Randy Rife, Kevin J. Haynes, Dr. Steve Swinnea and Dr. Dwight Romanovic, who helped me to assemble the machine units and gave me permission to the research facilities.

Last but not least, I also want to thank to National Science Foundation for their financial support (Award CBET-1160195).

Controlling Nucleation and Growth of Ultra-Thin Ruthenium Films in Chemical Vapor Deposition

Wen Liao, Ph. D.

The University of Texas at Austin, 2016

Supervisor: John G. Ekerdt

As feature sizes in microelectronic devices decrease, ultra-thin (< 3 nm) and smooth diffusion barriers are required to prevent copper from diffusing into the surrounding dielectric layers and to limit electron scattering at the copper-liner surface. Chemical vapor deposition (CVD) is one route to these barriers.

The inhibitor gas adsorbs on metal nanoparticles, forces additional nucleation and enhances nucleation density. Island growth combined with a sparse nucleation density leads to film roughness and the deposition of more metal mass than is needed to form a film of sufficient thickness to function as a copper diffusion barrier when compared to a uniformly-thick metal film.

In the first study, a higher nucleation density and smoother Ru film is achieved in CVD with CO addition during growth. CO competes with $Ru_3(CO)_{12}$ for free hydroxyl adsorption. The CO addition to $Ru_3(CO)_{12}$ deposition at proper timing and effective partial pressure reduces the film growth rate, surface roughness and nanocrystalline grain size by chemical vapor deposition.

The second study reports the use of ammonia to inhibit the growth of previously-nucleated ruthenium islands and force the nucleation of additional islands such that thinner films form as the islands coalesce with continued growth using $Ru_3(CO)_{12}$. The ammonia addition reduces the film nanocrystallinity and the films appear X-ray amorphous with the highest ammonia partial pressure during film deposition.

In the third study, films grown from $Ru(^t$Bu-Me-amd$)_2(CO)_2$ form a 2D wetting layer before 3D particle growth is observed. CO and ammonia addition to the gas phase during film growth from $Ru(^t$Bu-Me-amd$)_2(CO)_2$ leads to smoother films by inducing surface reconstructions during the film growth; these gases also lead to films with lower resistivity and lower crystalline character.

Overall, this research is to understand how blocking adsorbed moieties effect the nucleation of metals on a silica substrate, and to discover the principles leading to ultra-thin and smooth metallic films in CVD.

Table of Contents

List of Tables

List of Figures

Chapter 1: Introduction

1.1 Overview

In recent decades, the advancements in integrated circuits (IC) to increase speed and reduce power have come about through reduction in device dimensions. A smooth ultra-thin diffusion barrier/liner is required to prevent copper from diffusing into the interlayer dielectric and electromigration within the vias and wire lines in IC devices (Fig. 1.1).[1] Refractory metals, such as ruthenium, tungsten, and tantalum, and some metal nitrides are promising materials in future designs due to their high conductivity, superior thermodynamic and chemical stability, plus the low solubility with Cu.[2–4] Ruthenium is a potential candidate material for the diffusion barrier, particularly as it is highly conductive (ρ_{Ru}= 7.1 μΩ-cm), the surface oxide is conductive (ρ_{RuO2}= 40 μΩ-cm) and can be reduced under typical electroplating conditions, and Ru is not soluble with copper up to 900°C.[2–6] To minimize Cu diffusion through grain boundaries and improve Cu electroplating behavior on films, small nanocrystalline grain size and a smooth film surface are desired in the semiconductor industry (Fig. 1.2).[1] The barrier films need to be ultra-thin to maximize via cross-section for the copper conductor.

Chemical vapor deposition (CVD) is a possible technology to realize highly conformal thin films compared to physical sputtering and low temperature growth operations.[7] The comparison between the films grown by physical vapor deposition (PVD) and CVD on conformity and nanocrystallinity are illustrated in Figure 1.3 and Figure 1.4 respectively.

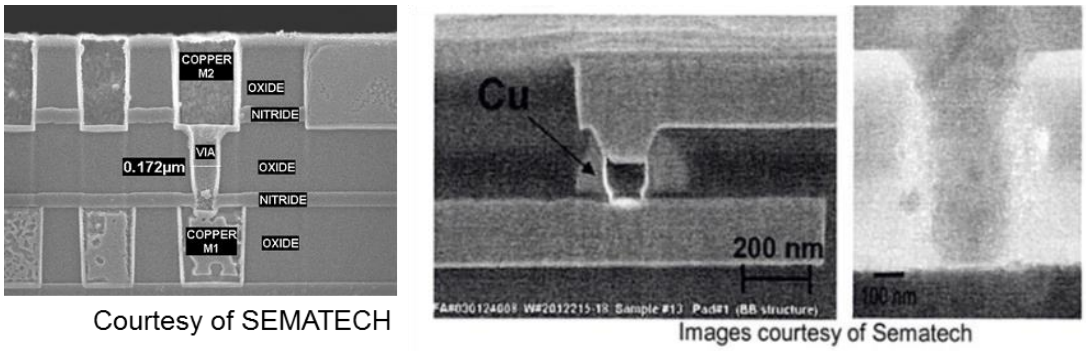

Figure 1.1: Example of copper diffusion in integrated circuit (Sematch).

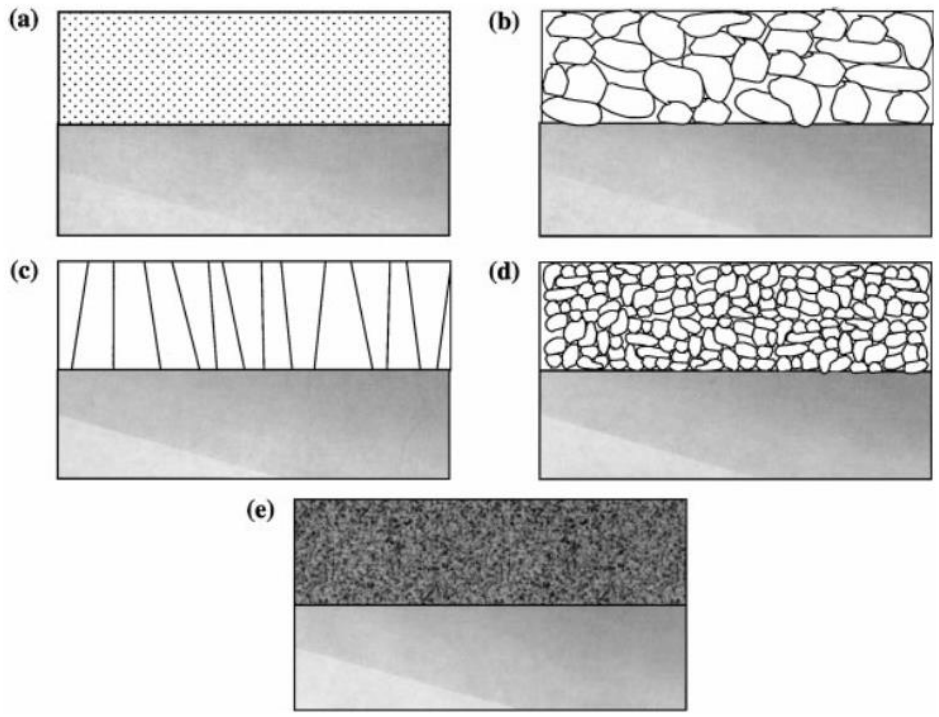

Figure 1.2: Liner microstructure can be categorized as (a) single crystal, (b) polycrystalline, (c) polycrystalline columnar, (d) nano-crystalline, and (e) amorphous.[1]

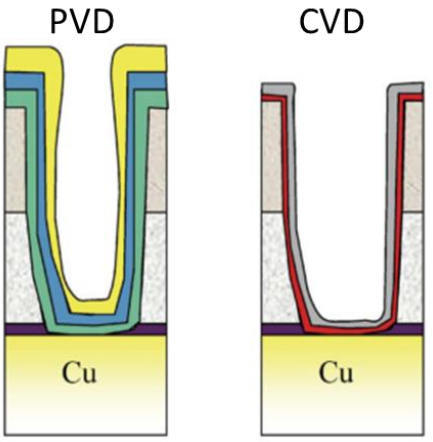

Figure 1.3: The comparison of conformity between physical vapor deposition and chemical vapor deposition.[4]

(a) (b)

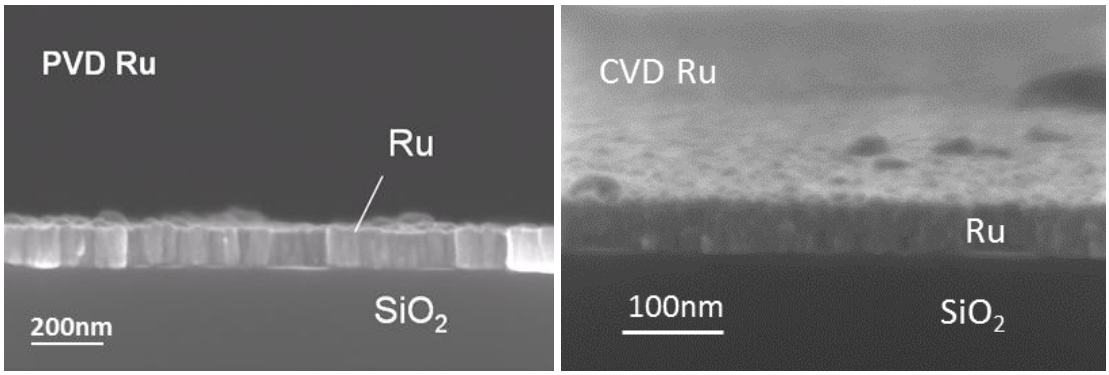

Figure 1.4: The comparison of conformity between (a) physical vapor deposition (J.H. Shin, unpublished) and (b) chemical vapor deposition.

Nucleation is a complicated process involving adatom adsorption, precursor decomposition, atoms binding to nucleate a critical cluster, surface diffusion, edge detachment and top re-evaporation (Fig. 1.5).[8,9] In general, once nucleation has occurred, additional adatoms incorporate into a nucleated particle faster than they nucleate new particles, i.e. growth is favored over new nuclei formation.[8–10] Film growth is generally categorized using three growth modes, Frank-van der Merwe (two-dimensional (2D) layer by layer growth), Volmer-Weber (VW, three dimensional (3D) growth), and Stranski–Krastanov (SK, the intermediate mode), depending on relative binding energies of adatoms on the islands and on the substrate (Fig. 1.6).[8–11] In the Volmer-Weber nucleations, the islands grow in 3D and coalesce to a continuous film eventually, while the Stranski–Krastanov mode means a layer plus island growth. Studies by kinetic Monte-Carlo simulation indicate that metal nucleation on oxides follows the Volmer-Weber growth mode.[8,9,11] However, the experimental data indicate that the metals nucleate on oxides with a growth mode between Volmer-Weber and Stranski–Krastanov growth, especially at low temperature.[11,12] In this case, the wetting layer may not completely cover the substrate before the 3D structures begin to form.

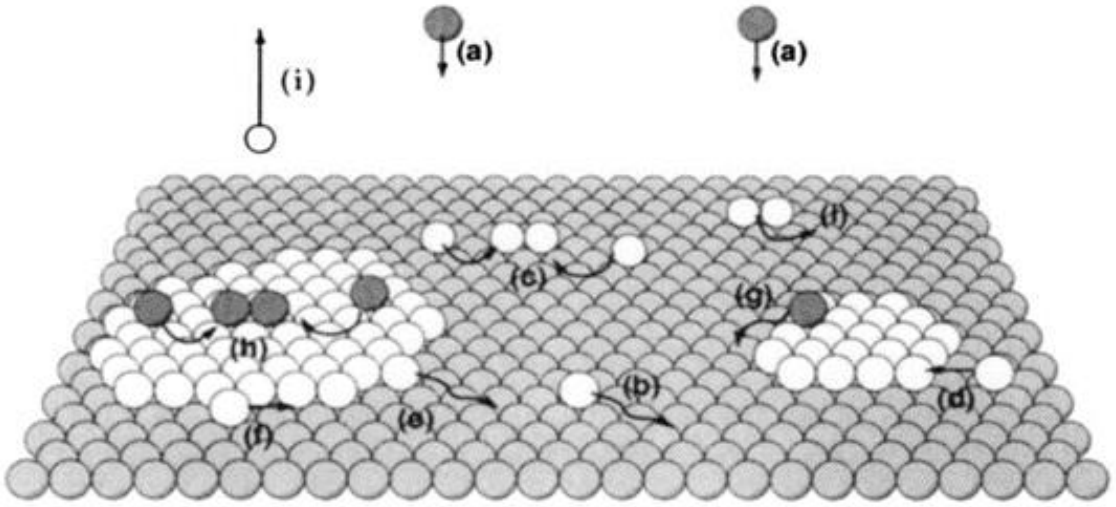

Figure 1.5: Typical atomistic processes during film growth.[9]

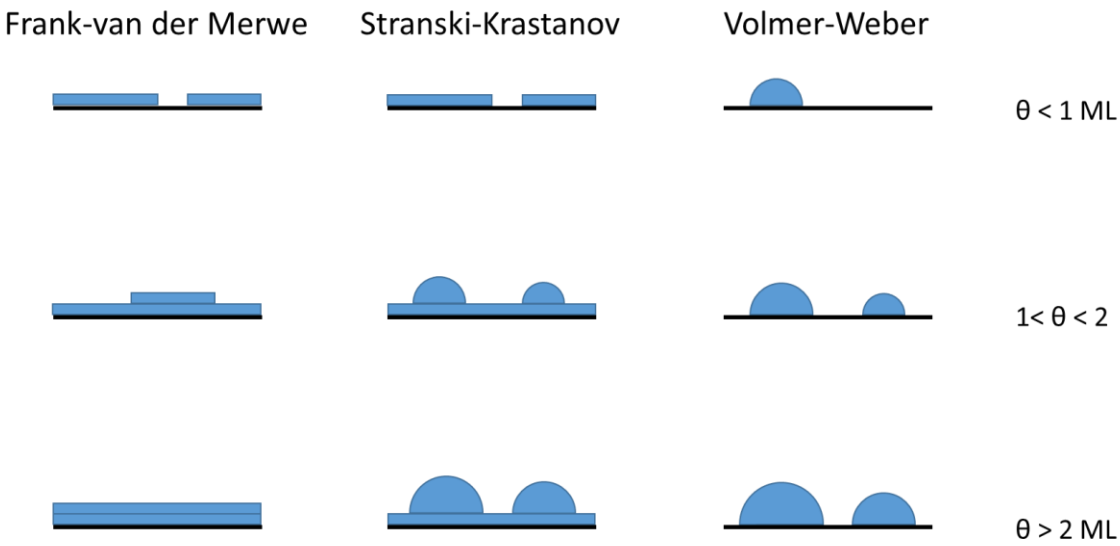

Figure 1.6: Three typical nucleation mode in theory, θ is the surface coverage.

Nanoparticle growth typically leads to the formation of three-dimensional islands that coalesce into a continuous film for a variety of reasons, including the unfavorable wetting associated with the high surface energy of the metal and the sparse nature of the nuclei from which the three dimensional islands grow.[10,13] Three-dimensional island growth combined with sparse nucleation leads to surface roughness and the deposition of more metal mass than is needed to form a film of sufficient thickness to function as a copper diffusion barrier when compared to a uniformly-thick metal film.[14] Growth chemistries that feature small and dense metal nuclei result in a thinner and smoother metal film than observed when big and sparse island merge with continued deposition (Fig. 1.7).[15] This research will explore chemical approaches to increasing island nucleation by enhancing new island formation and suppressing growth on existing islands (Fig. 1.8).

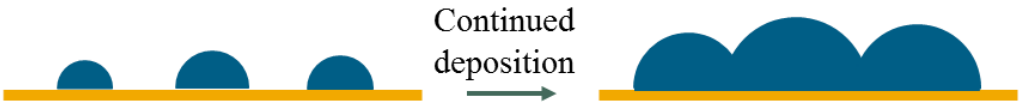

Big and sparse islands ⇒ surface roughness and the deposition of more metal mass than is needed to form a film of sufficient thickness to function as a copper diffusion barrier

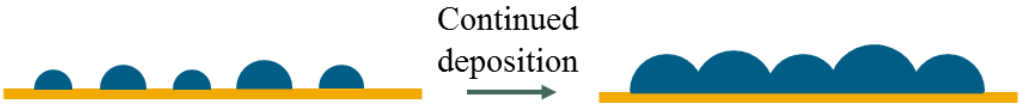

Small and dense metal nuclei ⇒ a uniformly-thick metal film, thinner and smoother

Figure 1.7: Illustration of film roughness grown from different nucleation.

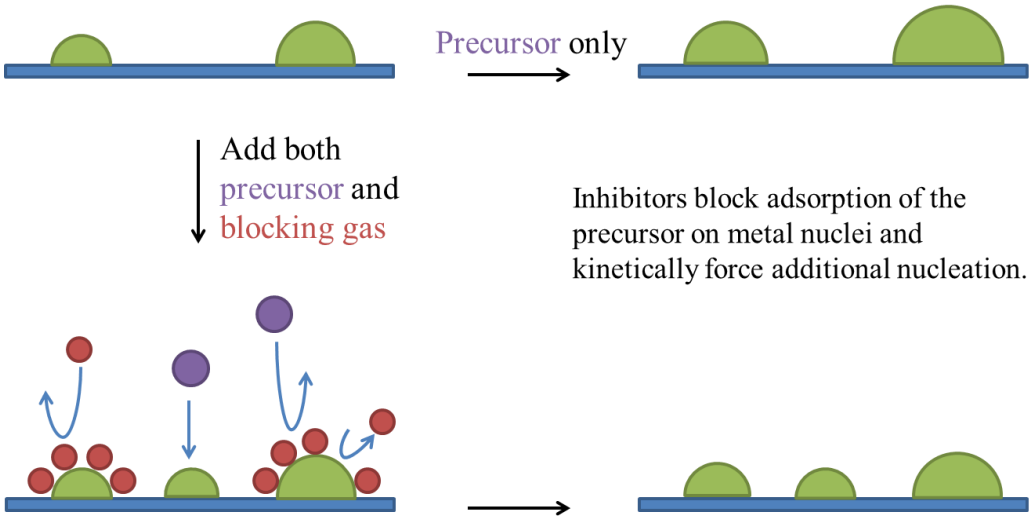

Figure 1.8: Illustration of inhibitor growth.

1.2 BACKGROUND

Chemical vapor deposition (CVD) is a broadly-used technology with advantages of high conformal coverage compared to physical sputtering and low temperature growth operations.[7] Chemical approaches are reported that increase island nucleation density by suppressing growth on existing islands using inhibitors that can block adsorption of the metal precursor or a co-reactant on exposed metal surfaces and thereby lead to growth of ultra-thin metal films.[16,17]

Iodine sources, such as CH_3I[15,18] and C_2H_5I,[18,19] in concert with $Ru(EtCp)_2$ are shown to enhance the nucleation density dramatically so as to improve film smoothness. Iodine worked with a Ru precursor that also needed co-reacting O_2 and may have functioned by surface segregating to the Ru surface and inhibiting oxygen adsorption on nucleated islands, which forced additional nuclei to form.[15] This study explores the use of inhibitors that can block adsorption of the metal precursor or a co-reactant, and function when O_2 is not the co-reactant.

Carbon monoxide (CO) has the potential to occupy the surface of Ru islands and thereby encourage additional nucleation on the oxide substrate surface. Carbon monoxide was selected as a Ru surface inhibitor because it adsorbs reversibly to Ru surfaces in the temperature range of precursor decomposition and Ru film growth (423 - 673 K).[3,20–22] As one of the potential Fischer–Tropsch synthesis catalysts,[23] the adsorption[20] and dissociation[24] of CO on various Ru crystal surfaces, including Ru(001),[21,22,25] Ru(109),[26] Ru(11$\bar{2}$0),[27] Ru(11$\bar{2}$1),[28] have been reported. Carbon monoxide can also adsorb at hydroxyl Si sites on SiO_2.[29–31]

Unlike CO, ammonia is expected to be inert toward the SiO_2 surface. Ammonia synthesis and decomposition are usually catalyzed by transition metals.[32] The NH_3 is expected to adsorb and form NH_x (x=2-0) depending on the metal, temperature and partial pressure of NH_3, N_2 and H_2. Ru crystals catalyze ammonia synthesis at temperatures between 600 and 900 K, and ammonia adsorbs on and desorbs from Ru surfaces during this process.[33,34] At low temperatures (500-600 K)[35], the steady state coverage of molecular ammonia and atomic hydrogen is expected to be exceedingly low on Ru and the coverage of adsorbed atomic nitrogen, N_{ads}, is expected to be near a monolayer as the recombinative desorption rate of adsorbed nitrogen as N_2 is slow.[39] In addition, some nitrogen dissolves in Ru for films sputtered in a N_2 ambient and this leads to X-ray amorphous Ru-N films that are stable below 548 K.[36] This study investigates the extent to which the dissociative adsorption and subsequent desorption of NH_3, H_2 and N_2 can be used to manipulate the coverage of NH_x (x=2-0) and alter nucleation and film growth.

When film growth follows a Stranski-Krastanov growth mode, smoother films may not be realized by increasing ad-atom formation on the oxide substrate. In addition to increasing nucleation density, gas chemisorption can induce metal surface reconstruction.[37–40] Hydrogen, nitrogen and CO are reported to modify platinum particle shape significantly through the variation of the surface free energy on different crystal facets.[41–44] The mechanisms of the atom/molecular induced reconstruction include the redistribution of surface electronic density,[40] the reduced activation energy of surface atom mobility,[38,39] and the higher adsorption heat on reconstructed surface[38,40] by the solid-gas interactions. A more open, rough surface with fewer neighboring atoms is more flexible

than a rigid bulk structure surface.[38,39] The formation and break-up of the substrate-adsorbate bond can drive the surface atom rearrangement to optimize surface chemical bonding.[39] This surface relaxation smooths out the film roughness gradually.[39] The previous studies of CO on Rh and oxygen on copper demonstrate the surface reconstruction by chemisorption.[45,46]

Representative Ru precursors used in the CVD process include $Ru(acac)_3$ (acac, acetylacetinate),[3,47] $Ru(CO)_4(hfb)$ (hfb, hexafluorlo-2-butyne),[48] $Ru(EtCp)_2$ (EtCp, ethylcycloentadienyl),[49] and $Ru_3(CO)_{12}$.[3,50] Triruthenium dodecacarbonyl, $Ru_3(CO)_{12}$, is capable of decomposing to nanocrystalline Ru (001) completely with negligible carbon content and excellent film adhesion at temperatures as low as 423K in the absence of any co-reacting gas.[1,50,51] Bis(*N,N'*-di-*tert*-butylacetamidinato) ruthenium(II) dicarbonyl, $Ru(^tBu\text{-}Me\text{-}amd)_2(CO)_2$ is an amidinate-ligand based chemical vapor deposition precursor with high thermal stability and sufficient volatility at 403 K to allow a vapor-phase growth for Ru.[52,53]

A general understanding of the adsorbate gas effect on nucleation and ultra-thin film growth using CVD is explored in this project. Plus, the advantages and limitations of each species of blocking adsorbate are explored. The nucleation density could be maximized with proper adsorbate gas addition for the optimal film dimensions and microstructure utilizing the discovered growth mechanism.

1.3 CHAPTER OVERVIEW

In chapter 3,[17] CO competes with $Ru_3(CO)_{12}$ for free hydroxyl adsorption. When CO and the Ru precursor are added to the CVD reaction chamber simultaneously at the beginning, the overpressure of CO reduces Ru nanoparticle density by limiting the Ru adatom formation at hydroxyl sites. CO also adsorbs on Ru nanoparticles, slowing their growth and facilitating additional, lower probability reactions between the $Ru_3(CO)_{12}$ precursor and the SiO_2 substrate; this new path to Ru adatoms leads to additional Ru island formation competitively with addition of Ru to existing nanoparticles, enhancing nucleation density. A higher nucleation density and smoother Ru film is achieved in CVD with CO addition during growth. The CO addition to $Ru_3(CO)_{12}$ deposition at proper timing and effective partial pressure reduces the film growth rate, surface roughness and nanocrystalline grain size by chemical vapor deposition.

In Chapter 4,[54] at low ammonia partial pressure, the blocking gas results in uniform smaller nanoparticles with a higher nucleation density that leads to smoother Ru films compared to Ru films deposited without ammonia. At the highest ammonia partial pressure, the ammonia keeps forcing additional nucleation and may lead to disparate sizes, but at a higher density, before the Ru particles coalesce to a continuous film. The large and small co-existing particles produce a rougher film compared to the film deposited with low ammonia partial pressure. Nitrogen residue on the film surface can be eliminated by post-growth annealing at 448 K, and there is no carbon or nitrogen contamination inside the Ru films. The smoothest thin film is achieved by high ammonia partial pressure during a 10-min nucleation step followed by a low ammonia pressure (5.25 mTorr) during the rest of

film growth. The ammonia addition reduces the film nanocrystallinity and the films appear X-ray amorphous with highest ammonia partial pressure (27.8 mTorr) during film deposition.

In Chapter 5, with free hydroxyl groups as activation sites, the $Ru_3(CO)_{12}$ forms adatoms that nucleate and grow in a VW 3D mode on silica. This free hydroxyl density on SiO_2 is manipulated by thermal pretreatment to enhance the initial nucleation density of the first sub-monolayer by surface chemistry. Stranski-Krastanov or 2DI growth is found with Ru(AMD) and 0.3-nm wetting layer forms quickly on SiO_2 followed by slower growth of Ru on Ru. 3D structures form on the 2D wetting layer. The addition of CO and NH_3 during CVD with Ru(AMD) can be used to control film texture and roughness by surface through adsorbate-induced reconstruction. CO and NH_3 addition sufficiently reduces the film roughness, nanocrystallite grain size and sheet resistivity for films grown with Ru(AMD).

1.4 REFERENCE

1. Kaloyeros, A. E. and Eisenbraun, E. *Annu. Rev. Mater. Sci.* **30,** 363–385 (2000).
2. Goswami, I. and Laxman, R. *Semicond. Int.* **27,** 49–54 (2004).
3. Green, M. L., Gross, M. E., Papa, L. E., Schnoes, K. J. and Brasen, D. *J. Electrochem. Soc.* **132,** 2677–2685 (1984).
4. Kim, H. *Surf. Coatings Technol.* **200,** 3104–3111 (2006).
5. Murakami, Y., Li, J., Hirose, D., Kohara, S. and Shimoda, T. *J. Mater. Chem. C* **3,** 4490–4499 (2015).
6. Chan, R., Arunagiri, T. N., Zhang, Y., Chyan, O., Wallace, R. M., Kim, M. J. and Hurd, T. Q. *Electrochem. Solid-State Lett.* **7,** G154–G157 (2004).

7. Crowell, J. E. *J. Vac. Sci. Technol. A* **21,** S88–S94 (2003).

8. Venables, J. A., Spiller, G. D. T. and Hanbucken, M. *Reports Prog. Phys.* **47,** 399–459 (1984).

9. Ratsch, C. and Venables, J. A. *J. Vac. Sci. Technol. A* **21,** S96–S109 (2003).

10. Brune, H. *Surf. Sci. Rep.* **31,** 121–229 (1998).

11. Campbell, C. T. *Surf. Sci. Rep.* **27,** 1–111 (1997).

12. Peden, C. H. F. *J. Vac. Sci. Technol. A* **9,** 1518 (1991).

13. Witten, T. A. and Sander, L. M. *Phys. Rev. Lett.* **47,** 1400–1403 (1981).

14. Park, S., Kim, H., Kim, K. and Min, S. *Electrochem. Solid-State Lett.* **1,** 262–264 (1998).

15. Thom, K. M. and Ekerdt, J. G. *Thin Solid Films* **518,** 36–42 (2009).

16. Babar, S., Kumar, N., Zhang, P., Abelson, J. R., Dunbar, A. C., Daly, S. R. and Girolami, G. S. *Chem. Mater.* **25,** 662–667 (2013).

17. Liao, W. and Ekerdt, J. G. *Chem. Mater.* **25,** 1793–1799 (2013).

18. Kim, J. J., Jung, D. H., Kim, M. S., Kim, S. H. and Yoon, D. Y. *Thin Solid Films* **409,** 28–32 (2002).

19. Kim, J. J., Kim, M. S. and Yoon, D. Y. *Chem. Vap. Depos.* **9,** 105–109 (2003).

20. Davydov, A. A. and Bell, A. T. *J. Catal.* **49,** 332–344 (1977).

21. Pfnür, H. and Menzel, D. *J. Chem. Phys.* **79,** 2400–2410 (1983).

22. Thomas, G. E. and Weinberg, W. H. *J. Chem. Phys.* **70,** 1437–1439 (1979).

23. Schulz, H. *Appl. Catal. A Gen.* **186,** 3–12 (1999).

24. Strebel, C., Murphy, S., Nielsen, R. M., Nielsen, J. H. and Chorkendorff, I. *Phys. Chem. Chem. Phys.* **14,** 8005–12 (2012).

25. Pfnür, H., Feulner, P., Engelhardt, H. A. and Menzel, D. *Chem. Phys. Lett.* **59,** 481–486 (1978).

26. Zubkov, T., Morgan, G. A., Yates, J. T., Kühlert, O., Lisowski, M., Schillinger, R., Fick, D. and Jänsch, H. J. *Surf. Sci.* **526,** 57–71 (2003).

27. Wang, J., Wang, Y. and Jacobi, K. *Surf. Sci.* **488,** 83–89 (2001).

28. Fan, C. Y., Bonzel, H. P. and Jacobi, K. *J. Chem. Phys.* **118,** 9773 (2003).

29. Beebe, T. P., Gelin, P. and Yates Jr., J. T. *Surf. Sci.* **148,** 526–550 (1984).

30. Ghlotti, G., Garrone, E., Morterra, C. and Boccuzzi, F. *J. Phys. Chem.* **83,** 2863–2869 (1979).

31. Ugliengo, P., Saunders, V. R. and Garrone, E. *J. Mater. Chem.* **93,** 5210–5215 (1989).

32. Boisen, A., Dahl, S., Norskov, J. K. and Christensen, C. H. *J. Catal.* **230,** 309–312 (2005).

33. Sanyan, S., Kantcheva, M., Suzer, S. and Uner, D. O. *J. Mol. Struct.* **480-481,** 241–245 (1999).

34. Dahl, S., Taylor, P. A., Törnqvist, E. and Chorkendorff, I. *J. Catal.* **178,** 679–686 (1998).

35. Tsai, W. and Weinberg, W. H. *J. Phys. Chem.* **91,** 5302–5307 (1987).

36. Damayanti, M., Sritharan, T., Mhaisalkar, S. G. and Gan, Z. H. *Appl. Phys. Lett.* **88,** 044101 (2006).

37. Zhdanov, V. P. and Zamaraev, K. I. *Sov. Phys. Usp.* **29,** 755–776 (1986).

38. Somorjai, G. A. *Surf. Sci.* **335,** 10–22 (1995).

39. Somorjai, G. *Annu. Rev. Phys. Chem.* **45,** 721–751 (1994).

40. Titmuss, S., Wander, A. and King, D. A. *Chem. Rev.* **96,** 1291–1306 (1996).

41. Lee, W. H. *et al.* The equilibrium shape and surface energy anisotropy of clean platinum. *J. Catal.* **126,** 658–670 (1990).

42. Shi, A. & Masel, R. The Effects of Gas Adsorption on Particle Platinum Catalysts Shapes in Supported. *J. Cat.* **120,** 421–431 (1989).

43. Lee, W. H., Petrova, V., VanLoon, K. R., Woodhouse, J. B., Loxton, C. M., Finnegan, N. L. and Masel, R. I. *Catal. Denctiuation* 597–603 (1991).

44. Shi, A.-C., Fung, K. K., Welch, J. F., Wortis, M. and Masel, R. I. *Mater. Res. Sociely* **111,** 59–64 (1988).

45. Parkin, S. R., Zeng, H. C., Zhou, M. Y. and Mitchell, K. A. R. *Phys. Rev. B* **41,** 5432–5435 (1990).

46. Kruse, N. and Gaussmann, A. *Surf. Sci.* **266,** 51–55 (1992).

47. Vigui, J. C. and Spitz, J. *J. Electrochem. Soc.* **122,** 585–588 (1975).

48. Senzaki, Y., Gladfelter, W. L. and McCormick, F. B. *Chem. Mater.* **5,** 1715–1721 (1993).

49. Matsui, Y., Hiratani, M., Nabatame, T., Shimamoto, Y. and Kimura, S. *Electrochem. Solid-State Lett.* **4,** C9–C12 (2001).

50. Wang, Q., Ekerdt, J. G., Gay, D., Sun, Y.-M. and White, J. M. *Appl. Phys. Lett.* **84,** 1380–1382 (2004).

51. Boyd, E. P., Ketchum, D. R., Deng, H. and Shore, S. G. *Chem. Mater.* **9,** 1154–1158 (1997).

52. Li, H., Farmer, D. B., Gordon, R. G., Lin, Y. and Vlassak, J. *J. Electrochem. Soc.* **154,** D642 (2007).

53. Gordon, R. G., Li, H., Aaltonen, T., Lim, B. S. and Li, Z. *Open Inorg. Chem. J.* **2,** 11–17 (2008).

54. Liao, W. and Ekerdt, J. G. *J. Vac. Sci. Technol. A* **34,** 031508 (2016)

Chapter 2: Experiment

2.1 APPARATUS

Figure 2.1 describes the surface analysis facility and growth reactors utilized in this research. This vacuum system is composed of a chemical vapor deposition (CVD) chamber, an *in situ* X-ray photoelectron spectrometer (XPS) equipped with ion sputtering, a physical vapor deposition (PVD) chamber, a high temperature furnace, a load-lock and a high vacuum transfer line connecting them. In PVD chamber, different high purity metal or metal oxide targets are sputtered by Ar plasma to produce thin films. Three targets can be installed in the PVD chamber side by side and grow films independently. The furnace is capable of annealing samples at temperature up to 1200 K in vacuum. The low pressure CVD (LPCVD) experiment is performed in the cold-wall CVD chamber operating from 10^{-3} to 10^{-5} Torr. Two separate saturators of precursors are loaded to the manifold at the same time and multiple gas species are investigated to improve the thin film characteristics. The *in situ* X-ray photoelectron spectrometer [Physical Electronics 3057; Mg Kα], connected to the CVD vessel with the ultra-high vacuum transfer line, is used to quantitatively detect element intensities on the film surfaces and inside the films after Ar^+ ion sputtering.

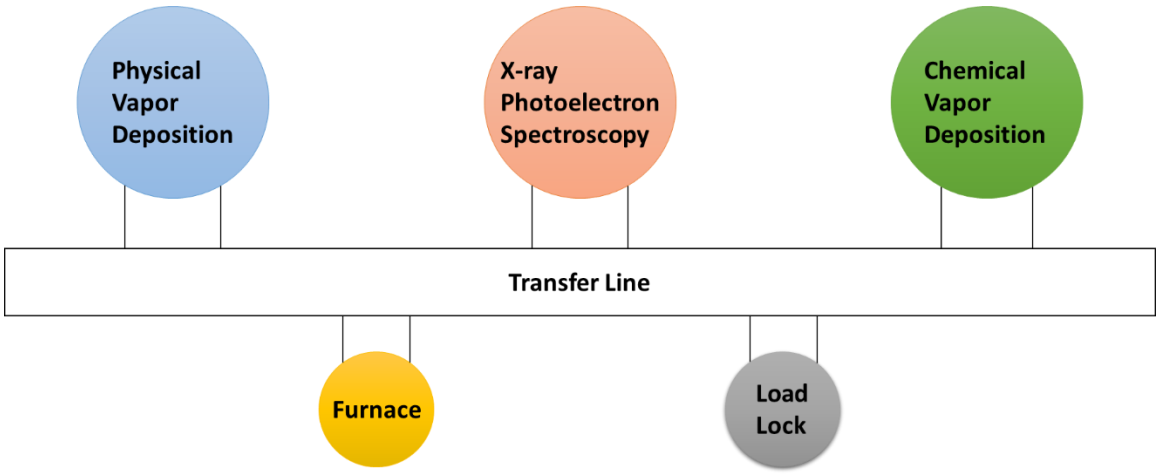

Figure 2.1: Schematic of the vacuum system that allows *in situ* transfer of samples between the growth chambers and an analysis chamber.

Growth experiments are performed in a spherical cold-wall stainless steel CVD chamber illustrated in Figure 2.2.[1–3] A 15 × 15 mm^2 piece of Si(001) with a chemical oxide SiO_2(150nm)/Si is placed in the center of the CVD chamber from the transfer chamber. The precursor is evaporated by heating tape wrapped on saturator and carried to the CVD chamber by a carrier gas flow before it decomposes on the substrate surface. The metal precursor is preheated in a sealed tube to its evaporating temperature and showered 25 mm above the substrate. It is carried by argon or hydrogen gas flowing through a warm manifold line and oil bath entrance. The temperatures of the manifold and oil bath vary with the precursor species, usually higher than the saturator and lower than their decomposition temperatures. The inhibitor gas is controlled by a mass flow controller and

flows into the system through the chamber sidewall. Before the deposition, the substrate is pre-heated for 20 min to arrive the growth temperature by the heating bulb [OSRAM halogen lamp] locating 5 mm below the substrate. During the deposition, the vaporized precursor adatoms adsorb on the substrate surface, thermally decompose and grow a metallic thin film. Other gas phase byproducts are exhausted from the CVD chamber by pumps and the deposition pressure in CVD reactor is at mTorr scale. After deposition, the chamber is isolated from all gas inputs, and samples cool to about 350 K over a 20-min period under 10^{-6} Torr vacuum and are then transferred to the XPS chamber.

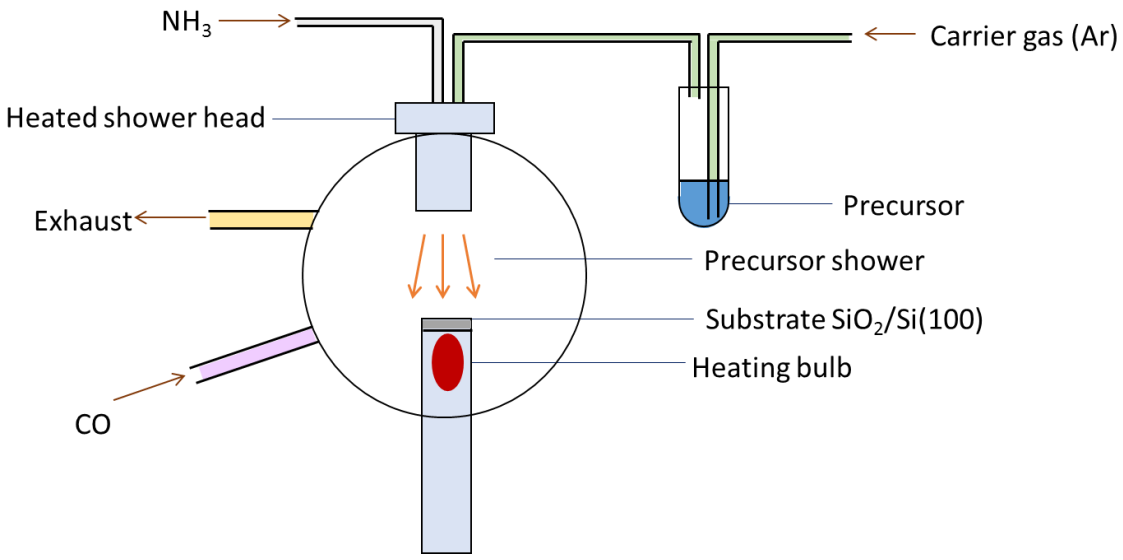

Figure 2.2: The schematic sketch of the CVD chamber used in this research.

The furnace is designed and built to study the surface chemistry of SiO_2/Si(100) substrate (Fig. 2.3). The quartz furnace tube is connected to the vacuum system with metal seal. The sample holder is made of molybdenum which has a melting point of 2896 K. To reduce the heat dissipation and to minimize the heat induced seal damage, a hollow ceramic rod [McMater-Carr] is employed under the Mo stage, connecting to the transfer arm. The furnace is surrounded by a cylinder heater on side and a flat heater on top [Omega]. Both radiant heaters are supported by a stainless steel frame from outside. Before the application, the substrate temperature is calibrated with the thermal couple reading in a fixed place between the furnace tube and the cylinder heater. During the annealing process, the temperature is handled by manipulating the power supply through a digital controller.

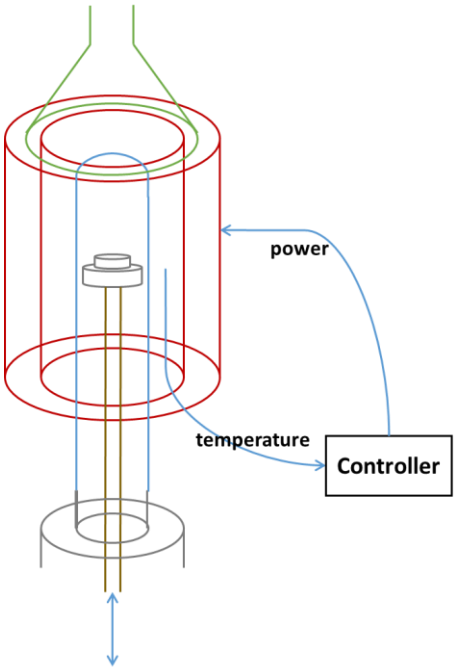

Figure 2.3: The schematic sketch of the furnace built for this research.

2.2 EXPERIMENTAL

2.2.1 Pretreatment

The substrate is cleaned chemically or thermally before the experiments. In the chemical method, the 15mm×15mm TEOS SiO_2 (1.5μm)/Si(100) substrates (Sylib Wafer 812AFBA) were cleaned in a piranha solution (H_2SO_4 : H_2O_2 : H_2O = 6 : 2 : 1) for 15 min, then in 2% HF for 10 s, and rinsed with deionized water. Then substrates are placed in a load lock and moved to an ultra-high vacuum transfer chamber at a pressure of 10^{-9}~10^{-10} Torr. In the thermal method, the wafer is moved into a quartz tube furnace through the transfer chamber and pre-annealed at 1173 K for 30 min at a pressure of 10^{-9}~10^{-10} Torr. After the annealing, > 90 % of the carbon contamination though loading process from air is removed from silica wafer surface. When the substrate cools down, it is moved to the center stage of the CVD chamber through the internal vacuum transportation. The thermal pretreatment in furnace is also used to control silica surface chemistry by annealing from 473 to 1193 K (Chapter 5).

2.2.2 $Ru_3(CO)_{12}$ (triruthenium dodecacarbonyl)

In Chapter 3, the wafer was radiantly heated at 573 K and 84 mTorr in flowing Ar for 1 hr before growth. $Ru_3(CO)_{12}$ (Sigma-Aldrich, 99%) was preheated to 358 K for 20 min in a sealed tube and showered 25 mm above the wafer, carried by 2.45 sccm Ar gas flowing through a 363 K manifold line and a 373 K oil bath entrance, which led to a precursor partial pressure of 12 mTorr in the chamber. CVD chamber pressure was monitored with a baratron gauge. The growth temperature was 473 K. The CO line was

controlled by a mass flow controller and flowed into the system through the chamber sidewall. In all processes, the total pressure was kept at 84 mTorr by regulating an Ar vent line.

In Chapter 4, the substrate was radiantly heated to the 448 K growth temperature. $Ru_3(CO)_{12}$ [Sigma-Aldrich, 99%] was preheated to 343 K in a saturator and admitted to the chamber 25 mm above the wafer using a showerhead heated to 373 K. Ar gas (7 standard cubic cm min^{-1}) carries the precursor through a 353 K manifold line to the showerhead and this leads to a precursor partial pressure of 47.2 mTorr in the chamber. CVD chamber pressure was monitored with a baratron gauge. The NH_3 line was controlled by a mass flow controller and entered the showerhead through separate tubing. Two growth times were used, 10 min for nucleation studies and 120 min for film growth studies.

In Chapter 5, $Ru_3(CO)_{12}$ [Sigma-Aldrich, 99%] was preheated to 358 K for 20 min in a sealed tube and showered 25 mm above the wafer, carried by 2.5 sccm Ar gas flowing through a 363 K manifold line and a 373 K oil bath entrance, which led to a precursor partial pressure of 12 mtorr in the chamber. Each substrate was placed in a load lock and moved into an ultra-high vacuum quartz tube and radiantly annealed at temperature from 473 to 1193 K for 1 hr before growth. Then the substrate was moved through the same ultra-high vacuum transfer chamber onto the center stage of the CVD vessel. CVD chamber pressure was monitored with a baratron gauge. The substrate was radiantly heated to growth temperature at 403 K in CVD chamber. The growth times were 10 min for nucleation studies using $Ru_3(CO)_{12}$.

2.2.3 Ru-amidinate (Ruthenium bis(*N,N'*-di-*tert*-butylacetamidinate) dicarbonyl)

In Chapter 5, ruthenium bis(*N,N'*-di-*tert*-butylacetamidinate) dicarbonyl (Ru(AMD)) precursor [Dow AccuDEP™ Ruthenium Precursor] was preheated to 383 K for 30 min in a sealed saturator and showered 25 mm above the wafer, carried by 10 sccm Ar gas flowing through a 423 K manifold line and oil bath entrance, which led to a precursor partial pressure of 45 mtorr in the chamber. Each substrate was radiantly annealed at 1173 K for 30 min in the ultra-high vacuum quartz tube before growth. The CO line was controlled by a mass flow controller and flowed into the system through the chamber sidewall at a partial pressure of 4 mTorr. The NH_3 line was controlled by a mass flow controller and flowed into the system on the top of the chamber through the same oil bath as the precursor in separate tubing at a partial pressure of 5 mTorr. To the study the initial of CVD, Ru are deposited by Ru(AMD) at 473 K and 523 K for 10 min. Since NH_3 boosts the growth rate in Ru(AMD) atomic layer deposition (ALD) as a coreactant,[4] deposition time varied depending on the use of CO or NH_3 to match the similar thickness for Ru film characterization. Thin Ru films were grown at 573 K for 30 min without NH_3 and for 25 min with NH_3. Also, thick Ru films were deposited at 623 K for 40 min without NH_3 and for 30 min with NH_3.

2.3 CHARACTERIZATION

2.3.1 X-ray photoelectron spectrometer

An *in situ* X-ray photoelectron spectrometer [Physical Electronics 3057; Mg Kα] is connected to the CVD vessel with an ultra-high vacuum transfer line. Film thickness is

calculated from the attenuation of a substrate feature intensity.[5,6] On thin Ru film (< 4 nm), the X-ray Photoelectron Spectroscopy (XPS) Si *2p* signal attenuation from blank silica substrate can be used to calculate the Ru thickness by referring NIST Effective-Attenuation-Length Database.[7] This quantitative XPS measurement assumes the films are ideally flat, while on the discontinuous films, the equivalent thickness is achieved comparing a smooth and uniform layer on the substrate.[8] For thick films, the XPS is used to monitor carbon and nitrogen content on the film surface before / after annealing, and inside the film after 60 s of Ar^+ ion sputtering.

According to "Handbook of X-ray Photoelectron Spectroscopy", carbon *1s* peak is positioned at 284.5 eV (page 40) and Ru 3d doublet splits 4.17 eV while Ru $3d_{5/2}$ peak is located at 280.1 eV for metallic ruthenium (page 114).[9] Therefore, Ru $3d_{3/2}$ peak overlaps the C *1s* peak at 284 eV binding energy and Ru $3d_{5/2}$ peak is independent at 280 eV in XPS spectra. Theoretically, the integrated peak area ratio of Ru $3d_{5/2}/3d_{3/2}$ is 3:2 due to the *d*-electrons spin-orbit interactions, corresponding to the lab measurements of high purity metallic Ru with XPS spectra fitted with Gaussian–Lorentzian natural line and Shirley baseline.[10–12]

Figure 2.4 is an example from Chapter 4 of a Ru film deposited by $Ru_3(CO)_{12}$ at 373 K for 2 hr. After 60 s of Ar^+ sputtering, the Ru film is scanned by the spectrometer in the 278 to 288 eV binding energy range. The carbon content is determined by fitting the Ru $3d_{3/2}$ and $3d_{5/2}$ XPS features at 284.3 eV and 280.1 eV, respectively, using Casa XPS 2.316 software [Casa Software Ltd].[9] The spectra were fitted three times (Fig. 2.5) and the data are listed in Table 2.1. We employed a Gausian-Lorentzian line shape and a Shirley

baseline. The C 1*s* XPS feature at 284.5 eV overlaps with the Ru $3d_{3/2}$ feature. The integrated peak area ratios for Ru $3d_{5/2}/3d_{3/2}$ are 1.50 and the carbon content is associated with the peak area at ~285 eV that exceeded the Ru $3d_{3/2}$ area based on this ratio.[10–12] Since the sensitivity factors for C and Ru of 0.296 and 4.273, respectively,[9] are quite different, small reproducibility errors in fitting the curves can lead to uncertainty of ± 2 % in determining the carbon content.

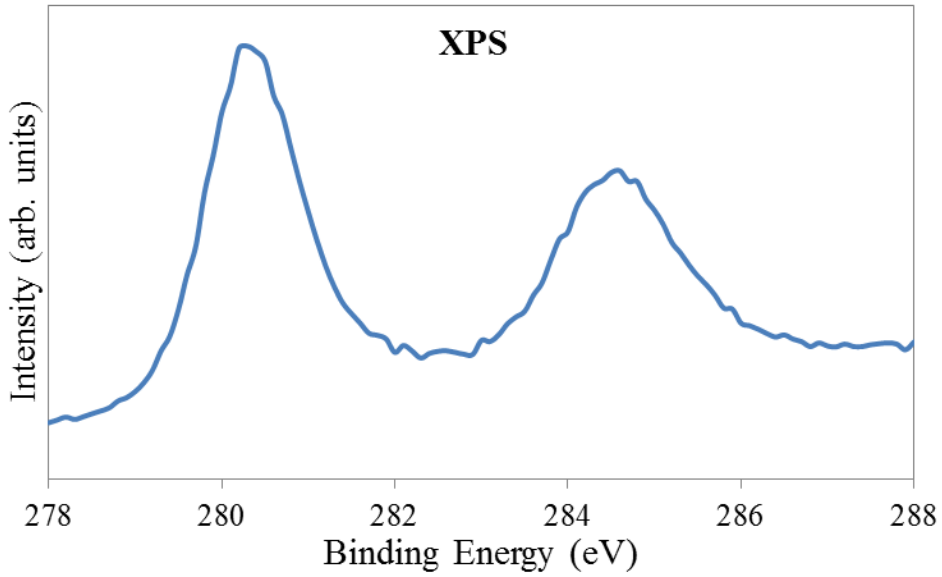

Figure 2.4: Ru film deposited by $Ru_3(CO)_{12}$ for 2 hr. XPS spectra of Ru/C after 60 s of Ar^+ sputtering.

(1)

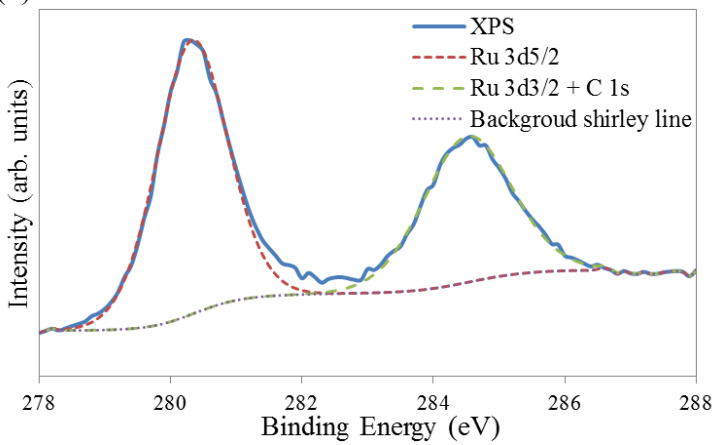

(2)

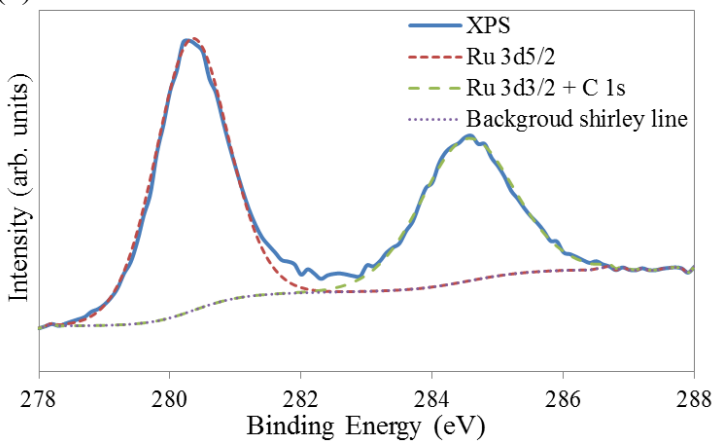

(3)

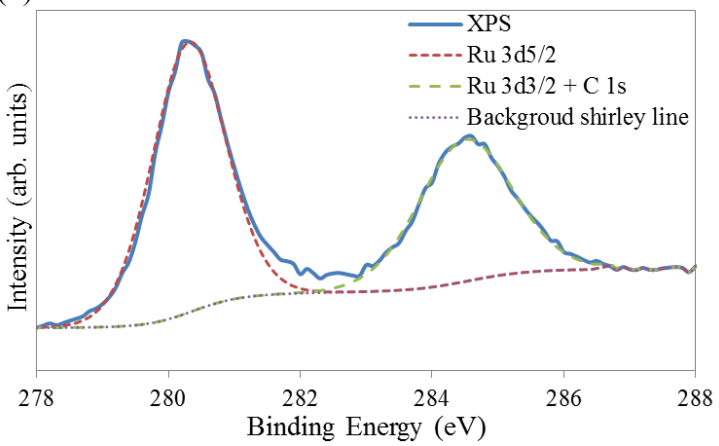

Figure 2.5: Peak fittings of Fig. 2.4 by CasaXPS software.

Fitting #	(1)		(2)		(3)	
Peak	Ru $3d_{5/2}$	Ru $3d_{3/2}$ (C $1s$)	Ru $3d_{5/2}$	Ru $3d_{3/2}$ (C $1s$)	Ru $3d_{5/2}$	Ru $3d_{3/2}$ (C $1s$)
Area	16401	10921	17121	11444	17098	11430
Area ratio	1.5018		1.4961		1.4959	
Component	Ru	C	Ru	C	Ru	C
Composition	100.69 %	-0.69 %	98.50 %	1.50 %	98.44 %	1.56 %

Table 2.1: Peak area ratios of Fig. 2.3 fittings by CasaXPS software.

2.3.2 X-ray reflectivity

Film thickness is measured by X-ray reflectivity (XRR) [Bruker-ABX D8 or Philips XPERT Theta-Theta Diffractometer]. On continuous films thicker than 4 nm, oscillation is observable from XRR, and the thickness is estimated by using the Kiessig fringe period.[13] The film thickness is estimated by Bragg's Law $d = \frac{\lambda}{2 \sin \Delta\theta}$, while λ = 1.542 Å is the wavelength of incident wave.[14] Film crystallinity of films is established using X-ray diffraction (XRD) [Bruker-ABX D8 and Philips XPERT Theta-Theta Diffractometer]. The crystallite grain size is calculated from XRD peaks using Scherrer equation $\tau = \frac{\lambda}{\beta \cos \theta}$, while β is the line broadening at half the maximum intensity (FWHM).[15] Figure 2.6 and 2.7 are the XRR and XRD scan examples from Chapter 5 on the Ru film deposited by the Ru(AMD) precursor at 623 K for 40 min.

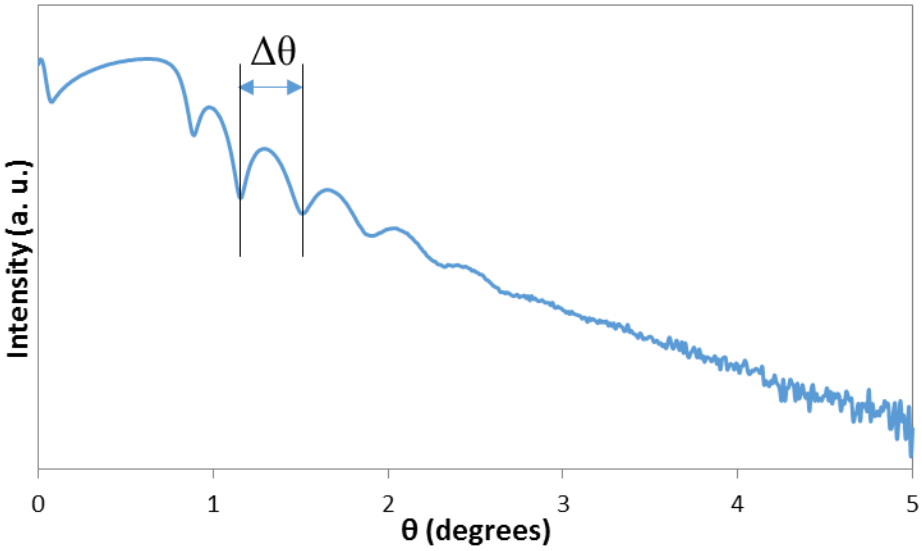

Figure 2.6: XRR example of Ru film deposited by Ru(AMD) precursor at 623 K for 40 min, which corresponds to a 25 nm thick Ru film (Δθ = 0.18).

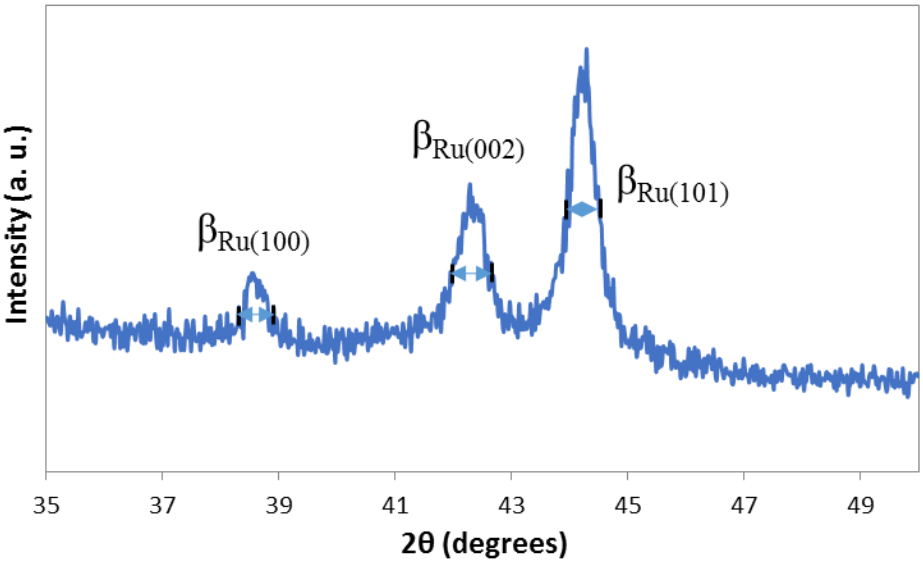

Figure 2.7: XRD example of a 25 nm Ru film deposited by Ru(AMD) precursor at 623 K for 40 min.

2.3.3 Atomic force microscopy and scanning electron microscopy

For *ex situ* characterization, the surface images for particle density and size distribution analysis are taken by scanning electron microscopy (SEM) [Zeiss Supra 40VP]. Atomic force microscopy (AFM) [Aligent Technologies 5500] is used to measure film roughness and the file is analyzed by Gwyddion software.

2.4 REFERENCES

1. Shin, J., Waheed, A., Winkenwerder, W. a., Kim, H.-W., Agapiou, K., Jones, R. A., Hwang, G. S. and Ekerdt, J. G. *Thin Solid Films* **515,** 5298–5307 (2007).

2. Shin, J., Kim, H.-W., Hwang, G. S. and Ekerdt, J. G. *Surf. Coatings Technol.* **201,** 9256–9259 (2007).

3. Henderson, L. B. and Ekerdt, J. G. *J. Electrochem. Soc.* **157,** D29–D34 (2010).

4. Li, H., Farmer, D. B., Gordon, R. G., Lin, Y. and Vlassak, J. *J. Electrochem. Soc.* **154,** D642–D647 (2007).

5. Shallenberger, J. R., Cole, D. A., Novak, S. W., Moore, R. L., Edgell, M. J., Smith, S. P., Hitzman, C. J., Kirchoff, J. F., Principe, E., Biswas, S., Bleiler, R. J., Nieveen, W. and Jones, K *1998 Int. Conf. Ion Implant. Technol. Proc. (Cat. No.98EX144)* **1,** 79–82 (1999).

6. Lewis, G. and Fox, P. G. *Corros. Sci.* **18,** 645–650 (1978).

7. Naumkin, A. V., Kraut-Vass, A., Gaarenstroom, S. W. and Powell, C. J., NIST Standard Reference Database 20, Version 4.1. *Measurement Services Division of the National Institute of Standards and Technology* (2012).

8. Jablonski, A. and Zemek, J. *Surf. Interface Anal.* **41,** 193–204 (2009).

9. Moulder, J. F., Stickle, W. F., Sobol, P. E. and Bomben, K. D., *Handbook of X-ray Photoelectron Spectroscopy*. (Perken-Elmer, Eden Prairie, MN, 1992).

10. Kim, H., Rabelo de Moraes, I., Tremiliosi-Filho, G., Haasch, R. and Wieckowski, A. *Surf. Sci.* **474,** L203–L212 (2001).

11. Lai, Y.-H., Chen, Y.-L., Chi, Y., Liu, C.-S., Carty, A. J., Peng, S.-M. and Lee, G.-H. *J. Mater. Chem.* **13,** 1999–2006 (2003).

12. Bost, D. E. and Ekerdt, J. G. *Thin Solid Films* **558,** 160–164 (2014).

13. Pietsch, U., Holy, V. and Baumbach, T., High-Resolution X-Ray Scattering From Thin Films to Lateral Nanostructures. (Springer Tracts in Modern Physics, 2004).

14. Mate, C. M., Yen, B.K., Miller, D.C., Toney, M.F., Scarpulla, M. and Frommer, J.E. *IEEE Trans. Magn.* **36,** 110–114 (2000).

15. Scherrer, P. *Math. Klasse* **2,** 98–100 (1918).

Chapter 3: Effect of CO on Ru Nucleation and Ultra-Smooth Thin Film Growth by Chemical Vapor Deposition at Low Temperature

3.1 INTRODUCTION

In recent decades, the advancements in integrated circuits (IC) to increase speed and reduce power have come about through reduction in device dimensions. A smooth ultra-thin diffusion barrier/liner is required to prevent copper from diffusing into the interlayer dielectric and electromigration within the vias and wire lines in IC devices.[1] Metallic Ru is a promising material in future designs due to its high conductivity (ρ_{Ru}= 6.7×10^{-6} Ω-cm), superior thermodynamical and chemical stability, plus the low solubility with Cu.[2–4] To minimize Cu diffusion through grain boundaries and improve Cu electroplating behavior on films, small Ru nanocrystalline grain size and a smooth film surface are desired in the semiconductor industry.[1]

Chemical vapor deposition (CVD) is a broadly used technology with advantages of high conformal coverage compared to physical sputtering and low temperature operation.[5] Representative Ru precursors used in the CVD process include $Ru(acac)_3$ (acac, acetylacetinate),[3,6] $Ru(CO)_4$(hfb) (hfb, hexafluoro-2-butyne),[7] $Ru(EtCp)_2$ (EtCp, ethylcyclopentadienyl),[8] and $Ru_3(CO)_{12}$.[3,9] Triruthenium dodecacarbonyl, $Ru_3(CO)_{12}$, is capable of decomposing to nanocrystalline Ru (001) completely with negligible carbon content and excellent film adhesion at temperature as low as 423K in the absence of any co-reacting gas.[1,9,10]

Metal growth on oxides in general and SiO_2 in particular during CVD typically leads to the formation of three-dimensional islands (Volmer-Weber growth mode) that coalesce

Liao, W., Ekerdt, J. G., "Effect of CO on Ru Nucleation and Ultra-Smooth Thin Film Growth by Chemical Vapor Deposition at Low Temperature", Chemistry of Materials 25, 1793–1799 (2013).

into a continuous film for a variety of reasons, including the unfavorable wetting associated with the high surface energy of the metal and the sparse nature of the nuclei from which the three dimensional islands grow.[11–13] Three-dimensional island growth combined with sparse nucleation leads to surface roughness and the deposition of more metal mass than is needed to form a film of sufficient thickness to function as a copper diffusion barrier when compared to a uniformly-thick metal film.[14] Growth chemistries that feature small and dense Ru nuclei result in a thinner and smoother metal film than observed when big and sparse island merge with continued Ru deposition.[15] Iodine sources, such as CH_3I[15,16] and C_2H_5I,[16,17] in concert with $Ru(EtCp)_2$ are shown to enhance the nucleation density dramatically so as to improve film smoothness. Iodine worked with a Ru precursor that also needed co-reacting O_2 and may have functioned by surface segregating to the Ru surface and inhibiting oxygen adsorption on nucleated islands, which forced additional nuclei to form.[15]

This study explores the use of inhibitors that can block adsorption of the metal precursor or a co-reactant, and function when O_2 is not the co-reactant. Carbon monoxide (CO) has the potential to occupy the surface of Ru islands and thereby encourage addition nucleation on the oxide substrate surface. As one of the potential Fischer–Tropsch synthesis catalysts,[18] the adsorption[19] and dissociation[20] of CO on various Ru crystal surfaces, including Ru(001),[21–23] Ru(109),[24] Ru(11$\bar{2}$0),[25] Ru(11$\bar{2}$1),[26] have been reported. Carbon monoxide can also adsorb at hydroxyl Si sites on SiO_2.[27–29]

3.2 EXPERIMENTAL

Growth experiments were performed in a spherical cold-wall stainless steel CVD chamber described previously.[30–32] The 15mm×15mm TEOS SiO_2 (1.5μm)/Si(100) substrates (Sylib Wafer 812AFBA) were cleaned in a piranha solution (H_2SO_4 : H_2O_2 : H_2O = 6 : 2 : 1) for 15 min, then in 2% HF for 10 s, and rinsed with deionized water. Each substrate was placed in a load lock and moved through an ultra-high vacuum transfer chamber onto the center stage of the CVD vessel. Then the wafer was radiantly heated at 573 K and 84 mTorr in flowing Ar for 1 hr before growth. $Ru_3(CO)_{12}$ (Sigma-Aldrich, 99%) was preheated to 358 K for 20 min in a sealed tube and showered 1 in above the wafer, carried by 2.45 sccm Ar gas flowing through a 363 K manifold line and a 373 K oil bath entrance, which led to a precursor partial pressure of 12 mTorr in the chamber. CVD chamber pressure was monitored with a baratron gauge. The growth temperature was 473 K. The CO line was controlled by a mass flow controller and flowed into the system through the chamber sidewall. In all processes, the total pressure was kept at 84 mTorr by regulating an Ar vent line.

An *in situ* X-ray photoelectron spectrometer [Physical Electronics 3057; Mg Kα], connected to the CVD vessel with an ultra-high vacuum transfer line, was used to monitor carbon content in the film after 60 s Ar^+ ion sputtering. For *ex situ* characterization, the surface images for particle density and size distribution analysis were taken by scanning electron microscopy (SEM) [Zeiss Supra 40VP], and atomic force microscopy (AFM) [Aligent Technologies 5500] was used to measure roughness. Film thickness was measured

by X-ray reflectivity (XRR) [Bruker-ABX D8]. Film crystallinity of films was established using grazing angle (0.5°) X-ray diffraction (XRD) [Bruker-ABX D8].

3.3 RESULTS

3.3.1 Ru nanoparticle nucleation

CO flows sufficient to realize 2.5 mTorr and 8.4 mTorr in the CVD chamber, were used and compared against the growth that did not add CO. CO was introduced at different times for 5 min periods, as well as during the entire 15 min growth time. SEM images in Figure 3.1 show the different Ru particle distributions at every growth condition, Table 3.1 and Figure 3.2 present tabulated and graphical illustrations of the trends, respectively. When CO and $Ru_3(CO)_{12}$ are fed simultaneously for the entire 15 min, the metallic Ru particles get larger and density decreases with increasing CO partial pressure, from 8.9×10^{11} /cm² without CO to 7.7×10^{11} /cm² or 6.3×10^{11} /cm². In all instances, adding CO after nucleation is initiated without CO increases the particle density and decreases the particle size. The effect on increasing density and decreasing particle size is greatest for CO addition in the last 5 min.

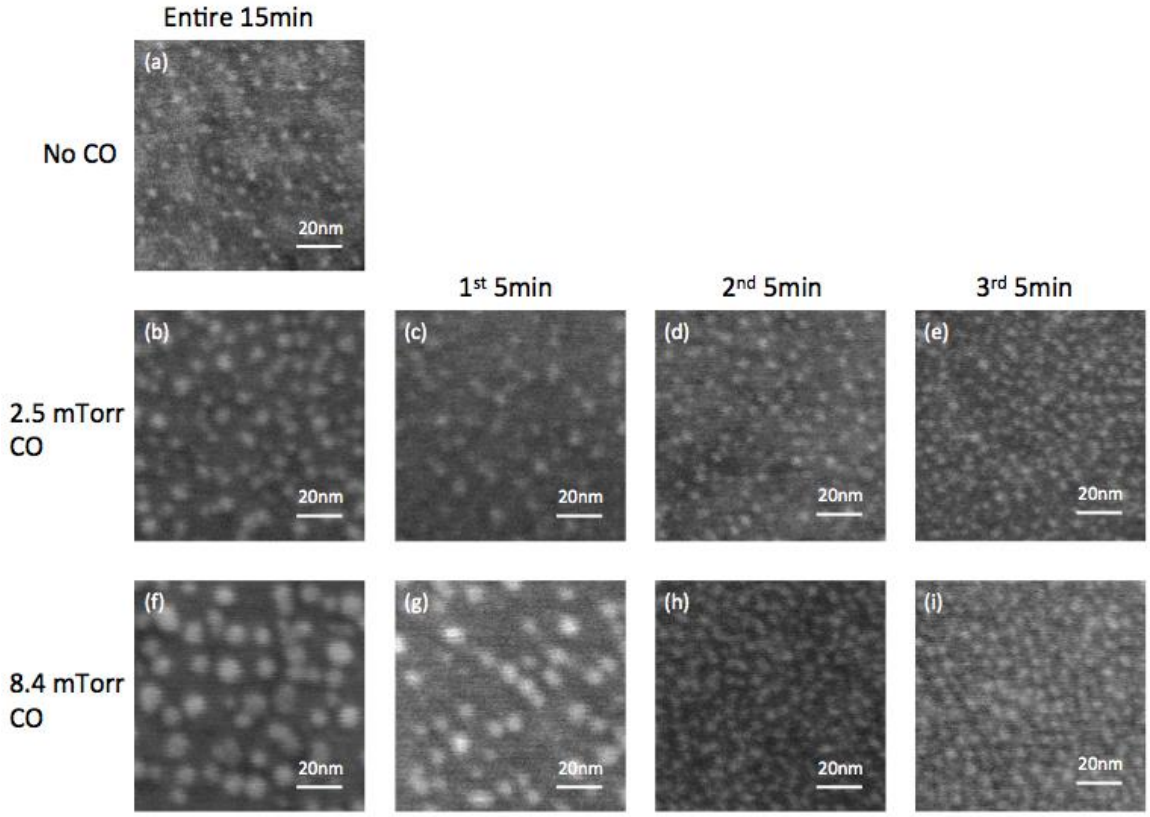

Figure 3.1: SEM images of Ru CVD at 473 K, 84 mTorr on TEOS Si substrates (a) without CO, and with (b) 2.5 mTorr CO, (f) 8.4 mTorr CO for entire 15 min; 2.5 mTorr partial pressure CO addition to CVD chamber (c) at 1st 5 min, (d) at 2nd 5 min, (e) at 3rd 5 min; 8.4 mTorr partial pressure CO addition at (g) 1st, (h) 2nd, and (e) 3rd 5 min during the 15 min growth.

No CO	15min
Density ($\times 10^{11}$/cm^2)	8.9
Diameter (nm)	4.38±0.56

P_{CO} =2.5 mTorr	15min	1st 5min	2nd 5min	3rd 5min
Density ($\times 10^{11}$/cm^2)	7.7	6.2	9.9	16.3
Diameter (nm)	6.15±0.83	5.23±0.71	4.47±0.72	4.17±0.74

P_{CO} =8.4 mTorr	15min	1st 5min	2nd 5min	3rd 5min
Density ($\times 10^{11}$/cm^2)	6.3	5.1	13.9	16.4
Diameter (nm)	7.43±1.48	7.15±0.94	4.28±0.67	4.32±0.72

Table 3.1: Ru nanoparticle densities, number per cm^2, and sizes for growthes at 473 K.

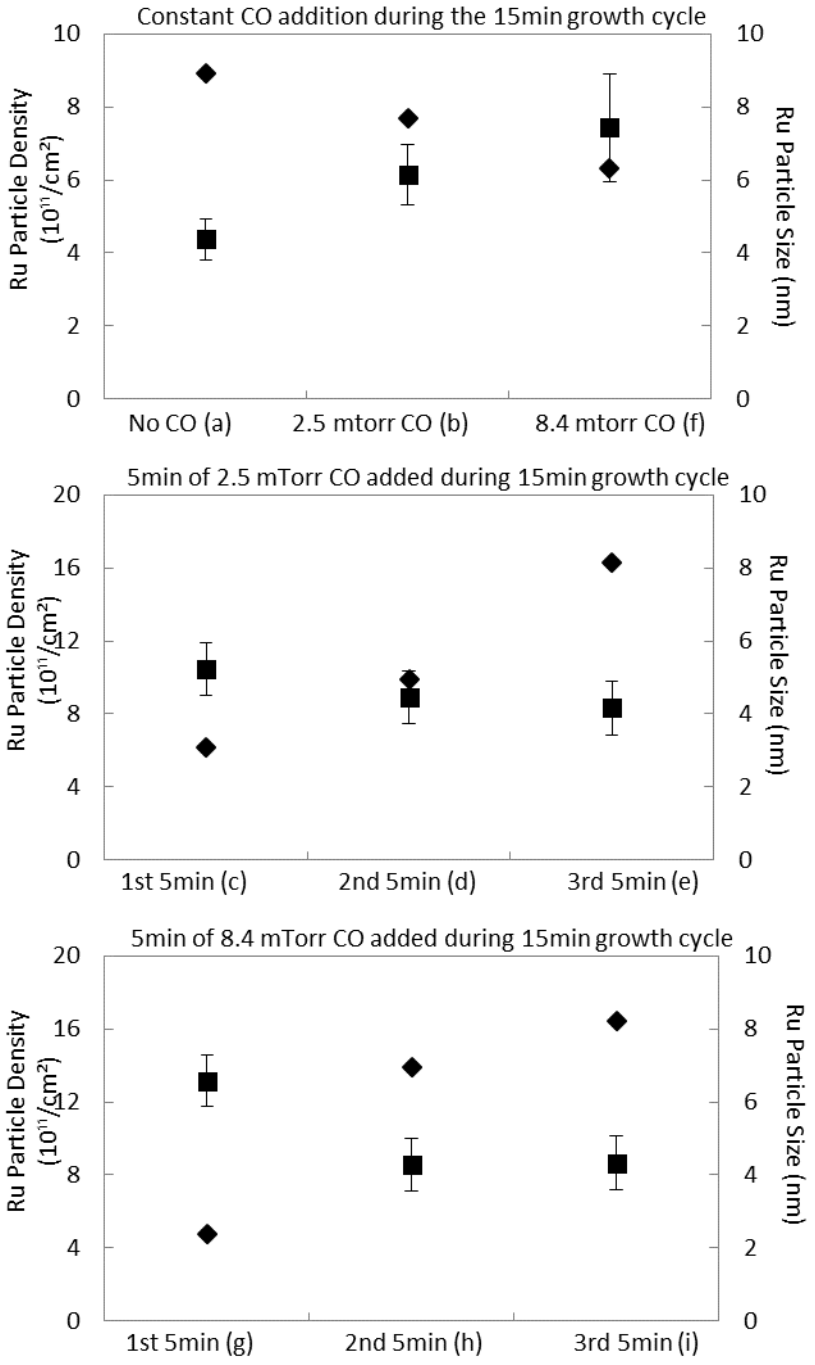

Figure 3.2: Graphical trends of Ru nanoparticle density (♦), number per cm^2, and diameter distribution (□) corresponding to Images (a) - (i) in Figure 3.1.

As observed in Figures 3.1 and 3.2, the lowest density is obtained by adding 8.4 mTorr CO from the beginning. To explore the unexpected density decline with more CO participation, additional experiments were performed. The first 15 min nucleation condition, presented in Figure 3.3 (a), is reproduced from Fig. 3.1 (g), in which 8.4 mTorr of CO was added for the first 5 min of growth followed by a 10 min period of growth without CO. Similar starting conditions of 8.4 mTorr of CO and $Ru_3(CO)_{12}$ were employed and then growth was continued for 25 and 55 min without CO, *i.e.*, the total growth times are 30 (Fig 3.3b) and 60 (Fig 3.3c) min, respectively. As illustrated in the Figure 3.3 SEM images, considerable small Ru particles nucleate between primary sparse big nuclei and grow during deposition. The densities of particles with diameters above and below 5 nm are counted separately and presented in Figure 3.3d. The density of metallic Ru particles larger than 5 nm diameter increases moderately from 3.9×10^{11} /cm² to 5.6×10^{11} /cm², while the visible particles smaller than 5 nm increase dramatically from 0.7×10^{11}/cm² to 7.5×10^{11}/cm² along with the deposition time.

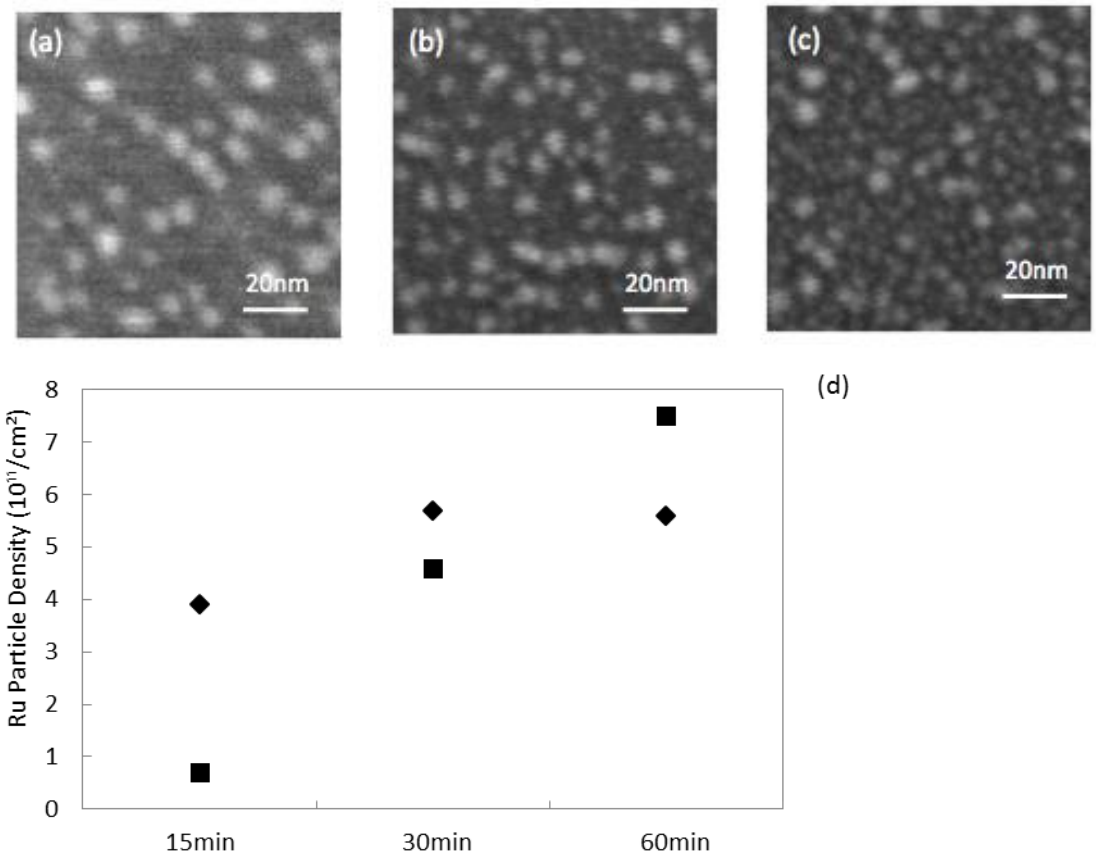

Figure 3.3: SEM images of Ru deposition at 473 K when 8.4 mTorr partial pressure CO was injected for the first 5 min of Ru nucleation and growth before continuously growing Ru without CO for total of (a) 15 min (b) 30 min, and (c) 60 min. Graphical trends (d) of the nucleation densities for Ru particle diameters above (♦) and below (□) 5 nm corresponding to each deposition time.

3.3.2 Ultra-thin metallic Ru film growth.

Among the experiments in Figure 3.1, no CO addition in first 10 min followed by 5 min with CO at 8.4 mTorr partial pressure, produces the highest density (16.4×10^{11} /cm²) during the 15 min deposition. A comparison of 120 min growth without CO, and 10 min of growth without CO during the nucleation phase followed by 110 min of growth with an overpressure of 8.4 mTorr CO deposition was conducted to explore to the effect of CO on island coalescence. SEM images in Figure 3.4 and AFM pictures in Figure 3.5 reveal larger features and a rougher surface for growth without CO (Figure 3.5a) than the film grown with 8.4 mTorr CO (Figure 3.5b). Film thickness is calculated by the angles between two peaks in the XRR pattern (Figure 3.6). The film grown without added CO is 5.5 nm thick with a root-mean square (RMS) roughness of 0.51 nm, while the 8.4 mTorr CO deposited film is 4.7 nm thick and 0.25 nm RMS roughness. CO addition during Ru deposition on the SiO_2 substrate decreases the grow rate by 15% in this case, and reduces film roughness by half. Besides the surface topology, by comparing the XRD crystallinity peak sharpness in Figure 3.7, the size of the 8.4 mTorr CO film (Figure 3.7b) nanocrystals are smaller than for growth without CO (Figure 3.7a). The measured peak full width at half maximum (FWHM) and calculated crystallite size by the Scherrer Formula are produced in Table 3.2. Furthermore, the X-ray photoelectron spectroscopy Ru $3d_{3/2}$ and Ru $3d_{5/2}$ peak ratios after 60 s of Ar^+ sputtering (Figure 3.8) indicate no observable carbon contaminant is introduced by CO into the Ru films; the peak area ratio $3d_{5/2}/3d_{3/2}$ is 1.5; which is the predicted value for Ru.[33]

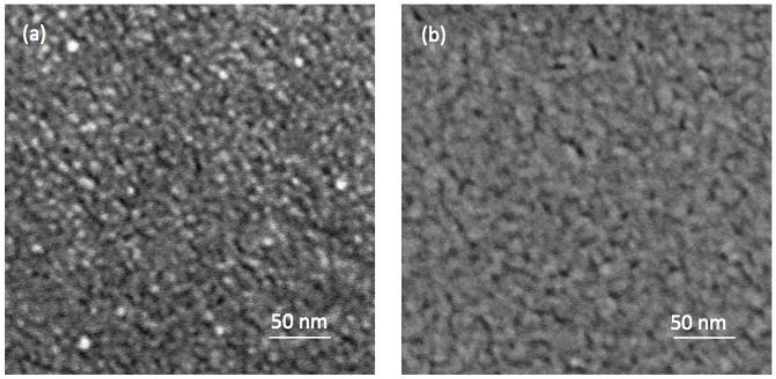

Figure 3.4: SEM images of 2 hr Ru deposition at 473 K, 84 mTorr (a) without CO, and (b) with 8.4 mTorr CO after initial growth for 10 min without CO.

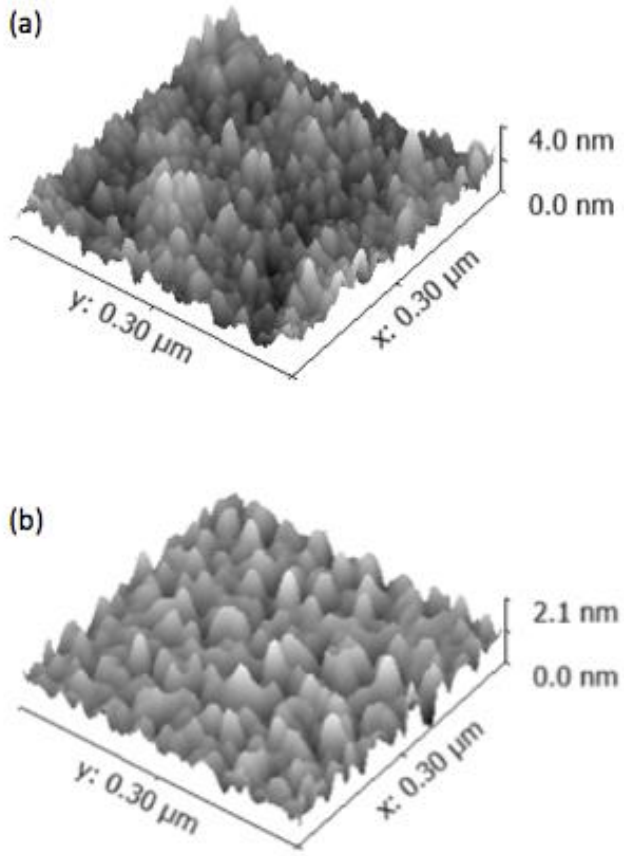

Figure 3.5: 3D AFM images of 2 hr Ru deposition at 473 K, 84 mTorr (a) without CO, and (b) with 8.4 mTorr CO after initial growth for 10 min without CO.

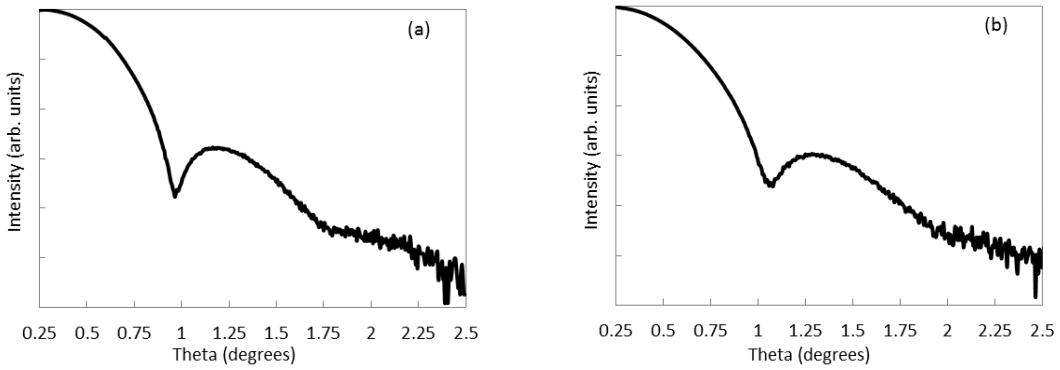

Figure 3.6: XRR spectra of 2 hr Ru deposition at 473 K and 84 mTorr (a) without CO, and (b) with 8.4 mTorr CO after growth for initial 10 min without CO.

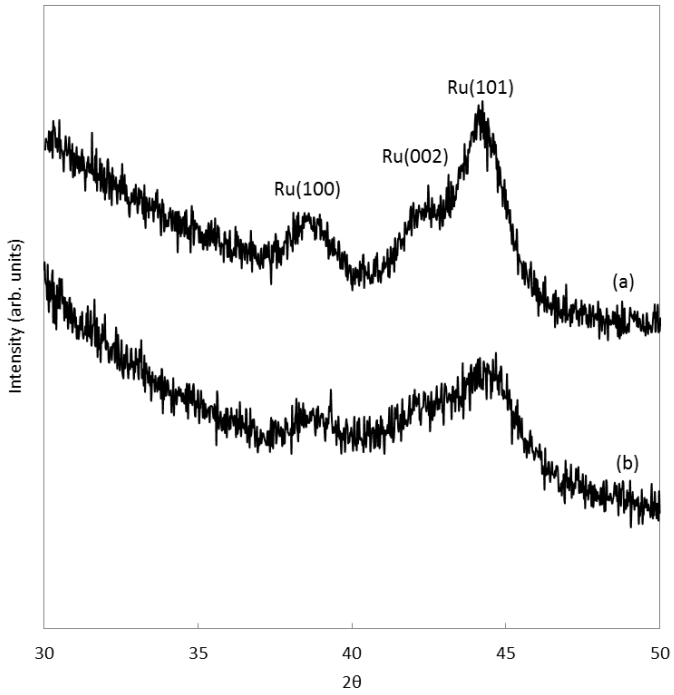

Figure 3.7: Grazing angle (0.5°) XRD spectrum of of 2 hr Ru deposition at 473 K and 84 mTorr (a) without CO, and (b) with 8.4 mTorr CO after initial growth for 10 min without CO.

		Ru (100)	Ru (002)	Ru (101)
Without CO	FWHM (deg)	1.5	1.4	1.9
	Crystallite size (nm)	5.46	5.92	4.39
With CO	FWHM (deg)	1.6	1.8	2.2
	Crystallite size (nm)	5.12	4.61	3.79

Table 3.2: Ru nanoparticle densities, number per cm^2, and sizes for growths at 473 K.

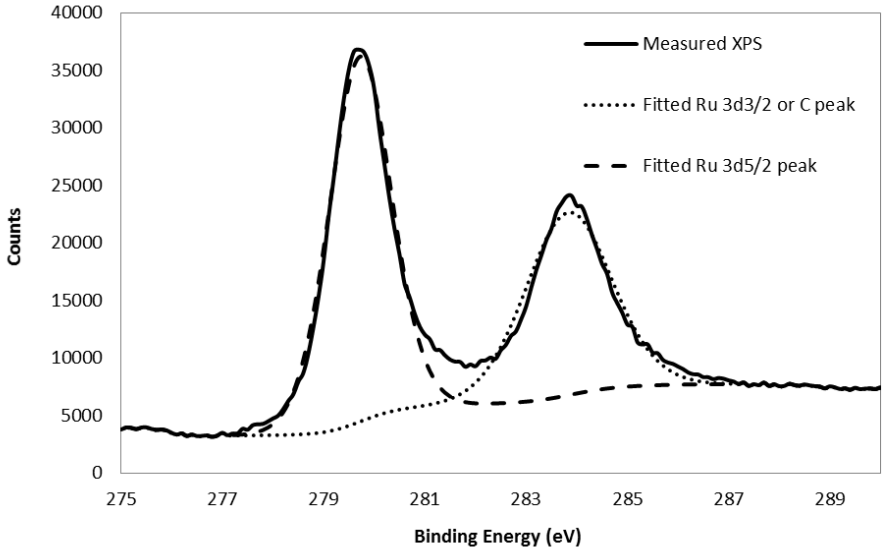

Figure 3.8: Ru/C XPS of CVD Ru film deposited with CO after 60 s Ar^+ ion sputtering.

3.4 DISCUSSION

Carbon monoxide was selected as a potential Ru surface inhibitor because it adsorbs reversibly to Ru surfaces in the temperature ranges for growth.[19,21,23] CO adsorption and dissociation are reversible on Ru surfaces at temperatures between 127 and 327 °C.[20] The premise of this study was to introduce CO at a sufficient overpressure to block the $Ru_3(CO)_{12}$ precursor from adsorbing on Ru that was occupied with adsorbed CO or for CO to compete with $Ru_3(CO)_{12}$ for Ru adsorption sites and thereby force new Ru nuclei to form on the SiO_2 surface. Higher nucleation densities were realized with CO addition and some form of inhibition/blocking was responsible. The sequence of CO addition relative to $Ru_3(CO)_{12}$ addition is important because both CO and $Ru_3(CO)_{12}$ also react with hydroxyl groups on SiO_2. Too high a CO overpressure can adversely affect nucleation by blocking SiO_2 sites where nucleation may initiate, as in Fig. 3.1 (b) and (f).

The $Ru_3(CO)_{12}$ precursor is reasoned to react with SiO_2 hydroxyl groups forming unstable $HRu_3(CO)_{10}(OSi\leqslant)$ grafted clusters that thermally decompose to metallic ruthenium.[34,35] $HRu_3(CO)_{10}(OSi\leqslant)$ can also continue to react with SiOH groups.[34] Additionally, $Ru_3(CO)_{12}$ is reasoned to thermally decompose directly to give Ru once the SiOH groups are consumed.[35] Carbon monoxide gas weakly adsorbs on free hydroxyls of SiO_2[27] to produce the H-bonded complex illustrated in Figure 3.9.[28] Beebe et al. illustrated the physical adsorption of CO on silanol at 150 °C and a CO pressure of 40 torr through infrared spectroscopy.[27]

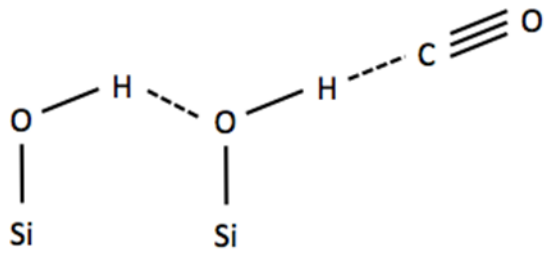

Figure 3.9: The complex structure of physisorbed CO on aerosol, adapted from G. Ghlotti, et al.[29]

The studies reported herein can be described with the reaction scheme shown in Figure 3.10. When $Ru_3(CO)_{12}$ and CO are incident on a SiO_2 surface, $Ru_3(CO)_{12}$ will interact irreversibly to form Ru adatoms that somehow nucleate into growing Ru islands/particles and CO will interact reversibly to form a complex (Figure 3.9) that blocks free hydroxyl from reacting with $Ru_3(CO)_{12}$, as illustrated in the top row in Figure 3.10. With continued $Ru_3(CO)_{12}$ exposure the Ru islands can grow larger by direct reaction of $Ru_3(CO)_{12}$ with the already formed Ru islands or by incorporating additional Ru that forms by reaction(s) of $Ru_3(CO)_{12}$ with SiO_2, as in Figure 3.10 left column. Carbon monoxide formed during $Ru_3(CO)_{12}$ decomposition or added to the reactor can compete with $Ru_3(CO)_{12}$ for adsorption sites on Ru islands or free hydroxyls on SiO_2 through reversible adsorption processes. The extent to which CO inhibits $Ru_3(CO)_{12}$ adsorption depends on the partial pressure of CO. The top plot in Figure 3.2 illustrates the density decreases from 8.9×10^{11} /cm² to 6.3×10^{11} /cm² and the Ru particle size increases from 4.38±0.56 nm to

7.43±1.48 nm as CO blocks the silica hydroxyl groups at a CO partial pressure of 8.4 mTorr when $Ru_3(CO)_{12}$ and CO are simultaneously put into the system from the beginning.

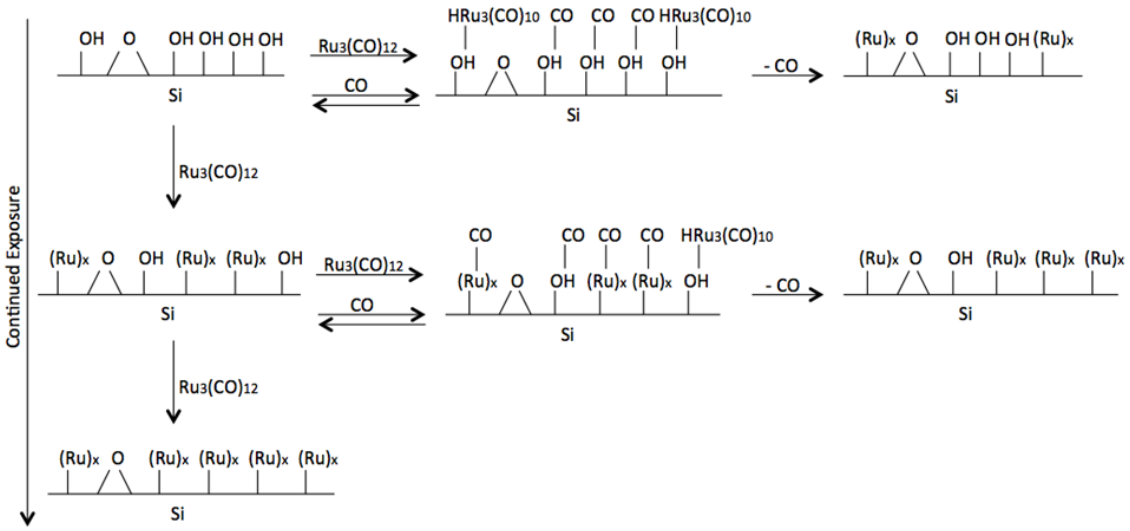

Figure 3.10: Schematic diagram of CO addition to Ru CVD at different times compared to deposition without CO.

As soon as the CO source was terminated (Figure 3.3), the physisorbed CO desorbs from the SiO_2 substrate and the $Ru_3(CO)_{12}$ reacts with the more abundant free hydroxyl groups rather than the sparse Ru particles. Eventually Ru nuclei grow in three dimensions with continued deposition. The appearance change to large particles is relatively minor

compared to the enhancement in volume and number for the small particles (Figures 3.3b and 3.3c). The density of small particles (diameter < 5 nm) increased much faster than the density of larger particles (diameter > 5 nm) as illustrated in Figure 3.3d, which suggests Ru is nucleated efficiently on the free hydroxyls that form once CO desorbs from the H-bonded SiOH-CO complex.

To avoid the competition between CO and $Ru_3(CO)_{12}$ on the SiO_2 substrate at the start of growth, CO was introduced after Ru adatoms and nanoparticles occupied the free hydroxyl groups. The later CO is injected into the system, the more completely Ru reacts with the hydroxyls as long as the silica hydroxyls are not saturated with metallic Ru. As observed in Figure 3.1 (c) to (e), Figure 3.1 (g) to (i), and the trend plots in Figure 3.2, the nucleation density increases as the CO addition period is delayed for the same total deposition time and CO injection dose. After 5 min of Ru deposition without CO, the silica hydroxyls have only partially reacted with $Ru_3(CO)_{12}$ to produce Ru adatoms and Ru nanoparticles and the CO overpressure addition at this time adsorbs not only on Ru adatoms and nanoparticles but also acts to block SiOH on the SiO_2 substrate, which impedes both growth on Ru and precursor dissociation at hydroxyl sites (Figure 3.10, middle row). After 10 min of Ru deposition without CO, sufficient free hydroxyls have reacted with $Ru_3(CO)_{12}$, and the added CO now adsorbs on the Ru metal surfaces and likely facilitates an additional, lower probability reaction channel through which the Ru precursor dissociates and nucleates particles on the SiO_2 surface.

CO partial pressure has an effect on the nucleation density. The maximum Ru particle density for 15 min growth runs was achieved by adding 8.4 mTorr CO in the last

5 min of growth (Table 3.1) as discussed further below. The starting point for Figures 3.1d and 3.1h was the same (5 min of growth without CO) and higher CO pressure led to a significantly higher Ru nanoparticle density and smaller average particle size. The ability for CO to form a complex with free hydroxyl groups increases with pressure as suggested by Beebe et al.[27] and 8.4 mTorr CO overpressure may have been sufficient to block free hydroxyls to a greater degree than the 2.5 mTorr overpressure. CO is expected to adsorb on Ru at both pressures and again a higher average coverage of CO should be expected for the higher CO overpressure. The combination of blocked free hydroxyl groups and CO adsorption on Ru surfaces is the likely reason the density of 13.9×10^{11} /cm^2 was observed in Figure 3.1h (Table 3.1).

The maximum Ru nucleation density is achieved by adding 8.4 mTorr CO in the last 5 min of the 15 min growth runs. Although the statistical density of 16.4×10^{11} nanoparticles /cm² by adding 8.4 mTorr CO in last 5 min in Figure 3.1i is only little more than that density of 16.3×10^{11} nanoparticles /cm² by adding 2.5 mTorr CO in last 5 min (Figure 3.1e), some of the larger particle shapes suggest Ru nanoparticles are beginning to coalesce by the end of the 15 min growth run.

With more nucleation and less distance between particles on the substrate, the island volume required to coalesce into continuous film is smaller, so that the coalesced film is smoother than the film coalesced from sparse large islands.[13] As illustrated in Figures 3.4 and 3.5, the film grown with 8.4 mTorr CO addition after presumably consuming most of the free hydroxyl groups in the first 10 min is thinner and smoother than the film grown without CO addition. During the growth CO blocks the Ru surface and

this decreases the precursor yield and film accumulation rate. CO disproportionation to carbon and CO_2 may have occurred, however carbon accumulation could not be detected by XPS. CO also successfully reduces the metallic Ru nanocrystallite size by 15% on average which may help prevent Cu diffusion through grain boundaries more efficiently. More experiments are required to be optimized the sequence and CO overpressure to control the nucleation density and the metallic film roughness and to determine the general applicability of CO to enhance nucleation for precursors that do not have such a high reactivity with hydroxyl groups as does $Ru_3(CO)_{12}$.

3.5 CONCLUSION

CO competes with $Ru_3(CO)_{12}$ for free hydroxyl adsorption. When CO and the Ru precursor are added to the CVD reaction chamber simultaneously at the beginning, the overpressure of CO reduces Ru nanoparticle density by limiting the Ru adatom formation at hydroxyl sites. CO also adsorbs on Ru nanoparticles, slowing their growth and facilitating additional, lower probability reactions between the $Ru_3(CO)_{12}$ precursor and the SiO_2 substrate; this new path to Ru adatoms leads to additional Ru island formation competitively with addition of Ru to existing nanoparticles, enhancing nucleation density. A higher nucleation density and smoother Ru film is achieved in CVD with CO addition during growth. The CO addition to $Ru_3(CO)_{12}$ deposition at proper timing and effective partial pressure reduces the film growth rate, surface roughness and nanocrystalline grain size by chemical vapor deposition.

3.6 REFERENCES

1. Kaloyeros, A. E.; Eisenbraun, E, *Annu. Rev. Mater. Sci.* **2000**, *30,* 363-385.

2. Goswami, I.; Laxman, R. *Semicond. Int.* **2004**, *27*, 49-54.

3. Green, M.L.; Gross, M.E.; Papa, L.E.; Schnoes, K.J.; Brason, D. *J. Electrochem. Soc.: Solid-State Sci. Technol.* **1985**, *132*, 2677-2685.

4. Kim, H. *Surf. Coat. Technol.* **2006**, *200*, 3104-3111.

5. Crowell, J.E. *J. Vac. Sci. Technol.* **2003**, *21*, S88-S95.

6. Viguie, J.C.; Spitz, J. *J. Electrochem. Soc.* **1975**, *122*, 585-588.

7. Senzaki, Y.; Gladfelter, W.L.; McCormick, F.B. *Chem, Mater.* **1993**, *5*, 1715-1721.

8. Matsui, Y.; Hiratani, M.; Nabatame, T.; Shimamoto, Y.; Kimura, S. *Electrochem. Solid-State Lett.* **2001**, *4*, C9-C12.

9. Aoyama, T.; Eguchi, K. *Jpn. J. Appl. Phys.* **1999**, *38*, L1134-L1136.

10. Wang, Q.; Ekerdt, J.G.; Gay, D.; Sun, Y.; White, J.M. *Appl. Phys. Lett.* **2004**, *84*, 1380-1382.

11. Boyd, E.P.; Ketchum, D. R.; Deng, H.; Shore, S.G. *Chem. Mater*. **1997**, *9*, 1154-1158.

12. Ratsch, C.; Venables, J. A. *J. Vac. Sci. Technol.* **2003**, *A21*, S96-S109.

13. Witten Jr., T. A.; Sander, L. M. *Phys. Rev. Lett.* **1981**, *47*, 1400-1403.

14. Brune, H. *Surf. Sci. Rep.* **1998**, *31*, 121-229.

15. Park, S.; Kim, H.; Kim, K.; Min, S. *Electrochem. Solid-State Lett.* **1998**, *1*, 262-264.

16. Thom, K.M.; Ekerdt, J.G. *Thin Solid Films* **2009**, *518*, 36-42.

17. Kim, J.J.; Jung, D.H.; Kim, M.S.; Kim, S.H.; Yoon, D.Y. *Thin Solid Films* **2002**, *409*, 28-32.

18. Kim, J.J.; Kim, M.S.; Yoon, D.Y. *Chem. Vap. Deposition* **2003**, *9*,105-109.

19. Schulz, H. *Appl. Catal.* **1999**, *186*, 3-12.

20. Davydov, A. A.; Bell, A. T. *J. Catalyst.* **1977**, *49*, 332-344.

21. Strebel, C.; Murphy, S.; Nielsen, R.M.; Nielsen, J.H.; Chorkendorff, I. *Phys. Chem. Chem. Phys.* **2012**, *14*, 8005-8012.

22. Pfnur, H.; Menzel, D. *J. Chem. Phys.* **1983**, *79*, 2400-2010.

23. Pfnur, H.; Feulner, P.; Engelhardt, H.A.; Menzel, D. *Chem. Phys. Lett.* **1978**, *59*, 481-486.

24. Thomas, G.E.; Weinberg, W.H. *J. Chem. Phys.* **1979**, *70*, 1437-1439.

25. Zubkov, T.; Morgan, G.A.; Yates, J.T.; Kuhlert, O.; Lisowski, M.; Schillinger, R.; Fick, D.; Jansch, H.J. *Surf. Sci.* **2003**, *52*, 657-71.

26. Wang, J.; Wang, Y.; Jacobi, K. *Surf. Sci.* **2001**, *488*, 83-89.

27. Fan, C.Y.; Bonzel, H.P.; Jacobi. K. *J. Chem. Phys.* **2003**, *118*, 9773-9782.

28. Beebe, T.P.; Gelin, P.; Yates, Jr., J.T. *Surf. Sci.* **1984**, *148*, 526-550.

29. G. Ghiottl, E. Garrone, C. Morterra, F. Boccuzzl, J. Phys. Chem. 83 (1979) 2863.

30. Ugliengo, P.; Saunders, V.R.; Garrone, E. *J. Phys. Chem.* **1989**, *93*, 5210-5215.

31. Shin, J.; Waheed, A.; Winkenwerder, W.A.; Kim, H.; Agapiou, K.; Jones, R.A.; Hwang, G.S.; Ekerdt, J.G. *Thin Solid Films* **2007**, *515*,5298-5307.

32. Shin, J.; Kim, H.; Hwang, G.S.; Ekerdt, J.G. *Surf. Coat. Technol.* **2007**, *201*, 9256-9259.

33. Henderson, L.B.; Ekerdt, J.G. *J. Electrochem. Soc.* **2010**, *157*, D29-D34.

34. Kim, H.; Rabelo de Moraes, I.; Tremiliosi-Filho, G.; Haasch, R.; Wieckowski, A. *Surf. Sci.* **2001**, *474*, L203-L212.

35. Theolier, A.; Choplin, A.; D'Ornelas, L.; Basset, J.M.; Ugo, R.; Psaro, R.; Sourisseau, C. *Polyhedron* **1983**, *2*, 119-121.

36. Zanderighi, G.M.; Dossi, C.; Ugo, R.; Psaro, R.; Theolier, A.; Choplin, A.; D'Ornelas, L.; Basset, J.M. *J. Organomet. Chem.* **1985**, *296*, 127-146.

Chapter 4: Ru Nucleation and Thin Film Smoothness Improvement with Ammonia during Chemical Vapor Deposition

4.1 INTRODUCTION

As feature sizes in microelectronic devices decrease, ultra-thin (< 3 nm) and smooth diffusion barriers are required to prevent copper from diffusing into the surrounding dielectric layers and to limit electron scattering at the copper-liner surface.[1,2] The thin barrier films in future technology nodes are expected to meet many performance criteria, including low resistivity, sufficient adhesion to copper and high stability.[3] Ruthenium is a potential candidate material for the diffusion barrier, particularly as it is highly conductive (ρ_{Ru}= 7.1 μΩ-cm), the surface oxide is conductive (ρ_{RuO2}= 40 μΩ-cm) and can be reduced under typical electroplating conditions, and Ru is not soluble with copper up to 900°C.[4–8] The barrier films need to be ultra-thin to maximize via cross-section for the copper conductor.

Chemical vapor deposition (CVD) is a possible technology to realize highly conformal thin films.[9] Representative organometallic Ru CVD precursors include $Ru(acac)_3$ (acac, acetylacetinate),[6,10] $Ru(CO)_4(hfb)$ (hfb, hexafluoro-2-butyne),[11] $Ru(EtCp)_2$ (EtCp, ethylcyclopentadienyl),[12] and $Ru_3(CO)_{12}$.[6,13] Triruthenium dodecacarbonyl, $Ru_3(CO)_{12}$, can evaporate with sufficient vapor pressure for CVD, thermally decompose to nanocrystalline ruthenium completely with negligible carbon residue, and establish metallic thin films at temperatures as low as 423 K without any co-reacting gas.[1,13,14]

Liao, W., Ekerdt, J. G., "Ru Nucleation and Thin Film Smoothness Improvement with Ammonia during Chemical Vapor Deposition", Journal of Vacuum Science & Technology A 34, 031508 (2016)

Chemical vapor-deposited metals on oxide surfaces, such as Ru on SiO_2, typically proceeds by forming sparse three-dimensional nuclei (*i.e.*, Volmer-Weber growth mode) that ultimately merge into a continuous film because the high surface energy of the metal compared to the oxide leads to unfavorable wetting or because of the more favorable reaction sites on the metal for precursor decomposition.[15–17] Three-dimensional island growth from sparse nucleation develops a rough film surface and a higher metal mass is needed to meet the minimum thickness required to function as a diffusion barrier when compared to a smooth metal film with uniform thickness.[18] Growth chemistries indicate that metal films grown from small and dense Ru nuclei lead to thinner and smoother films with better conformal coverage than the films coalesced by large and sparse islands.[19,20]

Chemical approaches are reported that increase island nucleation density by suppressing growth on existing islands using inhibitors that can block adsorption of the metal precursor or a co-reactant on exposed metal surfaces and thereby lead to growth of ultra-thin metal films.[21,22] Alkyl iodine addition improved the metal nucleation density and film smoothness by blocking adsorption of the co-reactant O_2 gas on Ru metal when (2,4-dimethylpentadienyl)(ethylcyclopentadieynl)Ru or $Ru(EtCp)_2$ was used as the Ru precursor.[19,23–25] Carbon monoxide was selected as a Ru surface inhibitor because it adsorbs reversibly to Ru surfaces in the temperature range of precursor decomposition and Ru film growth (423-673 K).[6,26–28] Ru deposition with dramatically higher nucleation densities and, ultimately, smoother films with smaller nano-crystallinity were realized using CO addition.[22] $Ru_3(CO)_{12}$ reacts with hydroxyl and strained siloxane sites on SiO_2

and too much CO added too early in the process limits nucleation at the hydroxyl sites since CO can also compete for hydroxyl groups at too high a partial pressure.[29–32]

Herein we report the use of NH_3 to inhibit growth of nucleated Ru surfaces and enable incident precursors to generate additional nuclei. Unlike CO, ammonia is expected to be inert toward the SiO_2 surface. Ammonia synthesis and decomposition are usually catalyzed by transition metals.[33] The NH_3 is expected to adsorb and form NH_x (x=2-0) depending on the metal, temperature and partial pressure of NH_3, N_2 and H_2. Ru crystals catalyze ammonia synthesis at temperatures between 600 and 900 K, and ammonia adsorbs on and desorbs from Ru surfaces during this process.[34,35] At low temperatures (500-600 K)[36], the steady state coverage of molecular ammonia and atomic hydrogen is expected to be exceedingly low on Ru and the coverage of adsorbed atomic nitrogen, N_{ads}, is expected to be near a monolayer as the recombinative desorption rate of adsorbed nitrogen as N_2 is slow.[39] In addition, some nitrogen dissolves in Ru for films sputtered in a N_2 ambient and this leads to X-ray amorphous Ru-N films that are stable below 548 K.[37] This study investigates the extent to which the dissociative adsorption and subsequent desorption of NH_3, H_2 and N_2 can be used to manipulate the coverage of NH_x (x=2-0) and alter nucleation and film growth.

4.2 EXPERIMENTAL

Growth experiments were performed in a spherical cold-wall stainless steel CVD chamber described previously.[38–40] The 16 mm×16 mm thermal oxide SiO_2(300 nm)/Si(100) substrates were cleaned with acetone, methanol, and rinsed with deionized

water. Each substrate was placed in a load lock and moved through an ultra-high vacuum transfer chamber between a quartz tube furnace and the CVD vessel. The wafer was pre-annealed at 1173 K for 30 min at a pressure of 10^{-9}~10^{-10} Torr before it was moved to the center stage of the CVD chamber. The substrate was radiantly heated to the 448 K growth temperature. $Ru_3(CO)_{12}$ [Sigma-Aldrich, 99%] was preheated to 343 K in a saturator and admitted to the chamber 25 mm above the wafer using a showerhead heated to 373 K. Ar gas (7 standard cubic cm min^{-1}) carries the precursor through a 353 K manifold line to the showerhead and this leads to a precursor partial pressure of 47.2 mTorr in the chamber. CVD chamber pressure was monitored with a baratron gauge. The NH_3 line was controlled by a mass flow controller and entered the showerhead through separate tubing. Two growth times were used, 10 min for nucleation studies and 120 min for film growth studies.

After deposition samples cooled to about 350 K over a 20-min period under 10^{-6} Torr vacuum and were then transferred to the XPS chamber. A limited number of post-deposition samples were annealed at 448 K for 30 min under 10^{-6} Torr vacuum and then allowed to cool to about 350 K as described above.

An *in situ* X-ray photoelectron spectrometer [Physical Electronics 3057; Mg Kα and a fixed angle of 30°], connected to the CVD vessel with an ultra-high vacuum transfer line, was used to monitor carbon and nitrogen content on the film surface before/after annealing, and within the unannealed film after 60 s of Ar^+ ion sputtering. The carbon content was determined by fitting the Ru $3d_{3/2}$ and $3d_{5/2}$ XPS features at 284.3 eV and 280.1 eV, respectively, using Casa XPS 2.316 software [Casa Software Ltd].[41] We employed a Gausian-Lorentzian line shape and a Shirley baseline. The C 1*s* XPS feature at 284.5 eV

overlaps with the Ru $3d_{3/2}$ feature. The integrated peak area ratios for Ru $3d_{5/2}/3d_{3/2}$ are 1.50 and the carbon content was associated with the peak area at ~285 eV that exceeded the Ru $3d_{3/2}$ area based on this ratio.[42–44] Since the sensitivity factors for C and Ru of 0.296 and 4.273, respectively,[41] are quite different, small variations in fitting the curves can lead to an uncertainty of ± 2 % in determining the carbon content.

For *ex situ* characterization, the surface images for particle density and size distribution analysis were taken by scanning electron microscopy (SEM) [Zeiss Supra 40VP], and atomic force microscopy (AFM) [Agilent Technologies 5500] was used to measure roughness. Film thickness was measured by X-ray reflectivity (XRR) [Philips XPERT Theta-Theta Diffractometer]. Film crystallinity of films was established using X-ray diffraction (XRD) [Philips XPERT Theta-Theta Diffractometer].

4.3 RESULTS

4.3.1 Ru nanoparticle nucleation

NH_3 was admitted at partial pressures of 3 mTorr, 5.25 mTorr, 8.25 mTorr, 10.5 mTorr, 19.2 mTorr and 27.8 mTorr to compare against the growth without NH_3 addition. The precursor $Ru_3(CO)_{12}$ was carried by Ar gas and gave a partial pressure of 47.2 mTorr in all depositions. SEM images in Figure 4.1 illustrate the effect of NH_3 pressure on the particles that nucleate. The resolution limit is ~3 nm and is it difficult to resolve nuclei smaller than this size that we suspect are present in Figures 4.1(f) and 4.1(g). Figure 4.2 presents a graphical illustration of nucleation density and nuclei diameter versus NH_3 partial pressure. As the NH_3 partial pressure rises from zero to 3 mTorr and 5.25 mTorr,

the metallic Ru particle density increases from 3.1×10^{11} cm-2 without NH_3 to 5.9×10^{11} cm^{-2} and 8.1×10^{11} cm^{-2}, respectively, and the average Ru nanoparticles diameter decreases from 5.3±0.8 nm to 3.9±0.6 nm and 3.1±0.7 nm, respectively. When NH_3 partial pressures are 8.25 mTorr and 10.5 mTorr, the recognizable Ru nanoparticle densities are 7.0×10^{11} cm^{-2} and 6.8×10^{11} cm^{-2}, and the average diameters of the particles are 3.1±0.7 nm and 3.0±0.6 nm. The surface features are blurry for 19.2 mTorr and 27.8 mTorr NH_3 pressures and particles cannot be resolved using SEM; Figure 4.2 presents the particles that can be resolved and may not reflect the true trend with increasing NH_3 pressure.

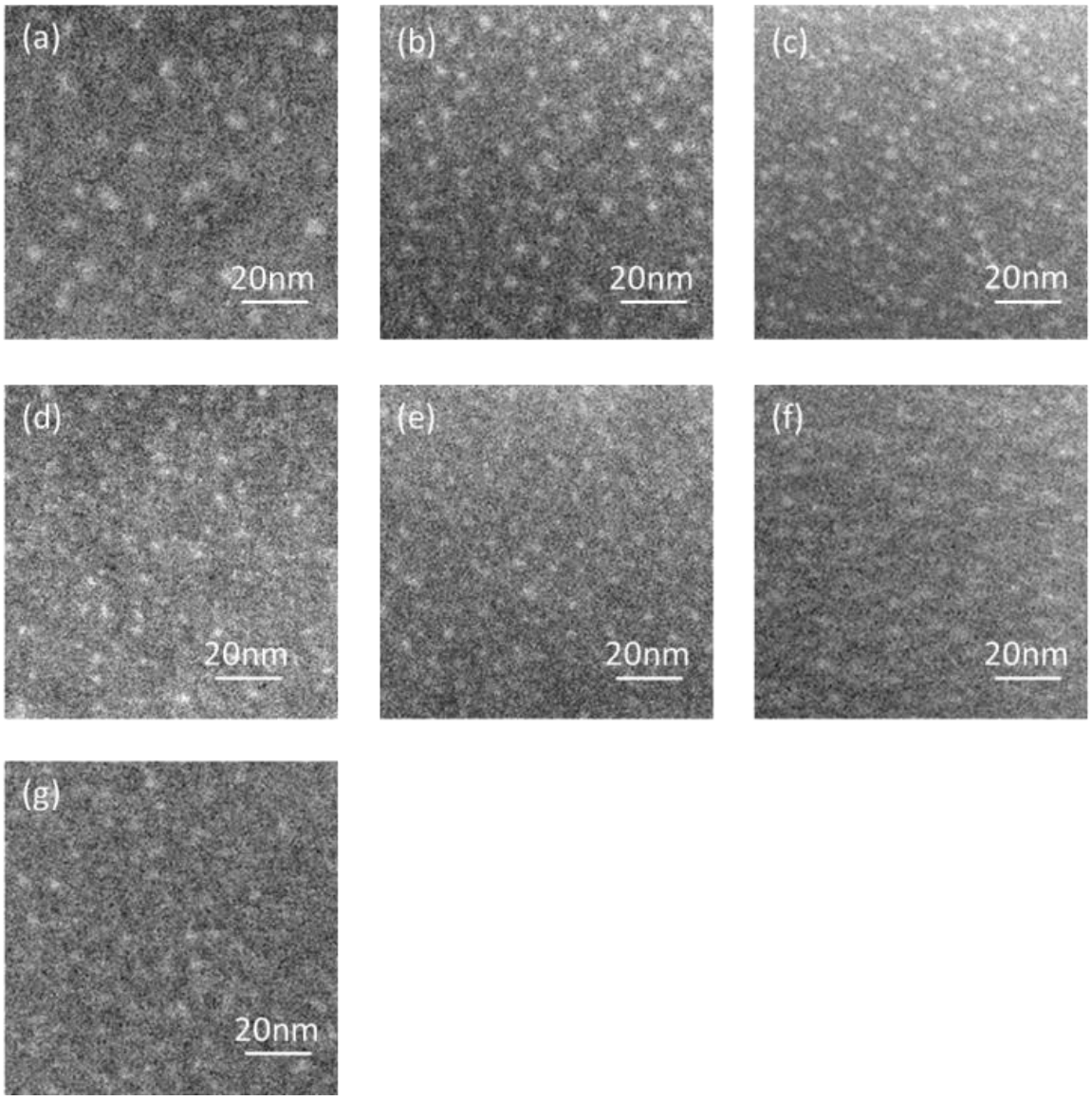

Figure 4.1: SEM images of Ru CVD at 448 K, using 47.2 mTorr $Ru_3(CO)_{12}$/Ar on silica substrates (a) without NH_3, and with (b) 3 mTorr NH_3, (c) 5.25 mTorr NH_3, (d) 8.25 mTorr NH_3, (e) 10.5 mTorr NH_3 (f) 19.2 mTorr NH_3 (g) 27.8 mTorr NH_3 for 10 min.

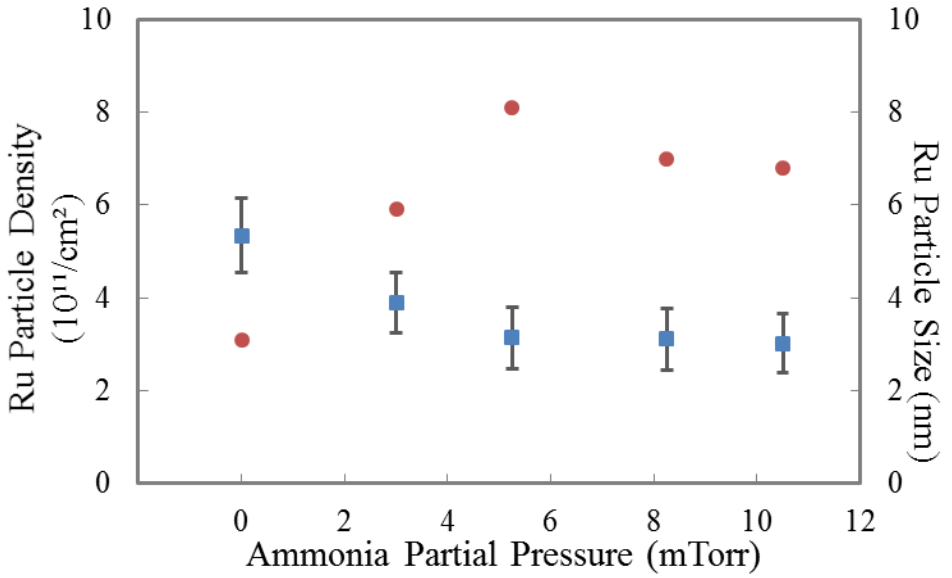

Figure 4.2: Graphical trends of Ru nanoparticle number density (•), number per cm^2, and the diameter distribution (□) corresponding to Images (a) - (e) in Fig. 4.1.

4.3.2 Ultra-thin metallic Ru film growth

Thin Ru films were realized by extending the growth time from 10 min to 120 min at the same gas flows, temperature and pressures. Possible nitrogen accumulation on film surfaces was examined by XPS after deposition at 448 K and cooling to 350 K under 10^{-6} Torr for about 20 min (Figure 4.3a, 4.3b and 4.3c). A N 1*s* XPS peak position at a binding energy 399 eV would indicate the presence of nitrogen on the film surface.[45,46] The spectrum for the film deposited without NH_3 is featureless between 396 to 402 eV, as is the spectrum for the film deposited with 5.25 mTorr NH_3, a pressure that produced the maximum particle density (Figure 4.2). There is a broad, ill-defined feature at 399 eV in the spectrum for the film deposited with 27.8 mTorr NH_3. Since NH_3 decomposition studies showed N_{ads} coverages near unity at 500 K on Ru(001),[36] some N_{ads} might be expected at the highest NH_3 pressure. After annealing the 27.8 mTorr NH_3 film at 448 K for 30 min in vacuum prior to the 20-min cooling period under 10^{-6} Torr, the N 1*s* feature attenuates (Figure 4.3d). This suggests any nitrogen-bearing adsorbates present during growth at the other NH_3 pressures likely desorbed during the sample cooling step.

Furthermore, the XPS spectra after 60-sec of Ar^+ sputtering (not shown) indicate no observable carbon or nitrogen inside annealed and unannealed Ru films either from carbonyl ligands of the Ru precursor or the incorporation N_{ads} during the deposition. As described in Experimental, there is an uncertainty of about 2% in determining the carbon concentration. Although Ru $3d_{3/2}$ overlaps C 1*s* at 284 eV binding energy, the Ru $3d_{5/2}$ peak is independent at 280 eV. The integrated peak area ratio of Ru $3d_{5/2}/3d_{3/2}$ is 3:2, fitted with

Gaussian–Lorentzian natural line shape and Shirley baseline, revealing negligible carbon contaminant (< 2%) for the films reported herein. [42–44]

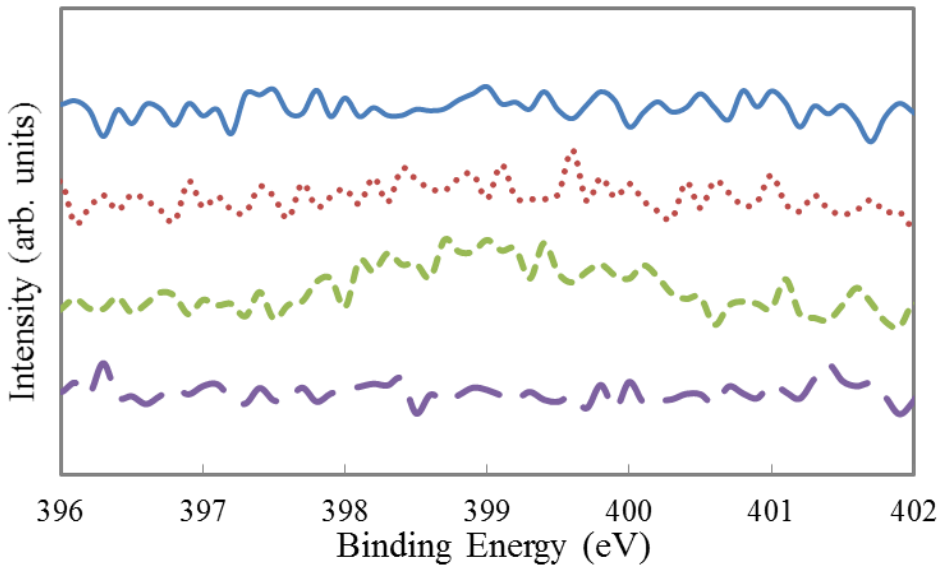

Figure 4.3: XPS of N 1*s* binding energy region for films deposited during 120 min growth runs (a) (——) without NH_3, (b) (·····) with 5.25 mTorr NH_3, (c) (-----) with 27.8 mTorr NH_3, (d) (– –) and growth with 27.8 mTorr NH_3 after annealing the film for 30 min at 448 K.

The root-mean square (RMS) roughness of the 120-min deposition films was measured by AFM and plotted in Figure 4.4. The blue diamond (♦) represents the films with constant NH_3 partial pressure during the 120-min growth. There is a minimum of 0.40 nm in the roughness versus NH_3 partial pressure at 5.25 mTorr. The substrate has an RMS roughness of 0.15 nm. The roughness without NH_3 is 0.66 nm and it decreased to 0.40 nm for 5.25 mTorr NH_3 pressure and increased to 0.53 nm for 27.8 mTorr NH_3 pressure. We suspected too much N_{ads} was present on the surfaces for pressures greater than 5.25 mTorr and this was somehow increasing the roughness.

To explore the effect of N_{ads} accumulation on film growth, the NH_3 partial pressure was reduced to 5.25 mTorr after 10 min of high NH_3 pressure nucleation. Films were nucleated for 10 min using pressures of 8.25, 10.5, 19.2 and 27.8 mTorr NH_3 and then the NH_3 pressure was reduced to 5.25 mTorr for an additional 110 min. The pressure of 5.25 mTorr NH_3 was selected because it corresponded to the density maximum in Figure 4.1 and the roughness minimum in Figure 4.4. The orange squares (■) in Figure 4.4 represent the roughness for films nucleated at the higher pressures. The films deposited with 8.25, 10.5, 19.2, and 27.8 mTorr for 10 min, then 5.25 mTorr NH_3 for 110 min have roughnesses of 0.32 nm, 0.31 nm, 0.32 nm and 0.31 nm, respectively. Growth at constant NH_3 pressures of 8.25, 10.5, 19.2, and 27.8 mTorr for 120 min led to roughness of 0.41 nm, 0.45 nm, 0.50 nm, and 0.53 nm, respectively. The AFM surface topography and three dimensional scan of films grown without NH_3 for 120 min and with 27.8 mTorr NH_3 for 10 min then 5.25 mTorr NH_3 for 110 min are displayed in Figure 4.5. The surface features for the film deposited with NH_3 are much smaller than the film deposited without NH_3.

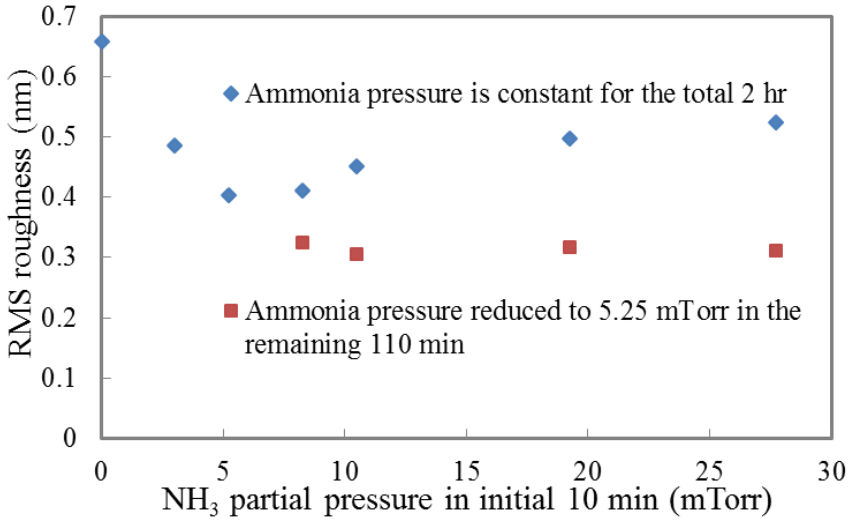

Figure 4.4: Graphical trends of Ru thin film roughness vs. NH_3 partial pressure for 120 min Ru deposition at 448 K and 47.2 mTorr $Ru_3(CO)_{12}$/Ar without NH_3, (♦) with constant NH_3 for 120 min and (■) with high NH_3 during initial 10 min then at 5.25 mTorr NH_3 for additional 110 min.

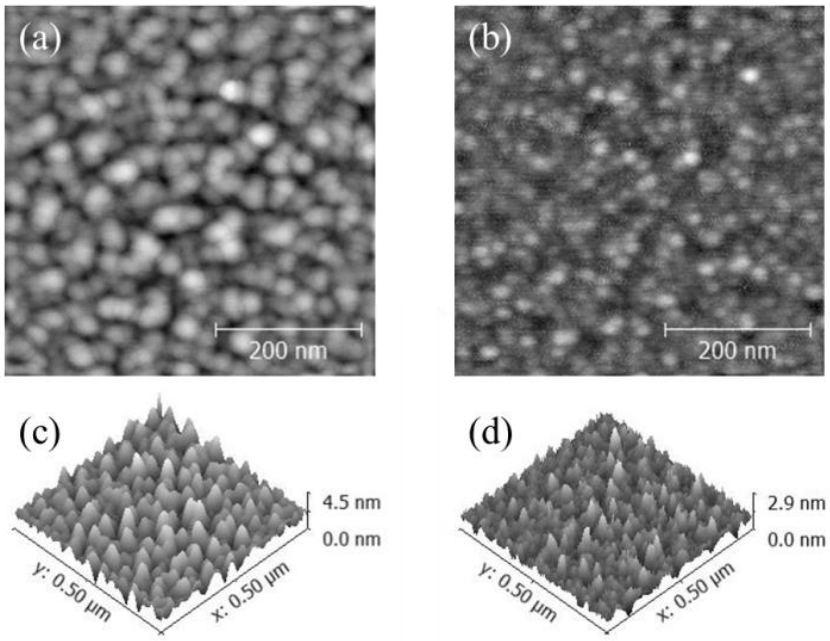

Figure 4.5: AFM images of Ru CVD at 448 K, using 47.2 mTorr $Ru_3(CO)_{12}$/Ar on silica substrates (a) (c) without NH_3 for 120 min, and with (b) (d) 27.8 mTorr NH_3 for 10 min then 5.25 mTorr NH_3 for additional 110 min. (a) (b): topography images; (c) (d): three dimensional view.

XRR spectra are used to estimate the film thicknesses (Figure 4.6). The films grown only with $Ru_3(CO)_{12}$ have a thickness of 5.2 nm. Representative films near the minimum in RMS roughness (Figure 4.5) at 5.25 mTorr NH_3 and at the highest added NH_3 pressure of 27.8 mTorr have the thicknesses of 5.8 nm and 5.7 nm, respectively. All the other Ru films grown with NH_3 addition have the thickness in the range of 5.4 - 5.8 nm.

In addition, film crystallinity is imaged by XRD (Figure 4.7). The film grown without NH_3 has a small bump at 2θ of 38.38° and two peaks at 2θ of 42.18° and 44.02° corresponding to Ru(100), Ru(002) and Ru(101), respectively (Figure 4.7a). The film grown with 5.25 mTorr NH_3 for 120 min has a weak feature at 2θ of 38° and a broad weak bump covering the region where Ru(002) and Ru(101) diffraction features are expected (Figure 4.7b). The film grown with 27.8 mTorr NH_3 for 120 min appears X-ray amorphous (Figure 4.7d).

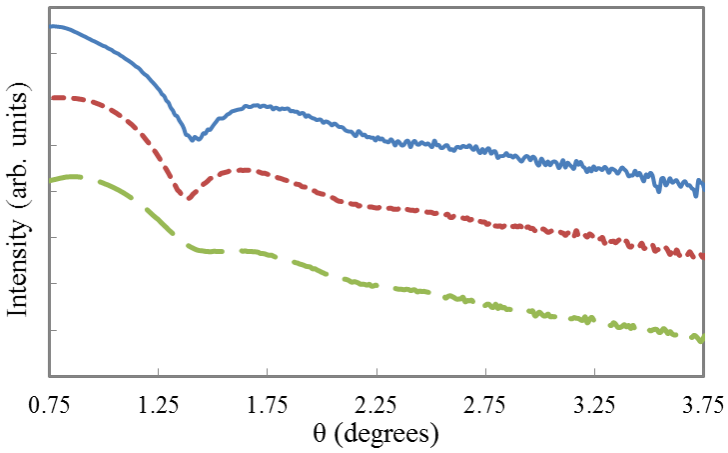

Figure 4.6: XRR spectrum following 120 min Ru deposition at 448 K and 47.2 mTorr $Ru_3(CO)_{12}$/Ar (a) (——) without NH_3, (b) (-----) with 5.25 mTorr NH_3, and (c) (– –) with 27.8 mTorr NH_3, corresponding to film thicknesses of 5.2, 5.8 and 5.7 nm, respectively.

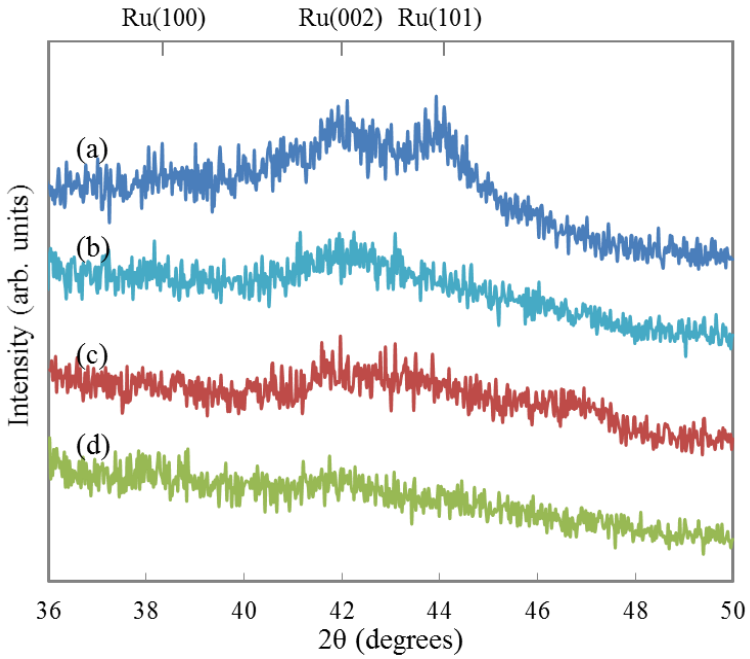

Figure 4.7: XRD spectrum following 120 min Ru deposition at 448 K and 47.2 mTorr $Ru_3(CO)_{12}$/Ar (a) without NH_3 for 120 min, (b) with 5.25 mTorr NH_3 for 120 min, (c) with 27.8 mTorr NH_3 for 10 min then 5.25 mTorr NH_3 for 110 min, and (d) with 27.8 mTorr NH_3 for 120 min.

4.4 DISCUSSION

Ru crystals catalyze ammonia synthesis at temperatures between 600 and 900 K, and ammonia decomposition from 400 to 1250 K.[34–36] Ammonia adsorbs reversibly on Ru surfaces as N_{ads} and H_{ads}.[3,35,47] The experiments presented herein were performed at 448 K – near the lower temperature range for ammonia decomposition and still low enough to retard the rapid desorption of N_{ads}. The expectation was for the dissociative adsorption of ammonia to be rapid enough, that N_{ads} would block Ru surface sites, and that N_{ads} would desorb as N_2 versus incorporate into the films. Building on previous work showing the inhibiting and reversible role of CO during Ru nucleation when added at sufficiently high partial pressures,[22] we sought to determine if N_{ads} (and possible NH_x) could obstruct/inhibit $Ru_3(CO)_{12}$ precursor adsorption on Ru particles and drive the formation of additional Ru nuclei on the SiO_2 surface, which is a lower probability event once nucleation has occurred.

The coverage of N_{ads} on a Ru surface increases at the higher NH_3 partial pressures and is dependent on the temperature. The rate of ammonia synthesis on a Ru catalyst was found to decrease as the partial pressure of ammonia in the reactor increased illustrating that produced ammonia that dissociatively adsorbs can block active sites on Ru.[35] Most relevant for the studies reported herein is how the fractional coverage of N_{ads} increases to near unity as the temperature decreased below 600 K when ammonia adsorbed on Ru(001).[36] The NH_3 adsorption rate coefficient was found to be proportional to the flux of NH_3[36] and the onset for recombinative N_{ads} desorption as N_2 in temperature programmed desorption is observed around 550-650 K.[35,36] Therefore, the adsorbed nitrogen adatom coverage on Ru is correlated to the NH_3 partial pressure at temperatures close to 448 K.

The schematic representation for nucleation is presented in Figure 4.8. The nucleation studies (Figures 4.1 and 4.2) show a maximum in the nanoparticle density at an NH_3 gas pressure of 5.25 mTorr. The particle size asymptotically approaches the minimum resolvable size of ~3 nm with increasing NH_3 pressure. The density maximum is likely associated with the resolvability of the small Ru particles using the SEM and the film growth experiments (see below) support an interpretation that nucleation is affected monotonically with increasing NH_3 pressure. With increasing pressure, the steady state coverage of N_{ads} increases and this N_{ads} inhibits growth of Ru islands by some combination of directly blocking $Ru_3(CO)_{12}$ adsorption on a nucleated island or by incorporation of Ru adatoms that have formed on the SiO_2 substrate. The net result is Ru adatoms that form on the SiO_2 surface increase in concentration and nucleate new Ru islands. Smaller particles and higher densities of nucleated islands are expected at the higher NH_3 pressures.

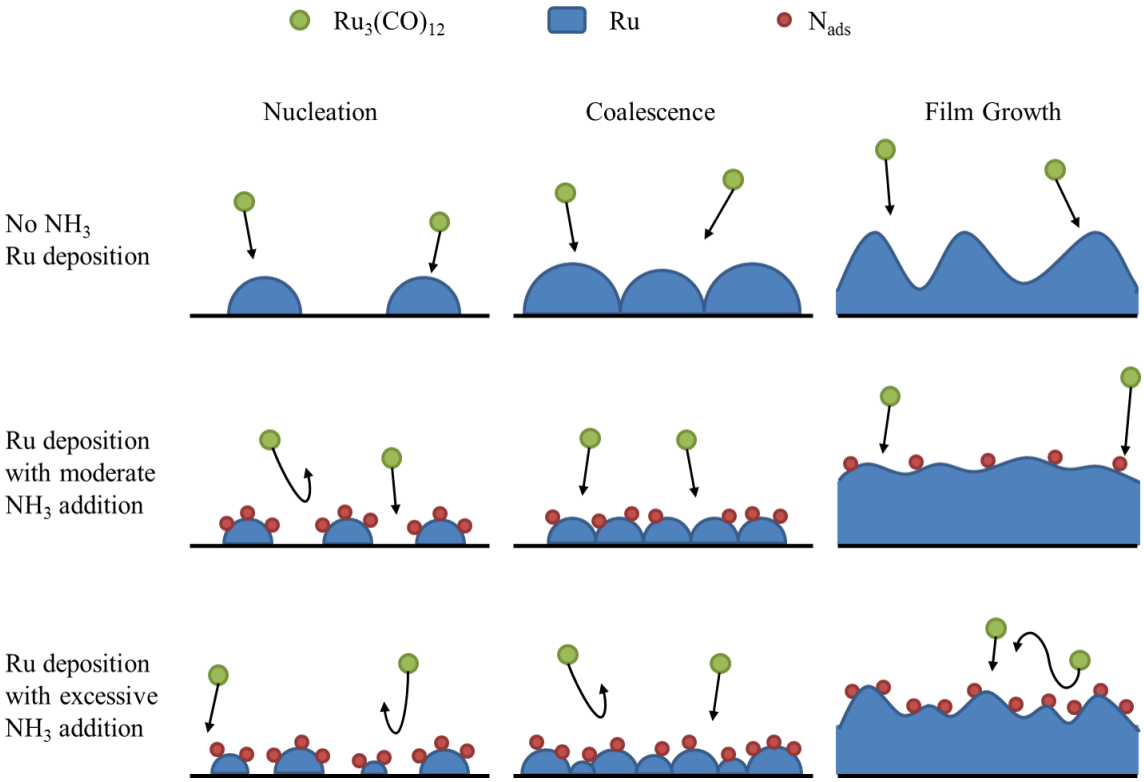

Figure 4.8: Schematic diagram of NH_3 addition to Ru CVD compared to deposition without NH_3.

Using film roughness as a surrogate indicator for nucleation density (Figure 4.4) supports the interpretation of the effect of NH_3 pressure on nucleation. The experiments that were conducted with increasing NH_3 pressure during the first 10 min, followed by a constant NH_3 pressure of 5.25 mTorr for 110 min reveal that the roughness approaches a constant value of ~0.31 nm monotonically – a value that is lower than 0.40 nm found for nucleation at 5.25 mTorr NH_3 and growth for 110 additional min at 5.25 mTorr NH_3. We suggest the roughness is related to the density of islands and their average size as they coalesce into a continuous film. Films nucleated above 5.25 mTorr NH_3 should have smaller nuclei and a greater number of nuclei as the pressure increases up until the NH_3 pressure that produces N_{ads} of unity or a constant value near unity. After the nucleation step at the various NH_3 pressures, the constant 5.25 mTorr NH_3 pressure should block Ru surfaces to the same extent for the remainder of the growth time.

The trend of roughness with NH_3 pressure for constant NH_3 pressures over the full 120 min growth time (Figure 4.4, diamond shapes) can be understood from the perspective of the distribution of nuclei sizes as they coalesce into a continuous film and continue to grow as a film. At low nucleation densities (0 and 3 mTorr NH_3) the islands are sparse (relative to higher NH_3 pressures) and grow to a large size before coalescing into the continuous film that continues to grow. At the higher NH_3 pressures (19.2 and 27.8 mTorr) the N_{ads} coverage is high enough that nucleation is suppressed and additional nucleation events occur during the entire time required to reach a coalesced film. If this time-to-coalesce is much greater than 10 min, large nuclei that formed early in the process and the very smallest that formed late in the process coalesce together. Greater disparity in

nucleation sizes, not just the average size, will lead to increase roughness in the final film. Figure 4.8 illustrates this effect.

Unexpectedly the growth rates increased slightly in the presence of NH_3 (Figure 4.6). Assuming Ru metal is more favorable for $Ru_3(CO)_{12}$ decomposition compared to SiO_2, the growth rate could be increased by the enhanced Ru surface area associated with smaller and denser nuclei. Alternately, a $RuNH_x$ (x = 0-2) intermediate could form on the surface and accelerate growth. Further studies are required to understand the origins of the growth rate enhancement.

Ru sputtered in a nitrogen atmosphere leads to dissolved N and produces amorphous Ru-N films, and the N effuses from the Ru film after it is annealed above 548 K.[37] For the results presented herein N_{ads} on the Ru surface during CVD at 448 K can desorb as N_2 and/or dissolve into the film. XPS analysis indicates the N may be adsorbed on the film or present in the near surface region for the highest NH_3 pressure (Figure 4.3); annealing these films for 30 min at 448 K led to a N level below the detection limit of 1%. With increasing NH_3 pressure, the films appear to be increasingly X-ray amorphous (Figure 4.7). It is possible the N_{ads} may have incorporated to some level into the Ru nanoparticles and/or film and facilitated an amorphous structure to form and more studies are needed to understand the origin of the X-ray amorphous character of the films.

4.5 CONCLUSION

At low ammonia partial pressure, the blocking gas results in uniform smaller nanoparticles with a higher nucleation density that leads to smoother Ru films compared

to Ru films deposited without ammonia. At the highest ammonia partial pressure, the ammonia keeps forcing additional nucleation and may lead to disparate sizes, but at a higher density, before the Ru particles coalesce to a continuous film. The large and small co-existing particles produce a rougher film compared to the film deposited with low ammonia partial pressure. Nitrogen residue on the film surface can be eliminated by post-growth annealing at 448 K, and there is no carbon or nitrogen contamination inside the Ru films. The smoothest thin film is achieved by high ammonia partial pressure during a 10-min nucleation step followed by a low ammonia pressure (5.25 mTorr) during the rest of film growth. The ammonia addition reduces the film nanocrystallinity and the films appear X-ray amorphous with highest ammonia partial pressure (27.8 mTorr) during film deposition.

4.6 REFERENCES

1. A. E. Kaloyeros, and E. Eisenbraun, Annu. Rev. Mater. Sci. **30**, 363–385 (2000).
2. International Technology Roadmap for Semiconductors (2013) - Interconnect Summary.
3. P. J. Estrup and J. Anderson, J. Chem. Phys. **49**, 523–528 (1968).
4. Y. Murakami, J. Li, D. Hirose, S. Kohara and T. Shimoda, J. Mater. Chem. **C 3**, 4490–4499 (2015).
5. I. Goswami and R. Laxman, Semicond. Int. **27**, 49–54 (2004).
6. M. L. Green, M. E. Gross, L. E. Papa, K. J. Schnoes and D. Brasen, J. Electrochem. Soc. **132**, 2677–2685 (1984).
7. H. Kim, Surf. Coatings Technol. **200**, 3104–3111 (2006).

8. R. Chan, T. N. Arunagiri, Y. Zhang, O. Chyan, R. M. Wallace, M. J. Kim and T. Q. Hurd, Electrochem. Solid-State Lett. **7**, G154–G157 (2004).

9. J. E. Crowell, J. Vac. Sci. Technol. A Vacuum, Surfaces, Film. **21**, S88–S94 (2003).

10. J. C. Vigui and J. Spitz, J. Electrochem. Soc. **122**, 585–588 (1975).

11. Y. Senzaki, W. L. Gladfelter and F. B. McCormick, Chem. Mater. **5**, 1715–1721 (1993).

12. Y. Matsui, M. Hiratani, T. Nabatame, Y. Shimamoto and S. Kimura, Electrochem. Solid-State Lett. **4**, C9–C12 (2001).

13. Q. Wang, J. G. Ekerdt, D. Gay, Y. M. Sun and J. M. White, Appl. Phys. Lett. **84**, 1380–1382 (2004).

14. E. P. Boyd, D. R. Ketchum, H. Deng and S. G. Shore, Chem. Mater. **9**, 1154–1158 (1997).

15. C. Ratsch and J. A. Venables, J. Vac. Sci. Technol. A Vacuum, Surfaces, Film. **21**, S96–S109 (2003).

16. T. A. Witten and L. M. Sander, Phys. Rev. Lett. **47**, 1400–1403 (1981).

17. H. Brune, Surf. Sci. Rep. **31**, 121–229 (1998).

18. S. Park, H. Kim, K. Kim and S. Min, Electrochem. Solid-State Lett. **1**, 262–264 (1998).

19. K. M. Thom and J. G. Ekerdt, Thin Solid Films **518**, 36–42 (2009).

20. N. Kumar, A. Yanguas-Gil, S. R. Daly, G. S. Girolami and J. R. Abelson, J. Am. Chem. Soc. **130**, 17660–17661 (2008).

21. S. Babar, N. Kumar, P. Zhang, J. R. Abelson, A. C. Dunbar, S. R. Daly and G. S. Girolami, Chem. Mater. **25**, 662–667 (2013).

22. W. Liao and J. G. Ekerdt, Chem. Mater. **25**, 1793–1799 (2013).

23. E. S. Hwang and J. Lee, Electrochem. Solid-State Lett. **3**, 138–140 (2000).

24. J. J. Kim, D. H. Jung, M. S. Kim, S. H. Kim and D. Y. Yoon, Thin Solid Films **409**, 28–32 (2002).

25. J. J. Kim, M. S. Kim and D. Y. Yoon, Chem. Vap. Depos. **9**, 105–109 (2003).

26. A. A. Davydov and A. T. Bell, J. Catal. **49**, 332–344 (1977).

27. H. Pfnür and D. Menzel, J. Chem. Phys. **79**, 2400–2410 (1983).

28. G. E. Thomas and W. H. Weinberg, J. Chem. Phys. **70**, 1437–1439 (1979).

29. A. Theolier, A. Choplin, L. D'Ornelas, J.M. Basset, G. Zanderighi and C. Sourisseau, Polyhedron **2**, 119–121 (1983).

30. G. M. Zanderighi, C. Dossi, R. Ugo, R. Psaro, A. Theolier, A. Choplin, L.D'Ornelas and J.M. Basset, J. Organomet. Chem. **296**, 127–146 (1985).

31. T. P. Beebe, P. Gelin and J. T. Yates Jr., Surf. Sci. **148**, 526–550 (1984).

32. G. Ghlotti, E. Garrone, C. Morterra and F. Boccuzzi, J. Phys. Chem. **83**, 2863–2869 (1979).

33. A. Boisen, S. Dahl, J. K. Norskov and C. H. Christensen, J. Catal. **230**, 309–312 (2005).

34. S. Sanyan, M. Kantcheva, S. Suzer and D. O. Uner, J. Mol. Struct. **480-481**, 241–245 (1999).

35. S. Dahl, P. A. Taylor, E. Törnqvist and I. Chorkendorff, J. Catal. **178**, 679–686 (1998).

36. W. Tsai and W. H. Weinberg, J. Phys. Chem. **91**, 5302–5307 (1987).

37. M. Damayanti, T. Sritharan, S. G. Mhaisalkar and Z. H. Gan, Appl. Phys. Lett. **88**, 044101–1–3 (2006).

38. J. Shin, A. Waheed, W. A. Winkenwerder, H. Kim, K. Agapiou, R. A. Jones, G. S. Hwang and J. G. Ekerdt, Thin Solid Films **515**, 5298–5307 (2007).

39. J. Shin, H. W. Kim, G. S. Hwang and J. G. Ekerdt, Surf. Coatings Technol. **201**, 9256–9259 (2007).

40. L. B. Henderson and J. G. Ekerdt, J. Electrochem. Soc. **157**, D29–D34 (2010).

41. J. F. Moulder, W. F. Stickle, P. E. Sobol and K. D. Bomben, *Handbook of X-ray Photoelectron Spectroscopy,* Perken-Elmer Corporation: Eden Prairie, MN 1992.

42. H. Kim, I. Rabelo de Moraes, G. Tremiliosi-Filho, R. Haasch and A. Wieckowski, Surf. Sci., **474**, L203–212 (2001).

43. Y. Lai, Y. Chen, Y. Chi, C. Liu, A. J. Carty, S. Peng and G. Lee, J. Mater. Chem., **13**, 1999–2006 (2003).

44. D. E. Bost and J. G. Ekerdt, Thin Solid Films, **558**, 160–164 (2014).

45. D. N. Hendrickson, J. M. Hollander and W. L. Jolly, Inorg. Chem. **8**, 2642–2647 (1969).

46. J. B. Wu, J. Wu, Y. Lin, J. Wang, P. Chang, C. Tasi, C. Lu, H. Chiu and Y. Yang, Inorg. Chem. **42**, 4516–4518 (2003).

47. M. Wilf and M. Folman, J. Chem. Soc. **72**, 1165–1176 (1975).

Chapter 5: Precursor Dependent Nucleation and Growth of Ruthenium Films during Chemical Vapor Deposition

5.1 INTRODUCTION

In the semiconductor industry, ultra-thin and smooth films (< 3 nm) are being sought as the copper diffusion barrier to prevent copper migration into the surrounding dielectric layers of the integrated circuit (IC).[1,2] To implement an effective diffusion barrier without effecting the IC performance, the thin liner films are required to have great thermal and chemical stability, high conductivity and sufficient adhesion for further copper deposition in IC manufacturing steps.[3] Ruthenium is a promising material for the diffusion barrier with its negligible solubility with copper up to 1173 K and it has a low bulk resistivity of ρ_{Ru}= 7.1 μΩ-cm.[4–7]

Chemical vapor deposition (CVD) is a widely-used technology to deposit thin metal films with uniform thickness and high conformality.[8] Representative organometallic Ru CVD precursors include $Ru(acac)_3$ (acac, acetylacetinate),[7,9] $Ru(EtCp)_2$ (EtCp, ethylcyclopentadienyl),[10] $Ru_3(CO)_{12}$[7,11] and (bis(*N,N'*-di-*tert*-butylacetamidinato) ruthenium(II) dicarbonyl).[12,13] We have reported on the nucleation and growth of Ru on SiO_2 using $Ru_3(CO)_{12}$ and how adding CO and NH_3 during CVD can improve nucleation and lead to smoother ultra-thin films.[14,15] Bis(*N,N'*-di-*tert*-butylacetamidinato) ruthenium(II) dicarbonyl (Ru(AMD)) incorporates an amidinate ligand to provide thermal stability during delivery, sufficient volatility for vapor-phase growth, and sufficient reactivity to enable CVD growth,[12,13] and is employed herein.

Liao, W., Ekerdt, J. G., "Precursor Dependent Nucleation and Growth of Ruthenium Films during Chemical Vapor Deposition" (submitted)

Metal film growth is generally categorized using four growth modes, Frank-van der Merwe or two dimensional (2D) layer-by-layer growth, Volmer-Weber (VW) or three dimensional (3D) growth, Stranski–Krastanov (SK) in which 3D growth occurs above the a 2D wetting layer, and pseudo layer-by-layer 2D island growth (2DI) in which the 2D islands do not form a complete layer before the onset of 3D growth, depending on relative binding energies of metal adatoms on the nucleated islands and on the substrate.[16–19] Mid-to-late transition metals generally follow a VW growth mode; however at sufficiently low temperatures and on well-ordered oxides surfaces they can grow as 2D layer islands and then as 3D particles above a critical island (*i.e.*, 2D monolayer) coverage ranging from 15 to 85%.[17] In Volmer-Weber growth metal nuclei grow both horizontally and vertically and then coalesce into a continuous film.[16,20] Big and sparse islands necessarily grow into thick films to become continuous at the minimum diffusion barrier thickness and the rough surface contains surplus unnecessary mass. On the contrary, films grown from small and dense nuclei lead to thinner and smoother films with a more uniform thickness.

The nucleation of Ru on SiO_2 during CVD using $Ru_3(CO)_{12}$ follows VW growth because of unfavorable wetting associated with the high surface energy of the Ru and the sparse nature of the nuclei from which the 3D islands grow.[16,18,21] We have employed CO and NH_3 to adsorb or react reversibly on the nucleated Ru islands and slow the incorporation of additional Ru into the islands enough that sufficient Ru adatoms form on the SiO_2 and generate additional nuclei.[14,15] An alternative approach to increasing nucleation density during CVD involves the use of more reactive precursors and/or increasing the reactivity of the oxide surface toward the precursor to produce a higher initial

concentration of Ru adatoms since nucleation is related to ad-atom concentration.[16,18,22] The $Ru_3(CO)_{12}$ precursor is reasoned to react with SiO_2 free isolated hydroxyl ($(Si\text{-}OH)_i$) groups forming unstable $HRu_3(CO)_{10}(OSi\leqslant)$ grafted clusters that thermally decompose to metallic ruthenium or continue to react with SiOH groups.[23,24] Zhuravlev reported the distribution of the different surface silanol and siloxane groups including $(Si\text{-}OH)_i$ groups as a function of annealing temperature.[25] We report herein $Ru_3(CO)_{12}$ reactivity, and in turn nucleation density, correlates with the $(Si\text{-}OH)_i$ concentration predicted by the Zhuravlev model.

Amidinate ligand-based precursors are expected to interact differently with SiO_2 than $Ru_3(CO)_{12}$ and the ultimate fate of the amidinate ligands depends on the presence of a reducing gas, such as H_2, during the chemical deposition process.[12,26–28] After partial ligand loss and reaction at hydroxyl sites, Ru may bind to the SiO_2 through SiO-Ru bonds. The amidinate ligands may form a ligand dimer if the precursor undergoes thermal decomposition on the surface.[12] During reaction of Ru(AMD) with hydroxyl groups it may also be possible an amidine forms and this can readsorb and bind to the SiO_2 surface.[27] We report herein Ru(AMD) appears to form a wetting layer and not follow VW growth.

When film growth follows a Stranski-Krastanov or 2DI growth mode, smoother films may not be realized by increasing adatom formation on the oxide substrate. In addition to increasing nucleation density, gas chemisorption can induce metal surface reconstruction.[29–32] Hydrogen, nitrogen and CO are reported to modify platinum particle shape significantly through the variation of the surface free energy on different crystal facets.[33–36] The mechanisms of the atom/molecular induced reconstruction include the

redistribution of surface electronic density,[32] the reduced activation energy of surface atom mobility,[30,31] and the higher adsorption heat on reconstructed surface[30,32] by the solid-gas interactions. A more open, rough surface with fewer neighboring atoms is more flexible than a rigid bulk structure surface.[30,31] The formation and break-up of the substrate-adsorbate bond can drive the surface atom rearrangement to optimize surface chemical bonding.[31] This surface relaxation smooths out the film roughness gradually.[31] CO has been reasoned to produce topographical changes in Rh through the possible intermediate formation of Rh-subcarbonyls[37] and has also been reported to increase the critical island coverage in 2DI due to the higher adsorption energy of CO on the metal than on the oxide.[17]

5.2 EXPERIMENTAL

Growth experiments were performed in a spherical cold-wall stainless steel CVD chamber, connected via a high-vacuum transfer line to an x-ray photoelectron spectrometer [Physical Electronics 3057; Mg Kα] and has been described previously.[38–40] The 16×16mm thermal oxide SiO_2(300nm)/Si(100) substrates were cleaned with acetone, methanol, and rinsed with deionized water. Each substrate was placed in a load lock and moved into an ultra-high vacuum quartz tube and radiantly annealed at temperatures from 473 to 1193 K for 1 hr before growth. Then the substrate was moved through the same ultra-high vacuum transfer chamber onto the center stage of the CVD vessel. CVD chamber pressure was monitored with a baratron gauge. The substrate was radiantly heated to the growth temperature in the CVD chamber.

The growth times were 10 min for nucleation studies using $Ru_3(CO)_{12}$ at 403 K. $Ru_3(CO)_{12}$ [Sigma-Aldrich, 99%] was delivered as a vapor in a carrier gas stream of Ar and the precursor pressure in the growth chamber was 12 mTorr.[14] Various temperatures and times were used for growth with Ru(AMD). Ru(AMD) [Dow AccuDEP™ Ruthenium Precursor] was preheated to 383 K for 30 min in a sealed saturator and showered 25 mm above the wafer, it was carried by 10 standard cm^3 min^{-1} Ar gas flowing through a 423 K manifold line and oil bath entrance, which led to a precursor partial pressure of 45 mtorr in the chamber. Each substrate for the Ru(AMD) studies was radiantly annealed at 1173 K for 30 min in the ultra-high vacuum quartz tube before growth. The CO line was controlled by a mass flow controller and flowed into the system through the chamber sidewall at a partial pressure of 4 mTorr. The NH_3 line was controlled by a mass flow controller and flowed into the system on the top of the chamber through the same oil bath as the precursor in separate tubing at a partial pressure of 5 mTorr.

In situ x-ray photoelectron spectroscopy (XPS) was used to survey the emission peaks for the elemental composition of the surface. Film thickness is calculated from the signal attenuation of a substrate feature.[41,42] For a thin Ru film (< 4 nm), the XPS Si 2*p* signal attenuation from the SiO_2 substrate can be used to calculate the Ru thickness by referring to the NIST Effective-Attenuation-Length Database.[43] This XPS measurement assumes the films are ideally flat. An equivalent thickness is estimated by this XPS attenuation calculation when the film is discontinuous[44] and, in general, the attenuation method underestimates the film thickness for discontinuous films.[45] For thick films, the XPS is used to monitor carbon and nitrogen content on the film surface before/after

annealing, and inside the film after 60 s of Ar^+ ion sputtering.[15] For *ex situ* characterization, the surface images for particle density and size distribution analysis were taken by scanning electron microscopy (SEM) [Zeiss Supra 40VP], and atomic force microscopy (AFM) [Aligent Technologies 5500] was used to measure roughness. Thick film thickness (> 4 nm) was measured by x-ray reflectivity (XRR) [Philips XPERT Theta-Theta Diffractometer]. Film crystallinity of films was established using x-ray diffraction (XRD) [Philips XPERT Theta-Theta Diffractometer]. The crystallite grain size are calculated from XRD peaks using Scherrer equation.[46]

5.3 RESULTS

5.3.1 Ru nanoparticle nucleation using $Ru_3(CO)_{12}$ on pretreated SiO_2

$Ru_3(CO)_{12}$ thermally decomposes directly to give Ru above 423 K on a silica substrate,[11,23,24] and appears to react on $(Si\text{-}OH)_i$ groups.[14] The studies reported herein were conducted at 403 K to slow the precursor decomposition rate and avoid film growth during the 10-min experimental observation time. The SiO_2 substrates were annealed at 10^{-8} to 10^{-9} Torr for 60 min prior to transferring them *in situ* to the growth chamber. The samples were inserted into the preheated annealing furnace and removed from the furnace hot. After positioning in the growth chamber, the samples were heated to the growth temperature over about 20 min.

Figure 1 presents representative SEM images of samples that had been annealed in the furnace at 473, 673, 873, 1073 and 1193 K. The Ru nucleation density increases from

5.3×10^{11} to 8.0×10^{11} cm^{-2} as the SiO_2 substrate pre-annealing temperature rises from 473 to 673 K, and then the Ru nucleation density decreases to 6.1×10^{11}, 4.8×10^{11} and 2.9×10^{11} cm^{-2} when the substrate is pre-annealed at 873, 1073 and 1193 K, respectively. The Zhuravlev model describes SiO_2 surface hydroxylation.[25] Figure 2 presents the Ru particle density vs. pretreatment temperature and plots the $(Si\text{-}OH)_i$ density versus temperature from the Zhuravlev model. The experimental nucleation data and the predicted $(Si\text{-}OH)_i$ density show similar trends and differ in absolute values. In the Zhuravlev model, the isolated Si-OH density is 1.2×10^{14}, 2.0×10^{14}, 1.3×10^{14}, 0.6×10^{14} and 0.4×10^{14} cm^{-2} when the silica substrate is pretreated at 473, 673, 873, 1073 and 1173 K, respectively.[25]

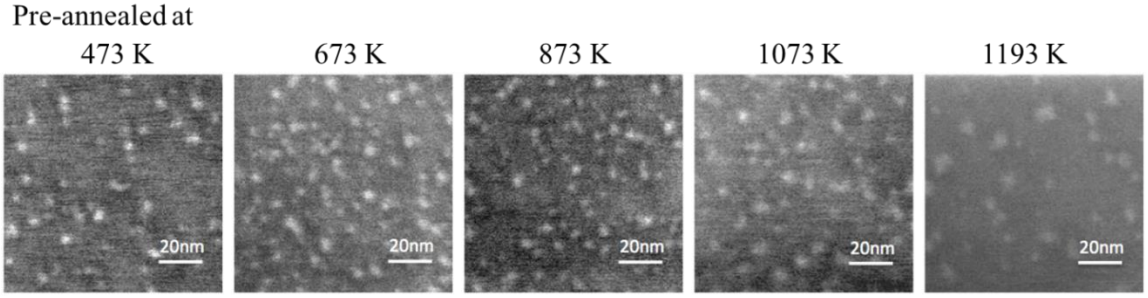

Figure 5.1: The SEM images of nucleation density vs. substrate pretreated temperatures from 473 to 1193 K at each point following CVD with $Ru_3(CO)_{12}$ at 403 K for 10 min.

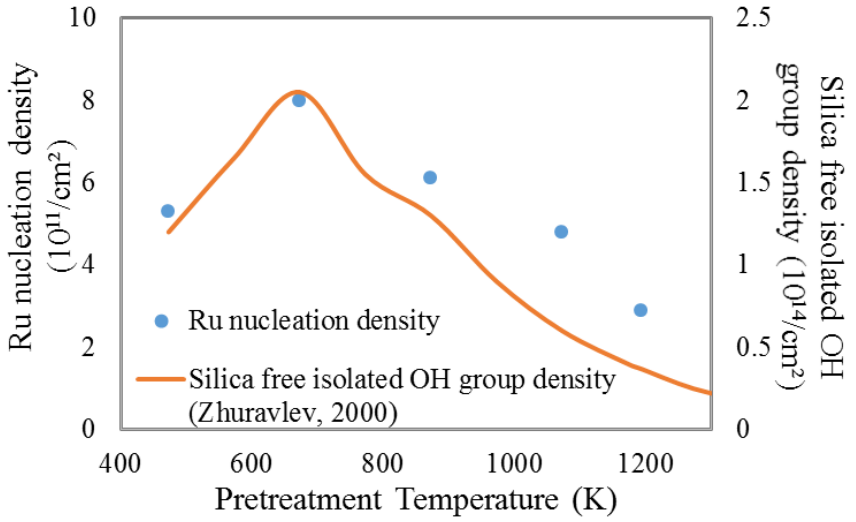

Figure 5.2: Blue ○, the diagram of nucleation density vs. substrate pretreated temperatures from 473 to 1193 K at each point following CVD with $Ru_3(CO)_{12}$ at 403 K for 10 min. Orange curve is the Zhuravlev model-2 of average concentration of the free isolated OH groups.[26]

5.3.2 Comparison between $Ru_3(CO)_{12}$ and $Ru(^tBu\text{-}Me\text{-}amd)_2(CO)_2$ Precursors during Nucleation

The nucleation with $Ru_3(CO)_{12}$ can be categorized as typical of Volmer-Weber 3D growth. The initial growth of Ru with Ru(AMD) is quite different. Unlike the correlation of nucleation density with pretreatment temperature for $Ru_3(CO)_{12}$ (Figure 2) similar experiments at temperatures ranging from 403 to 453 K revealed very sparse to no particles for Ru(AMD) (not shown). Growth with Ru(AMD) at 473 K led to films with thicknesses of 0.33, 0.35 and 0.36 nm after 7, 10 and 12 min, respectively. Assuming a constant growth rate and fitting the data at 473 K to a linear growth model suggests a thin, 0.3-nm Ru wetting layer forms on the SiO_2 quickly and that once formed, a much slower growth rate of ~0.06 nm/min follows. Basing absolute thickness on attenuation of a substrate XPS feature, such as Si 2*p*, can be problematic and the true thickness tends to be underestimated

when discontinuous and/or rough films are sampled;[45] therefore the wetting layer and all the ultra-thin film thickness reported at 473 K may be greater.

Ru(AMD) has been used in the atomic layer deposition (ALD) of thick (90-180 nm) Ru films.[12] We converted the ALD thicknesses reported by Li et al. into a growth rate by assuming Ru growth only occurs during the precursor exposure cycle and plot the effective growth rates in Fig. 3. Films were grown in this study in a CVD process with Ru(AMD) at 473, 498, 523 and 573 K for 7 min to study the effect of the substrate temperature on the ultra-thin film growth. Film thickness was determined by XPS and a 0.3-nm wetting layer was subtracted from each thickness at each temperature. The blue ◊ data in Fig. 3 represent Ru growth rates on Ru of 0.004, 0.011, 0.024 and 0.144 nm min^{-1} at 473, 498, 523 and 573 K, respectively, after allowing for the wetting layer. The effective ALD growth rate and the Ru growth rates on a wetting layer lead to activation energies of 81 kJ/mol and 79 kJ/mol, respectively. Interestingly the copper (I) *N,N'*-di-sec-butylacetamidinate precursor has been reported to have a much slower deposition rate on metal surfaces (0.11 Å/cycle on Ru and 0.5 Å/cycle on Cu) than on an oxide surface (1.9 Å/cycle on Al_2O_3/SiO_2).[26] This is consistent with our interpretation of a rapidly-formed wetting layer followed by slower growth of Ru on the wetting layer. The growth rates represented in Fig. 3 are proportionally slower at each temperature than Li et al.[12] and this could be associated with the lower precursor partial pressure and lower precursor sublimation temperature during CVD experiments than in ALD study. When growth rate

is determined by total film thickness divided by the 7-min growth time a different rate versus reciprocal temperature profile results.

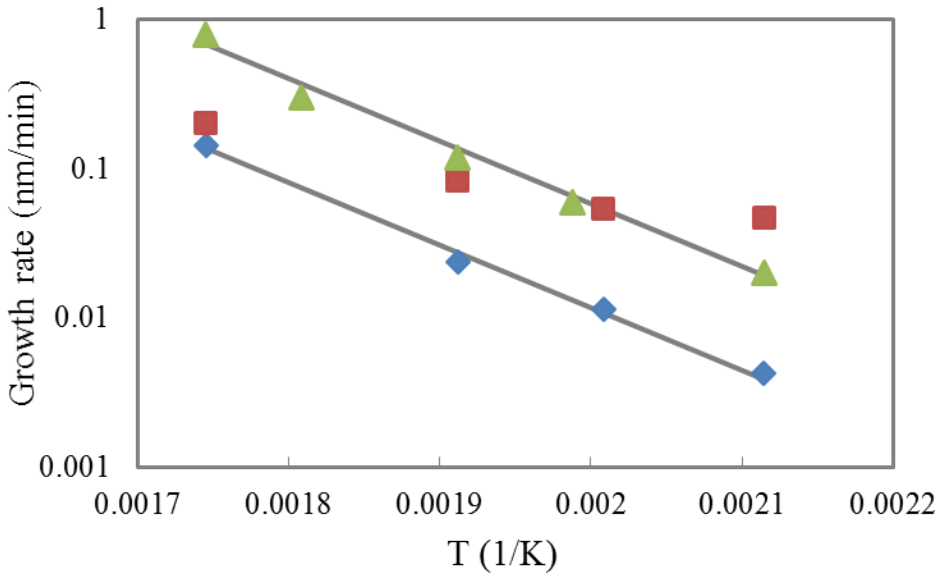

Figure 5.3: Ru growth rates versus reciprocal temperature for Ru(AMD): (green Δ) are effective growth rates based on ALD thicknesses reported by Li et al.,[12] (blue ◊) are our data considering a 0.3-nm wetting layer, and (red □) are our thickness data divided by 7 min. The lines are best fits of an Arrhenius expression to the rate versus reciprocal temperature.

CVD with Ru(AMD) at 473 K for 7 min produces a film with an XPS-based thickness of 0.33 nm. CVD was performed with $Ru_3(CO)_{12}$ at 473 K on a 1173-K annealed substrate for 30 min. A representative SEM image of the substrate and Ru nanoparticles is presented in Fig. 4a; there are on average 85 nanoparticles per 10,000 nm^2 with a diameter of 5.4 nm, and this corresponds to a Ru metal volume that would produce a 0.34-nm thick Ru film over the same area. Figure 4b presents a representative SEM image of the sample that results following CVD with Ru(AMD) and that has the XPS-based thickness of 0.34 nm. The 2-3-nm resolvable features in SEM have a density of 3-9 features per 10,000 nm^2 and the film equivalent thickness for these SEM features is 0.03 nm of Ru.

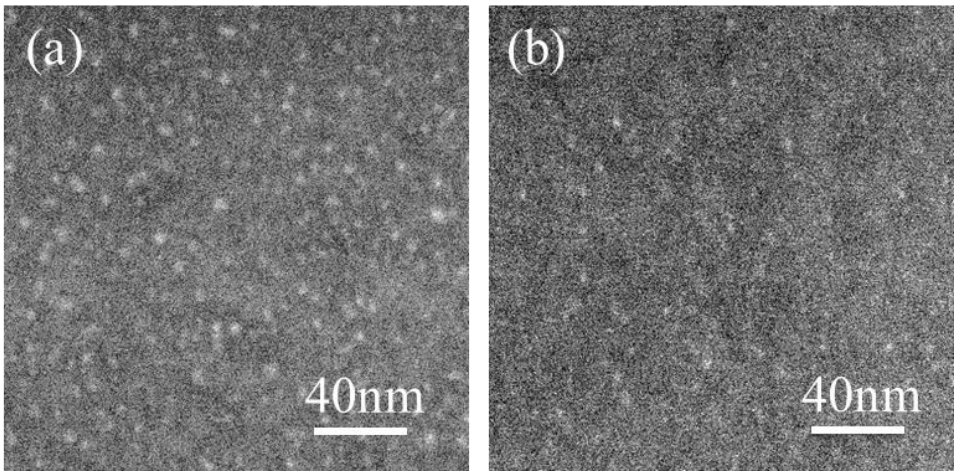

Figure 5.4: SEM images of film deposited with (a) $Ru_3(CO)_{12}$ and (b) Ru(AMD) precursors at ~0.3 nm XPS thickness.

5.3.3 CO or NH_3 effect on Ru CVD using the Ru(^{t}Bu-Me-amd)$_2$(CO)$_2$ precursor

Previous studies with CO and NH_3 addition along with $Ru_3(CO)_{12}$ revealed that film nucleation density, surface roughness and crystallinity were affected by the partial pressure of the added gas.[14,15] The studies with CO and NH_3 addition during CVD with Ru(AMD) were conducted at a fixed pressure of 4 mTorr of CO and 5 mTorr of NH_3 for films with three targeted thicknesses: 0.6, 4 and 20 nm. The thinnest films were deposited at 523 K for 10 min. Ru(AMD), Ru(AMD) plus CO and Ru(AMD) plus NH_3 produced XPS-based thicknesses of 0.61, 0.58 and 0.67 nm, respectively. Figure 5 presents the surface height distribution and root-mean-square (RMS) roughness that was determined by AFM of the three films and of the blank SiO_2 substrate. The blank SiO_2 substrate was cleaned using the same procedure and anneal as all other wafers before CVD and has a sharp and narrow height distribution peak at 0.7 nm and a 0.15-nm RMS roughness. Ru films deposited with CO and NH_3 have 0.21 and 0.22-nm RMS roughness, respectively, and a slightly wider height distribution peak centered at 0.8 nm. The film grown with Ru(AMD) only has the broadest height distribution centered at 1.2 nm and a 0.41-nm RMS roughness.

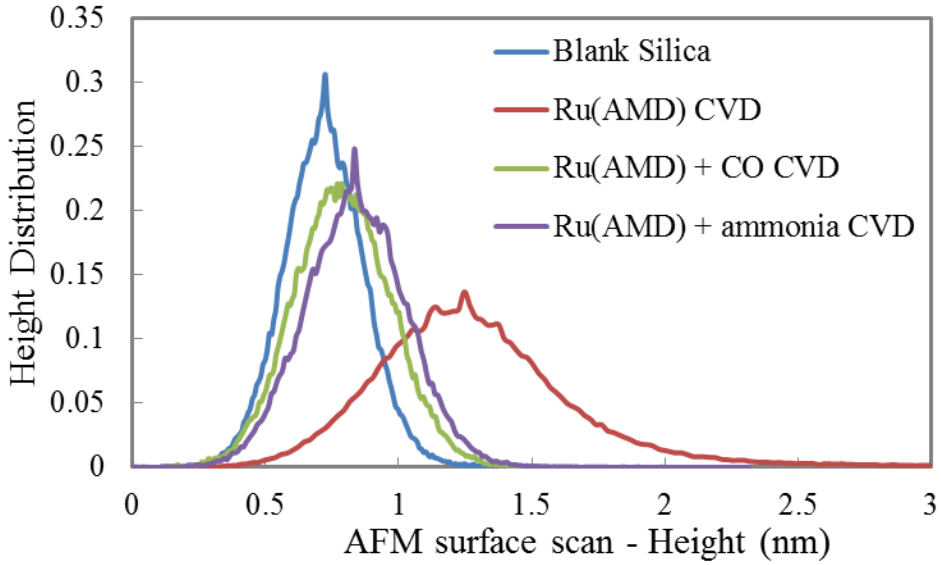

Figure 5.5: Surface height distributions measured by AFM of the blank substrate, 0.60 nm thick Ru film deposited with Ru(AMD) only, 0.57 nm thick Ru films deposited with Ru(AMD) and CO, and 0.67 nm thick Ru films deposited with Ru(AMD) and NH_3 addition.

Ru films were deposited at 573 K for 30 min with Ru(AMD) only or with Ru(AMD) plus 4 mTorr CO, and for 25 min with Ru(AMD) plus 5 mTorr NH_3 addition, leading to the film thickness of 4.3 , 3.9 and 4.5 nm, respectively. These film thicknesses were established by XRR. The AFM RMS roughness for these films is presented in Table 1. The films grown with CO and NH_3 displayed approximately half the roughness of the film grown only with Ru(AMD). Thin films grown with CO and NH_3 are smoother with smaller surface features than the film deposited with only Ru(AMD) based on the film surface topography scanned by AFM (Fig.6).

	XRR thickness	AFM roughness
Ru(AMD) only	4.3 nm	1.28 nm
+ 4 mTorr CO	3.9 nm	0.61 nm
+ 5 mTorr NH3	4.5 nm	0.68 nm

Table 5.1: Thin Ru films deposited at 573 K with Ru(AMD).

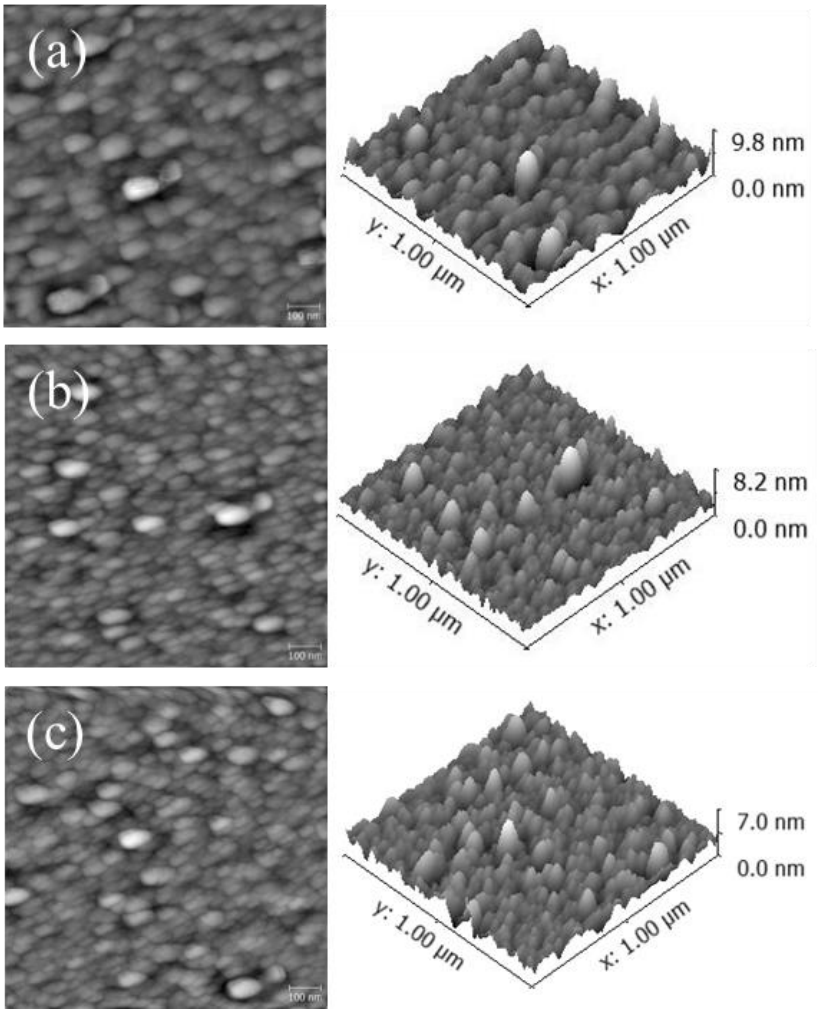

Figure 5.6: AFM surface scanning of thin Ru films at ~4 nm thickness deposited with (a) Ru(AMD) only, (b) Ru(AMD) and CO and (c) Ru(AMD) and NH_3.

The thick Ru films were grown to study the crystalline character of the films and to measure sheet resistivity by 4-point probe resistance measurement (Table 2). Thickness was established with XRR. Ru(AMD) deposited at 623 K for 40 min grows to a 22-nm thick film with 45 μΩ-cm resistivity. With 4 mTorr CO addition, 40 min Ru(AMD) deposition at 623 K leads to a 20-nm thick film with 38 μΩ-cm resistivity. Finally the film deposited at 623 K for 30 min with 5 mTorr NH_3 is 18-nm thick with 17 μΩ-cm resistivity. For reference, the bulk Ru resistivity is 7.1 μΩ-cm at 273 K.[4,6,7] Using both the thin (~4 nm) and thick (~20 nm) films the Ru growth rate is reduced 10% by CO addition and increased by 25% with NH_3 as compared to growth with Ru(AMD) alone. XRD spectra are presented in Fig. 7 and the grain sizes based on the Ru(101) diffraction feature are presented in Table 2. The thick Ru film deposited by Ru(AMD) has three strong and sharp crystallite peaks at Ru(100), Ru(002) and Ru(101) and the average grain size for the Ru(101) feature is 17.0 nm. When CO is added during the deposition, the three Ru peaks are weaker and broader, which means the crystallite grain sizes are smaller, and the Ru(101) feature corresponds to an average grain size of 12.2 nm. In the film deposited with NH_3, only Ru(100) and Ru(101) are detected by XRD and the crystallite grain size for Ru(101) is 16.4 nm. Ru(002) is absent in the XRD for the film deposited with NH_3, and its Ru(100) and Ru(101) peaks hold much lower intensity than the Ru film grown with CO addition or only with Ru(AMD).

Nitrogen was not detected in any of the films by XPS (spectra not shown). There is carbon residue (< 10%) on the film surfaces from *in situ* sample transfer, and the interior of films have a carbon concentration between 0 and 2%.[15]

	XRR thickness	Sheet resistivity	Ru(101) grain size
Ru(AMD) only	22 nm	45 μΩ-cm	16.99 nm
+ 4 mTorr CO	20 nm	38 μΩ-cm	12.20 nm
+ 5 mTorr NH3	18 nm	17 μΩ-cm	16.41 nm

Table 5.2: Thick Ru films deposited at 623 K with Ru(AMD) precursor.

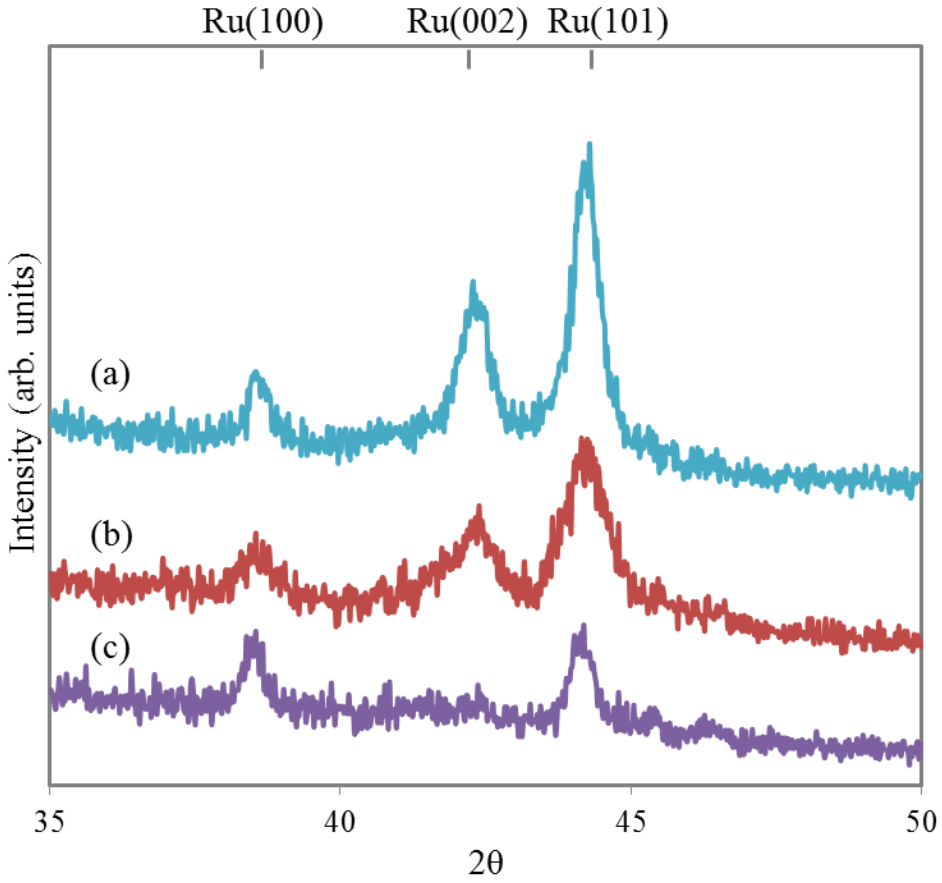

Figure 5.7: XRD of thick Ru films at ~20 nm thickness deposited with (a) Ru(AMD) only, (b) Ru(AMD) and CO and (c) Ru(AMD) and NH_3.

5.4 DISCUSSION

The previous studies reported that when CO and the $Ru_3(CO)_{12}$ precursor are added simultaneously to the CVD reaction chamber at the beginning of growth, the CO reduces the Ru nanoparticle density compared to the nucleation without CO.[14] With continued $Ru_3(CO)_{12}$ exposure the Ru islands can grow larger by direct reaction of $Ru_3(CO)_{12}$ with the already-formed Ru islands or by incorporating additional Ru that forms by reaction(s) of $Ru_3(CO)_{12}$ with SiO_2. The reason proposed[14] is the weak adsorption of carbon monoxide on $(Si\text{-}OH)_i$[47] producing an H-bonded complex,[48] which limits the Ru adatom formation at hydroxyl sites. Beebe et al. illustrated the physical adsorption of CO on silanol at 150 °C and a CO pressure of 40 Torr through infrared spectroscopy.[47] Carbon monoxide formed during $Ru_3(CO)_{12}$ decomposition or added to the reactor can compete with $Ru_3(CO)_{12}$ for adsorption sites on Ru islands or free isolated hydroxyls on SiO_2 through reversible adsorption processes.

To further verify the reaction of $Ru_3(CO)_{12}$ on SiO_2 $(Si\text{-}OH)_i$ groups, $Ru_3(CO)_{12}$ was deposited at low temperature on SiO_2 substrates pre-annealed at temperatures ranging from 473 to 1193 K because the $(Si\text{-}OH)_i$ concentration varies on SiO_2 with thermal pretreatment.[25] In Figs. 1 and 2, both SiO_2 $(Si\text{-}OH)_i$ groups and Ru nucleation by $Ru_3(CO)_{12}$ reach their maximum on the SiO_2 pre-annealed at 673 K. In addition, the pattern for changes in hydroxyl density and nanoparticle density with temperature are similar.

However, the relation between $(Si\text{-}OH)_i$ concentration ($\sim 10^{14}$ cm^{-2}) from the Zhuravlev model[25] and Ru nanoparticle ($\sim 10^{11}$ cm^{-2}) density using $Ru_3(CO)_{12}$ CVD suggests that either a small portion of the $(Si\text{-}OH)_i$ groups are involved in the Ru nucleation

or some other site such as oxygen vacancy defects, which have a density of 10^{11} cm^{-2}.[49,50] We suggest that the $(Si\text{-}OH)_i$ sites activate the $Ru_3(CO)_{12}$ precursor at the outset and that adatoms are trapped or coalesce into a stable cluster at different sites. The greater the number of adatoms before nucleation occurs, the higher the density of stable nuclei.[16,18,22] If oxygen vacancy defects or strained siloxane sites are the nucleation sites, the upper limit to expect is 10^{11} or 10^{12} cm^{-2}, respectively.[49] At the beginning of deposition, $Ru_3(CO)_{12}$ precursor vapor reacts with the $(Si\text{-}OH)_i$ groups and the denser the reactive sites on the substrate, the higher initial production of Ru adatoms. Once stable nuclei form, the additional $Ru_3(CO)_{12}$ is more likely to react with either $(Si\text{-}OH)_i$ groups or existing islands The data do not allow us to know if the $(Si\text{-}OH)_i$ groups are consumed in their reaction with $Ru_3(CO)_{12}$. The results confirm that a higher $(Si\text{-}OH)_i$ concentration created by thermal pretreatment of SiO_2 leads to a higher initial Ru nucleation density from $Ru_3(CO)_{12}$. Interestingly, Ru deposition from Ru(AMD) did not display any dependence on the $(Si\text{-}OH)_i$ density, as indicated by nanoparticles, or if it was dependent, the nature of the Ru growth masked this dependence.

Unlike the Volmer-Weber nucleation mode of $Ru_3(CO)_{12}$, the Ru(AMD) precursor appears to be deposited in a Stranski-Krastanov or 2DI mode. Nanoparticles are not observed with Ru(AMD) at any deposition temperature, rather featureless SEM images with very sparse particle-like features result (Fig. 4). XPS analysis after 7 min at 473 K indicates the presence of around 0.3 nm of Ru from Ru(AMD) and with $Ru_3(CO)_{12}$, this amount of Ru would generate a high density of observable Ru nanoparticles. The more rapid reaction of an amidinate-based precursor with Al_2O_3/SiO_2 than with metals Ru/Co/Cu

for copper(I) *N,N'*-di-sec-butylacetamidinate precursor has been reported.[26] As a mid-late transition/ noble metal, Ru might be expected to grow as 3D particles at the temperatures employed herein.[17] The growth rate data (Fig. 3) and the SEM images in Fig. 4, are consistent with a 2D wetting layer forming with Ru(AMD). By analogy to Cu and Ga amidinate-based precursor studies, the reasons for this 2D growth mode may be associated with Ru bonding directly to SiO at the surface before complete removal of a second amidinate ligand and/or changes in the surface energy of the SiO_2 if an amidine adsorbs on the SiO_2 surface.[27,28]

In the Stranski-Krastanov and 2DI mode of growth from Ru(AMD), CO or NH_3 addition smoothed out the Ru film through surface reconstruction. On the rough surface, atoms with fewer coordinated neighbors have higher flexibility and chemisorption of the adsorbate on the film surface induces the atom mobility.[30,31] Afterward, the break-up of this surface-adsorbate bonding relocates the surface atom to minimize surface free energy.[30,32] This surface relaxation develops smoother film and the reconstructed atoms with more neighbors are more rigid and less favored to the adsorbate gas. In the height distribution study (Fig. 5), a sharp peak means the surface is composed of dense and uniform features, while the broader and smaller peak means bumpy surface features of various sizes. The center of the height distribution curve indicates the average height of the surface features. On the 0.6-nm thick Ru film deposited at 523 K, the Ru(AMD)-CVD film with a broad distribution centered at 1.2 nm height indicates a rough surface. In comparison, the films deposited with CO or NH_3 have narrow sharp peaks centered at 0.8 nm height representing more uniform and small topography on the surface (Fig. 5).

Extending to ~4-nm-thick Ru films deposited at 573 K, the thin films grown from smaller and denser particles with CO or NH_3 addition are smoother than the film grown without inhibitors, obtaining half of the RMS roughness and smaller surface features through AFM investigations (Table 1, Fig. 6). Thick Ru films (~20 nm thickness) were grown for better XRD crystallinity resolution and sheet resistant measurement. A 22-nm thick film deposited by Ru(AMD) CVD has three strong peaks at Ru(100), Ru(002) and Ru(101) (Fig. 7) and its sheet resistivity is 45 μΩ-cm. Sheet resistivity is highly related to film thickness, surface roughness and average grain size,[51] and sheet resistivity decreases with increasing film thickness. A smooth film is more conductive because of less surface roughness-induced scattering. As the grain size decreases, transmission and reflection at interfaces increase the resistivity. In the 20-nm thick Ru film deposited by Ru(AMD) with CO addition, the film resistivity is 38 μΩ-cm with much smoother surface and 30% smaller grain size on average compared to the 22-nm film deposited without inhibitor. The XRD spectrum of the 18-nm thick film deposited with both Ru(AMD) and NH_3 at 623 K shows two small peaks at Ru(100) and Ru(101).The smooth and moderately-amorphous film deposited with added-NH_3 has the lowest sheet resistivity at 17 μΩ-cm.

Ru films sputtered in N_2 and Ar atmospheres incorporate N and display better diffusion barrier characteristics with N dissolved in the Ru film versus films that were annealed to remove the dissolved N.[52] Nitrogen starts to effuse from the amorphous Ru-N film and the film crystalizes above 548K.[52] The 18-nm film grown herein with NH_3 addition displays more amorphous character than the other films of similar thickness and the microstructure is likely associated with N adsorbed on the surface or during growth.[15]

As a co-reactant, NH_3 increases the growth rate without affecting the average grain size in the crystalized portion (Table 2). In polycrystalline films, copper diffuses between the grain boundaries and the grain boundaries are sites for electron scattering. As a result, films grown from Ru(AMD) and NH_3 should perform the better as a copper diffusion barrier than films grown with CO or without any added blocking gas.

In general, CO or NH_3 addition during Ru CVD can be expected to improve Ru thin film performance as a diffusion barrier. CO or NH_3 addition reduces the Ru thin film roughness and crystallinity compared to the metallic films deposited without an adsorbate gas. When a precursor grows by Volmer-Weber (3D) growth, nucleation density is increased by CO or NH_3 addition by generating a higher density of the nuclei and with a smaller size that coalesce to a smoother and thinner Ru film.[14,15] Alternatively, CO or NH_3 adsorption on films that follow Stranski-Krastanov or 2DI growth induces surface reconstruction to minimize the Ru surface free energy with the net effect of smoother films.

5.5 CONCLUSION

With free hydroxyl groups as activation sites, the $Ru_3(CO)_{12}$ forms adatoms that nucleate and grow in a VW 3D mode on silica. This free hydroxyl density on SiO_2 is manipulated by thermal pretreatment to enhance the initial nucleation density of the first sub-monolayer by surface chemistry. Stranski-Krastanov or 2DI growth is found with Ru(AMD) and 0.3-nm wetting layer forms quickly on SiO_2 followed by slower growth of Ru on Ru. 3D structures form on the 2D wetting layer. The addition of CO and NH_3 during CVD with Ru(AMD) can be used to control film texture and roughness by surface

through adsorbate-induced reconstruction. CO and NH_3 addition sufficiently reduces the film roughness, nanocrystallite grain size and sheet resistivity for films grown with Ru(AMD).

5.6 REFERENCES

1. A. E. Kaloyeros and E. Eisenbraun, Annu. Rev. Mater. Sci. **30**, 363–385 (2000).
2. International Technology Roadmap for Semiconductors, *Interconnect Summary* (International Roadmap Committee, Semiconductor Industry Associations of the United States, Europe, Japan, South Korea, and Taiwan, 2013).
3. P. J. Estrup and J. Anderson, J. Chem. Phys. **49**, 523–528 (1968).
4. I. Goswami and R. Laxman, Semicond. Int. **27**, 49–54 (2004).
5. H. Kim, Surf. Coatings Technol. **200**, 3104–3111 (2006).
6. R. Chan, T. N. Arunagiri, Y. Zhang, O. Chyan, R. M. Wallace, M. J. Kim and T. Q. Hurd, Electrochem. Solid-State Lett. **7**, G154–G157 (2004).
7. M. L. Green, M. E. Gross, L. E. Papa, K. J. Schnoes and D. Brasen, J. Electrochem. Soc. **132**, 2677–2685 (1984).
8. J. E. Crowell, J. Vac. Sci. Technol. A **21**, S88–S94 (2003).
9. J. C. Vigui and J. Spitz, J. Electrochem. Soc. **122**, 585–588 (1975).
10. Y. Matsui, M. Hiratani, T. Nabatame, Y. Shimamoto and S. Kimura, Electrochem. Solid-State Lett. **4**, C9–C12 (2001).
11. Q. Wang, J. G. Ekerdt, D. Gay, Y. M. Sun and J. M. White, Appl. Phys. Lett. **84**, 1380–1382 (2004).
12. H. Li, D. B. Farmer, R. G. Gordon, Y. Lin and J. Vlassak, J. Electrochem. Soc. **154**, D642–D647 (2007).
13. R. G. Gordon, H. Li, T. Aaltonen, B. S. Lim and Z. Li, Open Inorg. Chem. J. **2**, 11–17 (2008).

14. W. Liao and J. G. Ekerdt, Chem. Mater. **25**, 1793–1799 (2013).

15. W. Liao and J. G. Ekerdt, J. Vac. Sci. Technol. A **34**, 031508 (2016)

16. H. Brune, Surf. Sci. Rep. **31**, 121–229 (1998).

17. C. T. Campbell, Surf. Sci. Rep. **27,** 1–111 (1997).

18. C. Ratsch and J. A. Venables, J. Vac. Sci. Technol. A **21**, S96–S109 (2003).

19. J. A. Venables, G. D. T. Spiller and M. Hanbucken, Reports Prog. Phys. **47,** 399–459 (1984).

20. S. S. Coffee and J. G. Ekerdt, J. Appl. Phys. **102,** 114912 (2007).

21. T. A. Witten and L. M. Sander, Phys. Rev. Lett. **47**, 1400–1403 (1981).

22. P. Mulheran and M. Basham, Phys. Rev. B **77,** 075427 (2008).

23. A. Theolier, A. Choplin, L. D'Ornelas, J.M. Basset, G. Zanderighi and C. Sourisseau, Polyhedron **2**, 119–121 (1983).

24. G. M. Zanderighi, C. Dossi, R. Ugo, R. Psaro, A. Theolier, A. Choplin, L. D'Ornelas and J.M. Basset, J. Organomet. Chem. **296**, 127–146 (1985).

25. L. T. Zhuravlev, Colloids Surfaces A Physicochem. Eng. Asp. **173,** 1–38 (2000).

26. Z. Li, A. Rahtu and R. G. Gordon, J. Electrochem. Soc. **153,** C787–C794 (2006).

27. M. Dai, J. Kwon, M. D. Halls, R. G. Gordon and Y. J. Chabal, Langmuir, **26**, 3911–3917 (2010).

28. P. J. Pallister, S. C. Buttera and S. T. Barry, J. Phys. Chem. C, **118**, 1618−1627 (2014)

29. V. P. Zhdanov and K. I. Zamaraev, Sov. Phys. Usp. **29,** 755–776 (1986).

30. G. A. Somorjai, Surf. Sci. **335,** 10–22 (1995).

31. G. A. Somorjai, Annu. Rev. Phys. Chem. **45,** 721–751 (1994).

32. S. Titmuss, A.Wander and D. A. King, Chem. Rev. **96,** 1291–1306 (1996).

33. W. H. Lee, K. R. Vanloon, V. Petrova, J. B. Woodhouse, C. M. Loxton and R. I. Masel, J. Catal. **126,** 658–670 (1990).

34. A. Shi and R. Masel, J. Cat. **120,** 421–431 (1989).

35. W. H. Lee, V. Petrova, K. R. Vanloon, J. B. Woodhouse, C. M. Loxton N. L. Finnegan, and R. I. Masel, Catal. Denctiuation, 597–603 (1991).

36. A. C. Shi, K. K. Fung, J. F. Welch, M. Wortis and R. I. Masel, Mater. Res. Sociely **111,** 59–64 (1988).

37. N. Kruse and A. Gaussmann, Surf. Sci. **266,** 51–55 (1992).

38. J. Shin, A. Waheed, W. A. Winkenwerder, H. W. Kim, K. Agapiou, R. A. Jones, G. S. Hwang and J. G. Ekerdt, Thin Solid Films **515,** 5298–5307 (2007).

39. J. Shin, H. W. Kim, G. S. Hwang and Ekerdt, J. G. Surf. Coatings Technol. **201,** 9256–9259 (2007).

40. L. B. Henderson and Ekerdt, J. G. J. Electrochem. Soc. **157,** D29–D34 (2010).

41. J. R. Shallenberger, D.A. Cole, S.W. Novak and R.L. Moore, 1998 Int. Conf. Ion Implant. Technol. Proc. (Cat. No.98EX144) **1,** 79–82 (1999).

42. G. Lewis and P. G. Fox, Corros. Sci. **18,** 645–650 (1978).

43. A. V. Naumkin, A. Kraut-Vass, S. W. Gaarenstroom and C. J. Powell, *NIST Standard Reference Database 20, Version 4.1.* Meas. Serv. Div. Natl. Inst. Stand. Technol. (2012).

44. A. Jablonski and J. Zemek, Surf. Interface Anal. **41,** 193–204 (2009).

45. J. Shin, D. Gay, Y. M. Sun, J. M. White and Ekerdt, J. G. AIP Conf. Proc. **788,** 482–487 (2005).

46. P. Scherrer, Math. Klasse **2,** 98–100 (1918).

47. T. P. Beebe, P. Gelin and J. T. Yates Jr., Surf. Sci. **148**, 526–550 (1984).

48. G. Ghlotti, E. Garrone, C. Morterra and F. Boccuzzi, J. Phys. Chem. **83**, 2863–2869 (1979).

49. J. M. McCrate and J. G. Ekerdt, AIChE J. **62,** 367–372 (2016).

50. J. M. McCrate and J. G. Ekerdt, Chem. Mater. **26,** 2166–2171 (2014).

51. S. M. Rossnagel and T. S. Kuan, J. Vac. Sci. Technol. B Microelectron. Nanomater. Struct. **22,** 240–247 (2004).

52. M. Damayanti, T. Sritharan, S. G. Mhaisalkar and Z. H. Gan, Appl. Phys. Lett. **88,** 044101 (2006).

Chapter 6: Summary

6.1 Conclusion

Ruthenium was deposited on SiO_2/Si(001) substrates at 473 K by chemical vapor deposition (CVD) using triruthenium dodecacarbonyl with and without an overpressure of CO. Carbon monoxide was employed to inhibit the growth of previously-nucleated islands to allow the formation of additional nuclei. Carbon monoxide also competed with the precursor for free hydroxyl sites on SiO_2 sites where precursor adsorption and decomposition is favored. Total pressure was maintained at 84 mTorr and CO was introduced at partial pressures of 2.5 and 8.4 mTorr at various intervals during 15 min growth runs. The nucleation density decreases with increasing CO overpressure when CO and precursor are injected simultaneously from the beginning; in this case, CO blocks the free hydroxyls where the Ru precursor dissociates. When 8.4 mTorr CO is introduced for 5 min to the CVD chamber after a 10 min period of deposition without CO, the maximum nucleation density was achieved (16.4×10^{11} /cm²), which is twice as much as the Ru particle density found for 15 min deposition without added CO. After 10 min of growth hydroxyl groups have mostly reacted and the injected CO adsorbs on Ru nanoparticles, inhibiting growth and forcing additional Ru nucleation on the SiO_2 substrate. Growth was extended to 2 hr to explore the influence of CO on ultra-thin Ru film characteristics. The film grown without CO for 10 min and then with 8.4 mTorr CO for 1 hr 50 min was thinner and smoother than the film grown without CO for 2 hr because CO adsorption on the Ru surface slows the Ru islands/film growth rate.

This study also reports the use of ammonia to inhibit the growth of previously-nucleated ruthenium islands and force the nucleation of additional islands such that thinner films form as the islands coalesce with continued growth. Ruthenium films are grown at 448 K in a chemical vapor deposition process on SiO_2/Si(001) using triruthenium dodecacarbonyl, $Ru_3(CO)_{12}$, with and without a constant partial pressure of ammonia. Film growth was performed at a $Ru_3(CO)_{12}$/Ar pressure of 47.2 mTorr. The ammonia partial pressure varied from 0 to 27.8 mTorr. X-ray photoelectron spectroscopy was used to analyze the samples *in situ*. *Ex situ* characterization included scanning electron microscopy, atomic force microscopy, and X-ray diffraction and X-ray reflectivity. Nucleation studies limited to the first 10 min of growth revealed the maximum nanoparticle (island) density of 8.1×10^{11} cm^{-2} occurred at an intermediate ammonia pressure (5.25 mTorr) compared to a density of 3.1×10^{11} cm^{-2} for no ammonia addition. Extending film growth to 120 min and varying the ammonia partial pressure during the first 10 min followed by 5.25 mTorr ammonia pressure for the final 110 min reveals the importance of nucleation on film smoothness. A model describing the inhibition effects of ammonia during nucleation and growth is presented.

Nucleation and film growth characteristics are reported during chemical vapor deposition of Ru on SiO_2 using triruthenium dodecacarbonyl ($Ru_3(CO)_{12}$) and ruthenium bis(di-t-butylacetamidinate) dicarbonyl ($Ru(^tBu\text{-}Me\text{-}amd)_2(CO)_2$). Films grown from $Ru_3(CO)_{12}$ follow the three dimensional (3D) Volmer-Weber growth mode. In contrast, films grown from $Ru(^tBu\text{-}Me\text{-}amd)_2(CO)_2$ follow the pseudo-layer-by-layer growth mode with two dimensional wetting layer islands forming before 3D particle growth is observed

on the islands. A relationship between free isolated hydroxyl ($(Si\text{-}OH)_i$) group density and Ru nucleation density is found for $Ru_3(CO)_{12}$ and is associated with $(Si\text{-}OH)_i$ acting as the reaction sites for activation of $Ru_3(CO)_{12}$ and in turn generating an adjustable adatom concentration. Carbon monoxide and ammonia addition to the gas phase during film growth from $Ru(^tBu\text{-}Me\text{-}amd)_2(CO)_2$ lead to smoother films by inducing surface reconstructions during the 3D phase of pseudo-layer-by-layer growth; these gases also lead to films with lower resistivity and lower crystalline character.

6.2 FUTURE WORK

This study explores the use of inhibitors that can block adsorption of the metal precursor and kinetically force the growth of ultra-thin metal films, such as Ru, Co and W. Continuing with the ruthenium example carbon monoxide (CO) has the potential to occupy the surface of Ru islands and thereby encourage addition nucleation on the oxide substrate surface. As the potential Fischer–Tropsch synthesis catalysts,[4] the adsorption[5] and dissociation[6] of CO on various Ru[7–9] and Co[4,10] crystal surfaces have been reported. Comparable metallic compounds with carbonyl ligands, such as $Co_2(CO)_8$[11–13] and $W(CO)_6$[14–17] have been reported as effective CVD precursors. Metal carbonyls decompose at from 100 to 500 °C at low pressure/ high vacuum. In the study of CO bonding on transition-metal, the adsorption energy of CO on W is slightly higher than on Co and Ru surfaces.[18] The CO addition during Co and W CVD could be investigated and optimized for nucleation and following ultra-thin film growth. Besides, other metal precursors could be studied to strengthen the CO blocking effect more broadly.

For some metallorganic precursors, the ligands may decompose to small carbonhydrons (C_xH_y) or hydrogen, which are reactive to CO.[19–22] To solve this limitation, the study of more inert adatoms, such as ammonia and halogen sources is suggested.

Similar to CO, NH_3 is also a promising material in interrupting metal island growth to force additional nucleation. The NH_3 is expected to form NH_x (x=2-0) depending on the metal, temperature and particle pressure of NH_3 and H_2. Ammonia synthesis and decomposition are usually catalyzed by transition metals.[23] Single crystal tungsten is reported catalyzing ammonia decomposition from 530 °C on surface in ultra-high vacuum.[24] Ammonia adsorbs on and dissociates from the metal crystal surfaces, so it has the potential to block the metal sites during CVD.[24–26] Moreover, in particular circumstances, either NH_3 or a mixture of N_2 and H_2 can perform as co-reactants to deposit metal nitride films, which are more likely to grow amorphous films.[27] For example, TiN, WN_x and WN_xC_y film has been deposited with NH_3 and H_2 addition, and analyzed as an excellent copper diffusion barrier.[28–30] Nitrogen binds on the ammonia synthesis catalysts more strongly than on the decomposition catalysts. Ammonia adsorbs on easily and desorbs slowly from the synthesis catalyst.[25] In this case, the content of N in film and the characteristics of this N impurity should be investigate, as well as the ammonia inhibitor influence on nucleation and film growth. On the decomposition catalyst surface, like W, the large coverage of intermediate $–NH_2$ reduces ammonia's regular adsorption and desorption significantly.[24] To minimize this side effect of ammonia, an overpressure H_2 flow could participate to minimize this reversible decomposition for the general inhibitor exploration.

Halogens adsorb dissociatively on most of transition metal surfaces and form submonolayer coverage at temperature between 100 and 500 K.[31–33] Based on the heterogeneously catalyzed conversion of hydrocarbons in crude oil refinement, chemisorption of alkyl-halides on metal surfaces provide potential sources as adsorbates inhibiting island growth.[32,34] Alkyl-iodine addition has sufficiently improved the metal nucleation density and film smoothness.[35,36] Iodine sources, such as CH_3I[35,37] and C_2H_5I[37,38], in concert with $Ru(EtCp)_2$ are shown to enhance the nucleation density dramatically so as to improve film smoothness. Iodine worked with a Ru precursor that also needed co-reacting O_2 and may have functioned by surface segregating to the Ru surface and inhibiting oxygen adsorption on nucleated islands, which forced additional nuclei to form.[35] Iodomethane, as the representative of halogen sources, could be used to study the applicability of iodine anchoring more transition metal nuclei surfaces and forcing additional nucleation to grow thinner and smoother film. Furthermore, experiments of alkyl-Cl,Br participation in metal film development could be performed upon the understanding of iodine source mechanism.

In summary, a general understanding of the blocking adsorbate effect on nucleation and ultra-thin film growth using CVD should be explored. Plus, the advantages and limitations of each species of blocking adsorbate should be explored.

6.3 REFERENCE

1. Zhuravlev, L. T. *Colloids Surfaces A Physicochem. Eng. Asp.* **173,** 1–38 (2000).
2. Theolier, A., Choplin, A., D'Ornelas, L., Basset, J. M., Zanderighi, G. and

Sourisseau, C. *Polyhedron* **2,** 119–121 (1983).

3. Zanderighi, G. M., Dossi, C., Ugo, R., Psaro, R., Theolier, A., Choplin, A., D'Ornelas, L. and Basset, J. M. *J. Organomet. Chem.* **296,** 127–146 (1985).

4. Schulz, H. *Appl. Catal. A Gen.* **186,** 3–12 (1999).

5. Davydov, A. A. and Bell, A. T. *J. Catal.* **49,** 332–344 (1977).

6. Strebel, C., Murphy, S., Nielsen, R. M., Nielsen, J. H. and Chorkendorff, I. *Phys. Chem. Chem. Phys.* **14,** 8005–12 (2012).

7. Pfnür, H. and Menzel, D. *J. Chem. Phys.* **79,** 2400–2410 (1983).

8. Pfnür, H., Feulner, P., Engelhardt, H. A. and Menzel, D. *Chem. Phys. Lett.* **59,** 481–486 (1978).

9. Thomas, G. E. and Weinberg, W. H. *J. Chem. Phys.* **70,** 1437–1439 (1979).

10. Shetty, S. and van Santen, R. A. *Catal. Today* **171,** 168–173 (2011).

11. Zhao, Q., Greve, D. W. and Barmak, K. *Appl. Surf. Sci.* **219,** 136–142 (2003).

12. Henderson, L. B. and Ekerdt, J. G. *J. Electrochem. Soc.* **157,** D29–D34 (2010).

13. Boyd, E. P., Ketchum, D. R., Deng, H. and Shore, S. G. *Chem. Mater.* **9,** 1154–1158 (1997).

14. Lai, K. K. and Lamb, H. H. *Thin Solid Films* **370,** 114–121 (2000).

15. Tanner, R. E., Szekeres, A., Gogova, D. and Gesheva, K. *Appl. Surf. Sci.* **218,** 163–169 (2003).

16. Gesheva, K. A., Vlakhov, E. S., Stoyanov, G. I. and Beshkod, B. G. D. *Ceram. Int.* **22,** 87–89 (1996).

17. Shimizu, H., Sakoda, K. and Shimogaki, Y. *Microelectron. Eng.* **106,** 91–95 (2013).

18. Andreoni, W. and Varma, C. M. *Phys. Rev. B* **23,** 437–444 (1981).

19. Pasko, S., Hubert-Pfalzgraf, L. G., Abrutis, A. and Vaissermann, J. *Polyhedron* **23,** 735–741 (2004).

20. Kang, S. Y., Choi, K. H., Lee, S. K., Hwang, C. S. and Kim, H. J. *J. Electrochem.*

Soc. **147,** 1161–1167 (2000).

21. Matsui, Y., Hiratani, M., Nabatame, T., Shimamoto, Y. and Kimura, S. *Electrochem. Solid-State Lett.* **4,** C9–C12 (2001).

22. Spee, C. I. M. A., Verbeek, F., Kraaijkamp, J. G., Linden, J. L., Rutten, T., Delhaye, H., van der Zouwen, E. A. and Meinema, H. A. *Mater. Sci. Eng. B* **17,** 108–111 (1993).

23. Boisen, A., Dahl, S., Norskov, J. K. and Christensen, C. H. *J. Catal.* **230,** 309–312 (2005).

24. Estrup, P. J. and Anderson, J. *J. Chem. Phys.* **49,** 523–528 (1968).

25. Dahl, S., Taylor, P. A., Törnqvist, E. and Chorkendorff, I. *J. Catal.* **178,** 679–686 (1998).

26. Wilf, M. and Folman, M.. *J. Chem. Soc.* **72,** 1165–1176 (1975).

27. Kaloyeros, A. E. and Eisenbraun, E. *Annu. Rev. Mater. Sci.* **30,** 363–385 (2000).

28. Sari, W., Eom, T.-K., Jeon, C.-W., Sohn, H. and Kim, S.-H. *Electrochem. Solid-State Lett.* **12,** H248 (2009).

29. Anacleto, A. C., Blasco, N., Pinchart, A., Marot, Y. and Lachaud, C. *Surf. Coatings Technol.* **201,** 9120–9124 (2007).

30. Perez-Mariano, J., Lau, K.-H., Sanjurjo, a., Caro, J., Prado, J. M. and Colominas, C. *Surf. Coatings Technol.* **201,** 2174–2180 (2006).

31. Myli, K. B. and Grassian, V. H. *Langmuir* **11,** 849–852 (1995).

32. Zaera, F. *Acc. Chem. Res.* **25,** 260–265 (1992).

33. Hinzert, H., Kleinherbers, K. K., Janssen, E. and Goldmann, A. *Appl. Phys. A Solids Surfaces* **49,** 313–320 (1989).

34. Kis, A., Kiss, J. and Solymosi, F. *Surf. Sci.* **459,** 149–160 (2000).

35. Thom, K. M. and Ekerdt, J. G. *Thin Solid Films* **518,** 36–42 (2009).

36. Hwang, E. S. and Lee, J. *Electrochem. Solid-State Lett.* **3,** 138–140 (2000).

37. Kim, J. J., Jung, D. H., Kim, M. S., Kim, S. H. and Yoon, D. Y. *Thin Solid Films* **409,** 28–32 (2002).

38. Kim, J. J., Kim, M. S. and Yoon, D. Y. *Chem. Vap. Depos.* **9,** 105–109 (2003).

Bibliography

Anacleto, A. C., Blasco, N., Pinchart, A., Marot, Y. and Lachaud, C., Novel cyclopentadienyl based precursors for CVD of W containing films. *Surface and Coatings Technology*, *201*(22-23), 9120–9124 (2007).

Andreoni, W. and Varma, C. M., Binding and dissociation of CO on transition-metal surfaces. *Physical Review B*, *23*(2), 437–444 (1981).

Babar, S., Kumar, N., Zhang, P., Abelson, J. R., Dunbar, A. C., Daly, S. R. and Girolami, G. S., Growth inhibitor to homogenize nucleation and obtain smooth HfB_2 thin films by chemical vapor deposition. *Chemistry of Materials*, *25*, 662–667 (2013).

Beebe, T. P., Gelin, P. and Yates Jr., J. T., Infrared spectroscopic observations of surface bonding in physical adsorption: The physical adsorption of CO on SiO_2 surfaces. *Surface Science*, *148*(2-3), 526–550 (1984).

Boisen, A., Dahl, S., Norskov, J. K. and Christensen, C. H., Why the optimal ammonia synthesis catalyst is not the optimal ammonia decomposition catalyst. *Journal of Catalysis*, *230*(2), 309–312 (2005).

Bost, D. E. and Ekerdt, J. G., Chemical vapor deposition of ruthenium–phosphorus alloy thin films: Using phosphine as the phosphorus source. *Thin Solid Films*, *558*, 160–164 (2014).

Boyd, E. P., Ketchum, D. R., Deng, H. and Shore, S. G., Chemical vapor deposition of metallic thin films using homonuclear and heteronuclear metal carbonyls. *Chemistry of Materials*, *9*, 1154–1158 (1997).

Brune, H., Microscopic view of epitaxial metal growth: Nucleation and aggregation. *Surface Science Reports*, *31*, 121–229 (1998).

Campbell, C. T., Ultrathin metal films and particles on oxide surfaces: structural, electronic and chemisorptive properties. *Surface Science Reports*, *27*(1-3), 1–111 (1997).

Chan, R., Arunagiri, T. N., Zhang, Y., Chyan, O., Wallace, R. M., Kim, M. J. and Hurd, T. Q., Diffusion studies of copper on ruthenium thin film: a plateable copper diffusion barrier. *Electrochemical and Solid-State Letters*, *7*(8), G154–G157 (2004).

Coffee, S. S. and Ekerdt, J. G., Investigation of Volmer-Weber growth mode kinetics for germanium nanoparticles on hafnia. *Journal of Applied Physics*, *102*(11), 114912 (2007).

Crowell, J. E., Chemical methods of thin film deposition: Chemical vapor deposition, atomic layer deposition, and related technologies. *Journal of Vacuum Science & Technology A: Vacuum, Surfaces, and Films*, *21*(5), S88–S94 (2003).

Dahl, S., Taylor, P. A., Törnqvist, E. and Chorkendorff, I., The Synthesis of ammonia over a ruthenium single crystal. *Journal of Catalysis*, *178*, 679–686 (1998).

Damayanti, M., Sritharan, T., Mhaisalkar, S. G. and Gan, Z. H., Effects of dissolved nitrogen in improving barrier properties of ruthenium. *Applied Physics Letters*, *88*, 044101 (2006).

Davydov, A. A. and Bell, A. T., An infrared study of NO and CO adsorption on a silica-supported Ru catalyst. *Journal of Catalysis*, *49*, 332–344 (1977).

Estrup, P. J. and Anderson, J., Adsorption and decomposition of ammonia on a single-crystal tungsten (100) surface. *The Journal of Chemical Physics*, *49*(2), 523–528 (1968).

Fan, C. Y., Bonzel, H. P. and Jacobi, K., CO adsorption on the multiple-site Ru(11$\bar{2}$1) surface: The role of bonding competition. *The Journal of Chemical Physics*, *118*(21), 9773 (2003).

Gesheva, K. A., Vlakhov, E. S., Stoyanov, G. I. and Beshkod, B. G. D., Deposition and characterization of CVD-tungsten and tungsten carbonitrides on (100) Si. *Ceramics International*, *22*, 87–89 (1996).

Ghlotti, G., Garrone, E., Morterra, C. and Boccuzzi, F., Infrared study of low temperature adsorption. 1. CO on aerosil. An interpretation of the hydrated silica spectrum. *The Journal of Physical Chemistry*, *83*(22), 2863–2869 (1979).

Gordon, R. G., Li, H., Aaltonen, T., Lim, B. S. and Li, Z., Synthesis and characterization of ruthenium amidinate complexes as precursors for vapor deposition. *The Open Inorganic Chemistry Journal*, *2*(1), 11–17 (2008).

Goswami, I. and Laxman, R., Transition metals show promise as copper barriers. *Semiconductor International*, *27*, 49–54 (2004).

Green, M. L., Gross, M. E., Papa, L. E., Schnoes, K. J. and Brasen, D., Chemical vapor deposition of ruthenium and ruthenium dioxide films. *Journal of The Electrochemical Society*, *132*(11), 2677–2685 (1984).

Henderson, L. B. and Ekerdt, J. G. Effect of phosphorus and carbon incorporation in amorphous cobalt films prepared by chemical vapor deposition. *Journal of The Electrochemical Society*, *157*(1), D29–D34 (2010).

Hendrickson, D. N., Hollander, J. M. and Jolly, W. L., Nitrogen 1s electron binding energies. correlations with molecular orbital calculated nitrogen charges. *Inorganic Chemistry*, *8*(12), 2642–2647 (1969).

Hinzert, H., Kleinherbers, K. K., Janssen, E. and Goldmann, A., Chemisorption of halogens on silver a critical comparison of results from photqemission and thermal desorption spectroscopy. *Applied Physics A Solids and Surfaces*, *49*(3), 313–320 (1989).

Hwang, E. S. and Lee, J., Surfactant-assisted metallorganic CVD of (111)-oriented copper films with excellent surface smoothness. *Electrochemical and Solid-State Letters*, *3*(3), 138–140 (2000).

International Technology Roadmap for Semiconductors, *Interconnect Summary* (International Roadmap Committee, Semiconductor Industry Associations of the United States, Europe, Japan, South Korea, and Taiwan, 2013).

Jablonski, A. and Zemek, J., Owerlayer thickness determination by XPS using the multiline approach. *Surface and Interface Analysis*, *41*(3), 193–204 (2009).

Kaloyeros, A. E. and Eisenbraun, E., Ultrathin diffusion barriers/liners for gigascale copper metallization. *Annual Review of Material Science*, *30*, 363–385 (2000).

Kang, S. Y., Choi, K. H., Lee, S. K., Hwang, C. S. and Kim, H. J., Thermodynamic calculations and metallorganic chemical vapor deposition of ruthenium thin films using bis(ethyl-pi-cyclopentadienyl) Ru for memory applications. *Journal of The Electrochemical Society*, *147*(3), 1161–1167 (2000).

Kim, H., The application of atomic layer deposition for metallization of 65 nm and beyond. *Surface and Coatings Technology*, *200*, 3104–3111 (2006).

Kim, H., Rabelo de Moraes, I., Tremiliosi-Filho, G., Haasch, R. and Wieckowski, A., Chemical state of ruthenium submonolayers on a Pt(111) electrode. *Surface Science*, *474*(1-3), L203–L212 (2001).

Kim, J. J., Jung, D. H., Kim, M. S., Kim, S. H. and Yoon, D. Y., Surface roughness reducing effect of iodine sources (CH_3I, C_2H_5I) on Ru and RuO_2 composite films grown by MOCVD. *Thin Solid Films*, *409*, 28–32 (2002).

Kim, J. J., Kim, M. S. and Yoon, D. Y., Effects of an added iodine source (C_2H_5I) on Ru metal-organic CVD. *Chemical Vapor Deposition*, *9*(2), 105–109 (2003).

Kis, A., Kiss, J. and Solymosi, F., Reaction of CH_2 with adsorbed O on Ru(001) surface. *Surface Science*, *459*, 149–160 (2000).

Kruse, N. and Gaussmann, A., Changes in the morphology of Rh field emitter tips due to the reaction with carbon monoxide. *Surface Science*, *266*(1-3), 51–55 (1992).

Kumar, N., Yanguas-Gil, A., Daly, S. R., Girolami, G. S. and Abelson, J. R., Growth inhibition to enhance conformal coverage in thin film chemical vapor deposition. *Journal of the American Chemical Society*, *130*, 17660–17661 (2008).

Lai, K. K. and Lamb, H. H., Tungsten chemical vapor deposition using tungsten hexacarbonyl: microstructure of as-deposited and annealed films. *Thin Solid Films*, *370*, 114–121 (2000).

Lai, Y.-H., Chen, Y.-L., Chi, Y., Liu, C.-S., Carty, A. J., Peng, S.-M. and Lee, G.-H., Deposition of Ru and RuO_2 thin films employing dicarbonyl bis-diketonate ruthenium complexes as CVD source reagents. *Journal of Materials Chemistry*, *13*(8), 1999–2006 (2003).

Lee, W. H., Petrova, V., VanLoon, K. R., Woodhouse, J. B., Loxton, C. M., Finnegan, N. L. and Masel, R. I., Particle shape evolution in gas environments: particle shape control in supported metal catalysis. *Catalyst Denctiuation*, 597–603 (1991).

Lee, W. H., Vanloon, K. R., Petrova, V., Woodhouse, J. B., Loxton, C. M. and Masel, R. I., The equilibrium shape and surface energy anisotropy of clean platinum. *Journal of Catalysis*, *126*(2), 658–670 (1990).

Lewis, G. and Fox, P. G., The thickness of thin surface films determined by photo-electron spectroscopy. *Corrosion Science*, *18*(7), 645–650 (1978).

Li, H., Farmer, D. B., Gordon, R. G., Lin, Y. and Vlassak, J., Vapor deposition of ruthenium from an amidinate precursor. *Journal of The Electrochemical Society*, *154*(12), D642 (2007).

Li, Z., Rahtu, A. and Gordon, R. G., Atomic layer deposition of ultrathin copper metal films from a liquid copper(I) amidinate precursor. *Journal of The Electrochemical Society*, *153*(11), C787 (2006).

Liao, W. and Ekerdt, J. G., Ru nucleation and thin film smoothness improvement with ammonia during chemical vapor deposition, *Journal of Vacuum Science & Technology A: Vacuum, Surfaces, and Films*, *34*(3), 031508 (2016).

Liao, W. and Ekerdt, J. G., Effect of CO on Ru nucleation and ultra-smooth thin film growth by chemical vapor deposition at low temperature. *Chemistry of Materials*, *25*, 1793–1799 (2013).

Mate, C. M., Yen, B.K., Miller, D.C., Toney, M.F., Scarpulla, M. and Frommer, J.E., New methodologies for measuring film thickness, coverage and topography. *IEEE Transactions on Magnetics, 36*, 110–114 (2000).

Matsui, Y., Hiratani, M., Nabatame, T., Shimamoto, Y. and Kimura, S., Growth mechanism of Ru films prepared by chemical vapor deposition using bis(ethylcyclopentadienyl)ruthenium precursor. *Electrochemical and Solid-State Letters*, *4*(2), C9–C12 (2001).

Moulder, J. F., Stickle, W. F., Sobol, P. E. and Bomben, K. D., *Handbook of X-ray Photoelectron Spectroscopy*. Physical Electronics. (Perken-Elmer, Eden Prairie, MN, 1992).

Murakami, Y., Li, J., Hirose, D., Kohara, S. and Shimoda, T., Solution processing of highly conductive ruthenium and ruthenium oxide thin films from ruthenium–amine complexes. *Journal of Materials Chemistry C*, *3*, 4490–4499 (2015).

Myli, K. B. and Grassian, V. H., Atomic iodine desorption from single crystal nickel surfaces. *Langmuir*, *11*(15), 849–852 (1995).

Naumkin, A. V., Kraut-Vass, A., Gaarenstroom, S. W. and Powell, C. J., NIST Standard Reference Database 20, Version 4.1. *Measurement Services Division of the National Institute of Standards and Technology* (2012).

Park, S., Kim, H., Kim, K. and Min, S., A novel process to improve the surface roughness of RuO_2 film deposited by metallorganic chemical vapor deposition. *Electrochemical and Solid-State Letters*, *1*(6), 262–264 (1998).

Parkin, S. R., Zeng, H. C., Zhou, M. Y. and Mitchell, K. A. R., Low-energy electron-diffraction crystallographic determination for the Cu(110)2×1-O surface structure. *Physical Review B*, *41*(8), 5432–5435 (1990).

Pasko, S., Hubert-Pfalzgraf, L. G., Abrutis, A. and Vaissermann, J., Synthesis and molecular structures of cobalt(II) β-diketonate complexes as new MOCVD precursors for cobalt oxide films. *Polyhedron*, *23*(5), 735–741 (2004).

Peden, C. H. F., Metal/metal-oxide interfaces: A surface science approach to the study of adhesion. *Journal of Vacuum Science & Technology A: Vacuum, Surfaces, and Films*, *9*(3), 1518 (1991).

Perez-Mariano, J., Lau, K.-H., Sanjurjo, a., Caro, J., Prado, J. M. and Colominas, C., Multilayer coatings by chemical vapor deposition in a fluidized bed reactor at atmospheric pressure (AP/FBR-CVD): TiN/TaN and TiN/W. *Surface and Coatings Technology*, *201*(6), 2174–2180 (2006).

Pfnür, H., Feulner, P., Engelhardt, H. A. and Menzel, D., An example of "fast" desorption: anomalously high pre-exponentials for CO desorption from Ru (001). *Chemical Physics Letters*, *59*(3), 481–486 (1978).

Pfnür, H. and Menzel, D., The influence of adsorbate interactions on kinetics and equilibrium for CO on Ru(001). I. Adsorption kinetics. *The Journal of Chemical Physics*, *79*(5), 2400–2410 (1983).

Pietsch, U., Holy, V. and Baumbach, T., High-Resolution X-Ray Scattering From Thin Films to Lateral Nanostructures. (Springer Tracts in Modern Physics, 2004).

Ratsch, C. and Venables, J. A., Nucleation theory and the early stages of thin film growth. *Journal of Vacuum Science & Technology A: Vacuum, Surfaces, and Films*, *21*(5), S96–S109 (2003).

Rossnagel, S. M. and Kuan, T. S. Alteration of Cu conductivity in the size effect regime. *Journal of Vacuum Science & Technology B: Microelectronics and Nanometer Structures*, *22*, 240 (2004).

Sanyan, S., Kantcheva, M., Suzer, S. and Uner, D. O., FTIR characterization of Ru/SiO_2 catalyst for ammonia synthesis. *Journal of Molecular Structure*, *480-481*, 241–245 (1999).

Sari, W., Eom, T.-K., Jeon, C.-W., Sohn, H. and Kim, S.-H., Improvement of the diffusion barrier performance of Ru by incorporating a WN_x thin film for direct-plateable Cu interconnects. *Electrochemical and Solid-State Letters*, *12*(7), H248 (2009).

Scherrer, P., Bestimmung der Größe und der inneren Struktur von Kolloidteilchen mittels Röntgenstrahlen. *Mathematisch-Physikalische Klasse*, *2*, 98–100 (1918).

Schulz, H., Short history and present trends of Fischer–Tropsch synthesis. *Applied Catalysis A: General*, *186*(1-2), 3–12 (1999).

Senzaki, Y., Gladfelter, W. L. and McCormick, F. B., Chemical vapor deposition of ruthenium and osmium thin films using (hexafluoro-2-butyne) tetracarbonylruthenium and -osmium. *Chemistry of Materials*, *5*, 1715–1721 (1993).

Shallenberger, J. R., Cole, D. A., Novak, S. W., Moore, R. L., Edgell, M. J., Smith, S. P., Hitzman, C. J., Kirchoff, J. F., Principe, E., Biswas, S., Bleiler, R. J., Nieveen, W. and Jones, K., Oxide thickness determination by XPS, AES, SIMS, RBS and TEM. *1998 International Conference on Ion Implantation Technology. Proceedings (Cat. No.98EX144)*, *1*(Cv), 79–82 (1999).

Shetty, S. and van Santen, R. A., CO dissociation on Ru and Co surfaces: The initial step in the Fischer–Tropsch synthesis. *Catalysis Today*, *171*(1), 168–173 (2011).

Shi, A. and Masel, R., The effects of gas adsorption on particle platinum catalysts shapes in supported. *Journal of Catalysis*, *120*, 421–431 (1989).

Shi, A.-C., Fung, K. K., Welch, J. F., Wortis, M. and Masel, R. I., Perspective on the use of gas adsorption for particle-shape control in supported metal catalysis. *Materials Research Sociely*, *111*, 59–64 (1988).

Shimizu, H., Sakoda, K. and Shimogaki, Y., CVD of cobalt–tungsten alloy film as a novel copper diffusion barrier. *Microelectronic Engineering*, *106*, 91–95 (2013).

Shin, J., Kim, H.-W., Hwang, G. S. and Ekerdt, J. G., Chemical routes to ultra thin films for copper barriers and liners. *Surface and Coatings Technology*, *201*, 9256–9259 (2007).

Shin, J., Waheed, A., Winkenwerder, W. a., Kim, H.-W., Agapiou, K., Jones, R. A., Hwang, G. S. and Ekerdt, J. G., Chemical vapor deposition of amorphous ruthenium–phosphorus alloy films. *Thin Solid Films*, *515*, 5298–5307 (2007).

Somorjai, G., Surface Reconstruction and Catalysis. *Annual Review of Physical Chemistry*, *45*(1), 721–751 (1994).

Somorjai, G. A., Molecular level studies of solid-gas and solid-liquid interfaces. *Surface Science*, *335*(C), 10–22 (1995).

Spee, C. I. M. A., Verbeek, F., Kraaijkamp, J. G., Linden, J. L., Rutten, T., Delhaye, H., van der Zouwen, E. A. and Meinema, H. A., Tungsten deposition by organometallic chemical vapour deposition with organotungsten precursors. *Materials Science and Engineering: B*, *17*(1-3), 108–111 (1993).

Strebel, C., Murphy, S., Nielsen, R. M., Nielsen, J. H. and Chorkendorff, I., Probing the active sites for CO dissociation on ruthenium nanoparticles. *Physical Chemistry Chemical Physics : PCCP*, *14*(22), 8005–8012 (2012).

Tanner, R. E., Szekeres, A., Gogova, D. and Gesheva, K., Study of the surface roughness of CVD-tungsten oxide thin films. *Applied Surface Science*, *218*(1-4), 163–169 (2003).

Theolier, A., Choplin, A., D'Ornelas, L., Basset, J. M., Zanderighi, G. and Sourisseau, C. The characterization and thermal stability of a cluster $HRu_3(CO)_{10}(OSi\leqslant)$ grafted on silica surface. *Polyhedron*, *2*(2), 119–121 (1983).

Thom, K. M. and Ekerdt, J. G., The effect of an iodine source on nucleation and film properties of Ru films deposited by chemical vapor deposition. *Thin Solid Films*, *518*, 36–42 (2009).

Thomas, G. E. and Weinberg, W. H., The vibrational spectrum and adsorption site of CO on the Ru(001) surface. *The Journal of Chemical Physics*, *70*(3), 1437–1439 (1979).

Titmuss, S., Wander, A. and King, D. A., Reconstruction of clean and adsorbate-covered metal surfaces. *Chemical Reviews*, *96*(4), 1291–1306 (1996).

Tsai, W. and Weinberg, W. H., Steady-state decomposition of ammonia on the Ru(001) surface. *Journal of Physical Chemistry*, *91*, 5302–5307 (1987).

Ugliengo, P., Saunders, V. R. and Garrone, E., Silanol as a model for the free hydroxyl of amorphous silica: quantum mechanical calculation of the interaction with CO. *Journal of Materials Chemistry*, *93*, 5210–5215 (1989).

Venables, J. A., Spiller, G. D. T. and Hanbucken, M., Nucleation and growth of thin films. *Reports on Progress in Physics*, *47*, 399–459 (1984).

Vigui, J. C. and Spitz, J., Chemical vapor deposition at low temperatures. *Journal of The Electrochemical Society*, *122*(4), 585–588 (1975).

Wang, J., Wang, Y. and Jacobi, K., Dissociation of CO on the Ru(110) surface. *Surface Science*, *488*(1-2), 83–89 (2001).

Wang, Q., Ekerdt, J. G., Gay, D., Sun, Y.-M. and White, J. M., Low-temperature chemical vapor deposition and scaling limit of ultrathin Ru films. *Applied Physics Letters*, *84*(8), 1380–1382 (2004).

Wilf, M. and Folman, M., Field emission study of decomposition of ammonia on individual tungsten planes. *Journal of the Chemical Society*, *72*, 1165–1176 (1975).

Witten, T. A. and Sander, L. M., Diffusion-limited aggregation, a kinetic critical phenomenon. *Physical Review Letters*, *47*(19), 1400–1403, (1981).

Wu, J.-B., Lin, Y.-F., Wang, J., Chang, P.-J., Tasi, C.-P., Lu, C.-C., Chiu, H.-T. and Yang, Y.-W., Correlation between N 1s XPS binding energy and bond distance in metal amido, imido, and nitrido complexes. *Inorganic Chemistry*, *42*, 4516–4518 (2003).

Zaera, F., Preparation and reactivity of alkyl groups adsorbed on metal surfaces. *Accounts of Chemical Research*, *25*(6), 260–265 (1992).

Zanderighi, G. M., Dossi, C., Ugo, R., Psaro, R., Theolier, A., Choplin, A., D'Ornelas, L. and Basset, J. M., Surface supported metal cluster carbonyls. Chemisorption, reactivity, and decomposition of $Ru_3(CO)_{12}$ on silica. *Journal of Organometallic Chemistry*, *296*(1-2), 127–146 (1985).

Zhao, Q., Greve, D. W. and Barmak, K., UHV/CVD growth of Co on Si(001) using cobalt carbonyl. *Applied Surface Science*, *219*(1-2), 136–142 (2003).

Zhdanov, V. P. and Zamaraev, K. I., Lattice-gas model of chemisorption on metal surfaces. *Soviet Physics Uspekhi*, *29*(8), 755–776 (1986).

Zhuravlev, L. T., The surface chemistry of amorphous silica. Zhuravlev model. *Colloids and Surfaces A: Physicochemical and Engineering Aspects*, *173*(1-3), 1–38 (2000).

Zubkov, T., Morgan, G. A., Yates, J. T., Kühlert, O., Lisowski, M., Schillinger, R., Fick, D. and Jänsch, H. J., The effect of atomic steps on adsorption and desorption of CO on Ru(109). *Surface Science*, *526*(1-2), 57–71 (2003).